

Sub-picosecond dynamics during relativistic laser-plasma interaction

Mohammed Almassarani



FRIEDRICH-SCHILLER-
UNIVERSITÄT
JENA

DISSERTATION

zur Erlangung des akademischen Grades
doctor rerum naturalium (Dr. rer. nat.)

vorgelegt dem Rat der Physikalisch-Astronomischen Fakultät
der Friedrich-Schiller-Universität Jena
von M.Sc. Mohammed Almassarani
geboren am 23.01.1988 in Kuwait

Gutachter:

1. Prof Dr. Gerhard G. Paulus
Institut für Optik und Quantenelectronik
Friedrich-Schiller-Universität Jena
2. Prof Dr. Jörg Schreiber
Experimentalphysik, Fakultät für Physik
Ludwig-Maximilians-Universität München
3. Dr. Matthias Schnürer
Max-Born-Institut für Nichtlineare Optik und Kurzzeitspektroskopie
Technische Universität Berlin

Tag der Disputation: 23.05.2024

Abstract

In this dissertation, we explore two major themes related to intense laser-matter interaction. Firstly, we present a comprehensive characterization of the intense THz emission from the rear surface of thin targets during the interaction with ultrashort laser pulses. We report the detection of THz pulses with a record-breaking field strength of 3 MV/cm . We utilize a novel detection scheme based on a non-collinear single-shot electro-optic detection technique. The characterization encompasses the picosecond-temporal waveform, the spectral analysis, the polarization state, and the 3D angular distribution of the THz emission. To verify the correlation between the spatiotemporal dynamics of the charged particles and the THz radiation, we conduct quantitative measurements of the charged particle emission at the rear surface of the target, including a parametric investigation of the energy, particle yield, temperature, and angular distribution of accelerated protons and electrons. Moreover, we perform detailed numerical modeling of various generation mechanisms of THz emission based on the charged particle measurements and find an excellent agreement with the experimentally measured THz emission. Furthermore, our findings reveal a notable agreement between the estimated temporal properties of the electron emission derived from the THz analysis and hot electron spectra. This strongly validates the reliability and utility of THz-based diagnostics for characterizing the temporal dynamics of electron emission during laser-matter interaction.

Secondly, we report the first direct visualization of the Coulomb field of relativistic electron bunches from laser-thin solid interactions on a sub-picosecond timescale. We introduce a novel non-destructive single-shot detection scheme based on the electro-optic principle. Our time-resolved measurements reveal a complex temporal structure with multiple electron bunches propagating at nearly the speed of light. Moreover, our observations confirm the contraction of the electric field of the relativistic electron bunches under the Lorentz transformation. Further, we demonstrate the spatiotemporal evolution of the Coulomb field wavefronts as the electron bunches propagate away from the target. This work paves the way for non-invasive measurements of fast dynamics of charged particles on sub-picosecond timescales.

Zusammenfassung

In dieser Dissertation wird zwei Hauptthemen im Zusammenhang mit intensiver Laser-Materie-Wechselwirkung untersucht. Erstens wird eine umfassende Charakterisierung der intensiven THz-Emission von der Rückseite einer dünnen Folie während der Wechselwirkung mit einem ultrakurzen Laserimpuls präsentiert. Wir werden über die Erfassung von THz-Impulsen mit einem Rekord-Feldstärke von 3 MV/cm berichten. Wir werden ein neuartiges Erfassungsschema verwenden, das auf einer nicht-kollinearen Einzelschuss-Elektrooptik-Detektionstechnik basiert. Die Charakterisierung umfasst die Pikosekunden-Wellenform, die spektrale Analyse, den Polarisationszustand und die 3D-Winkelverteilung der THz-Emission. Um die Korrelation zwischen den räumlich-zeitlichen Dynamiken der geladenen Teilchen und der THz-Strahlung zu verifizieren, führen wir quantitative Messungen der geladenen Partikelemission an der Rückseite der Probe durch, einschließlich einer parametrischen Untersuchung von Energie, Teilchenausbeute, Temperatur und Winkelverteilung von beschleunigten Protonen und Elektronen. Darüber hinaus werden wir detaillierte numerische Modellierung verschiedener Generationsmechanismen der THz-Emission durchführen. Diese basiert auf den geladenen Partikelmessungen und zeigt eine ausgezeichnete Übereinstimmung mit der experimentell gemessenen THz-Emission. Zudem zeigen unsere Ergebnisse eine bemerkenswerte Übereinstimmung zwischen den geschätzten zeitlichen Eigenschaften der Elektronenemission, die aus der THz-Analyse abgeleitet werden, und den Spektren heißer Elektronen. Dies bestätigt nachdrücklich die Zuverlässigkeit und Nützlichkeit der THz-basierten Diagnostik zur Charakterisierung der zeitlichen Dynamik der Elektronenemission während der Laser-Materie-Wechselwirkung.

Zweitens wird über die erste direkte Visualisierung des Coulomb-Feldes relativistischer Elektronenbündel aus der Wechselwirkung dünner Folien mit Lasern auf einer sub-pikosekunden Zeitskala berichtet. Wir werden ein neuartiges zerstörungsfreies Einzelschuss-Schema vorstellen, das auf dem elektrooptischen Prinzip basiert. Unsere zeitaufgelösten Messungen enthüllen eine komplexe zeitliche Struktur mit mehreren Elektronenbündeln, die sich nahezu mit Lichtgeschwindigkeit ausbreiten. Darüber hinaus bestätigen unsere Beobachtungen die Kontraktion des elektrischen Feldes der relativistischen Elektronenbündel unter der Lorentz-Transformation. Zudem demonstrieren wir die räumlich-zeitliche Evolution der Coulomb-Feld-Wellenfronten, während die Elektronenbündel sich von der Folie entfernen. Diese Arbeit ebnet den Weg für nicht-invasive Messungen schneller Dynamiken geladener Teilchen auf relativistischen Zeitskalen.

Acknowledgment

Sir Isaac Newton once said, **“If I have seen further, it is by standing on the shoulders of giants.”** He used this peculiar analogy to explain that his ideas did not come from him alone. With this sentiment in mind, I am compelled to extend through this acknowledgment my profound gratitude to all those who have been instrumental in my journey over the past few years.

First and foremost, I wish to extend my heartfelt appreciation to our group leader, Professor Dr. Gerhard G. Paulus. It is with immense gratitude that I acknowledge the opportunity to join his group and engage in a project that intertwines two of my genuine passions: lasers and plasma. Under his guidance, I had the privilege to work in the high-power laser facility, the Jeti-40, where I conducted my experimental campaigns, made possible by his unwavering support.

I extend my sincere gratitude to Dr. Matthias Kübel, an outstanding scientist and exceptional colleague. He was always available with open doors for my spontaneous inquiries and questions. I really enjoyed the long and informative scientific discussions we had. His extraordinary passion and commitment to the realm of science make him the ideal scientist we need in academia. His willingness to share not only his knowledge but also the lab equipment was crucial in moving my project forward.

I am deeply grateful to my former supervisor, Dr. A. Gopal, for her unlimited support and helpful criticism. She played a key role as a driving force in my first experimental campaign in 2017/2018. Her expertise in THz technology is unparalleled, and I firmly believe she merits the moniker “The THz Lady.” Her contributions have been crucial in shaping my journey.

I would like to thank my former colleague A. Woldegeorgis, with whom I performed my first experiments in the Jet-40 laboratory and shared an office for three years. I owe him a debt of gratitude for his openness and willingness to share his great experiences. It is without exaggeration that I assert, had it not been for the unwavering contributions of both my former colleagues, Dr. Gopal and Woldegeorgis, this project would not have advanced to its current stage.

I am deeply grateful for the help of other colleagues whose contributions have unequivocally shaped the trajectory of this work: Prof. Dr. Kaluza and Prof. Dr. Zepf, whose engaging discussions and unlimited accessibility have been invaluable. Dr. A. Sävert and Dr. G. Becker for technical and scientific support at the Jeti-40 lab. H. Marschner for her support in chemistry. My gratitude extends to B. Beleites and F.

Ronneberger, whose firm support within the Jeti-40 lab has gone above and beyond, even if it means calling them at home in the evening to ask for assistance when the laser system is not working properly.

Last but not least, I would like to thank my family, including my uncle, Dr. F. Almassarani, and my brother, Abdulssalaam, for their faithful belief in me. I am particularly grateful for the unwavering encouragement of my wife, Sanaa, who awaited my return from the lab/office every time. Her boundless love and nurturing care provided the foundation of stability and comfort throughout this journey. And finally, my little hero, my daughter, Lea. Her insatiable curiosity and passion for science served as a constant reminder to strive for excellence both as a loving father and as a dedicated scientist.

Contents

1	Introduction	3
2	Theoretical background	6
2.1	Laser-plasma interaction	6
2.1.1	Absorption mechanisms of intense laser pulses in a plasma	7
2.1.2	Laser-driven ion acceleration	10
2.2	The electro-optic effect	12
2.2.1	Wave propagation in anisotropic crystals	13
2.2.2	The Index of ellipsoid	14
2.2.3	The Pockels effect in ZnTe and GaP	15
2.2.4	Electro-Optic Properties of ZnTe and GaP	21
2.3	Electro-optic signal detection	24
3	Electro-optic detection of THz radiation	30
3.1	Experimental setup	30
3.2	Electro-optic detection of THz radiation	33
3.3	Temporal structure of the THz emission	35
3.4	Polarization state of the THz emission	37
3.5	Angular distribution of terahertz radiation	38
3.6	Conclusion	39
4	Characterization of Charged particle emission	41
4.1	Angular distribution of electron emission	41
4.2	Angular distribution of proton emission	44
4.3	Energy spectra of electrons and protons	45
4.3.1	Electron temperature	46
4.3.2	Laser Intensity Scan	48
4.3.3	Laser Pulse Duration Scan	50
4.3.4	Laser focus Spot Size	53
4.4	conclusion	58

5	Theory of THz generation processes	59
5.1	Coherent transition radiation	59
5.2	Sheath radiation	65
5.3	Bunch length estimation	69
5.4	Comparison of the model and the measured data	71
5.5	Conclusion	73
6	Direct visualization of Coulomb field of relativistic electron bunches from laser-plasma interaction	75
6.1	Experimental setup	75
6.2	Observations of relativistic electron bunches along the target normal direction	78
6.3	Electron bunch length estimation	82
6.4	Electric field dependence on radial distance	83
6.5	Testing signal origin	86
6.6	Observations in the direction of laser propagation	90
6.7	Time evolution via plasmashadowgraphy	92
6.8	Discussion	94
7	Summery	96
8	Appendix	98
9	References	102
10	Ehrenwörtliche Erklärung	115

1 Introduction

Chirped pulse amplification (CPA) [1], honored with the 2018 Nobel Prize in physics, revolutionized the generation of high-power laser pulses with incredibly short durations in the femtosecond (10^{-15} s) range and power levels exceeding petawatts (PW) [2]. By focusing a high-power laser pulse to a spot size of a few micrometers, the intensity can reach 10^{22} W/cm² [3], thereby opening up new frontiers in high-energy-density studies. The interaction of an ultraintense laser pulse with a thin solid-state target produces high fluxes of relativistic electrons that can lead to secondary processes such as bright x-ray and γ -ray emission [4], ion acceleration [5], and powerful terahertz radiation [6]. The plasma produced during such an interaction has many advantages over other well-established generation methods due to the compact size, high damage threshold, and high conversion efficiency. At present intensities, the laser energy is mainly transferred to relativistic electrons, whose collective fields result in the acceleration of ions. In addition, the transient dynamics of charged particles at the rear surface of the target, involving the formation of a plasma sheath and the acceleration of its charges, can generate intense electromagnetic pulses in the terahertz range [7, 8]. In fact, short-pulse laser-based terahertz sources may offer compact and cost-effective alternatives to conventional synchrotrons and free-electron lasers. Even today, they can routinely deliver terahertz pulses with peak powers exceeding the gigawatt level [7]. The generation mechanisms include the excitation of dc polarization in the case of organic crystals [9] and the generation of free electron currents upon ionization of the media [10]. A particularly intriguing aspect of short-pulse laser-based terahertz sources is their ability to generate sub-picosecond single-cycle terahertz pulses with field strengths reaching MV/cm levels [11]. In contrast to visible light, which typically carries an excess of photon energy for collective excitations in condensed matter systems, THz light allows direct coupling to the low-energy (meV scale) excitations of interest, enabling new dynamical states of matter in which the material exhibits properties quite different from those of equilibrium [12]. As a result, they have attracted significant interest due to their unique applications, such as coherent manipulation of molecular orientations and electron spin both resonantly and non-resonantly [13, 14], and characterization of laser-wakefield acceleration [15].

Experimental studies and two-dimensional particle-in-cell simulations suggested that the emission of THz radiation is due to charged particle dynamics at the target rear surface via multiple processes such as coherent transition radiation (CTR) by

the electrons exiting the rear of the target [16], surface currents, and sheath radiation [17]. These initial findings sparked considerable interest in investigating terahertz generation from relativistic lasers. [18]. However, the subsequent studies by various groups could not agree on the precise origin and characteristics of the terahertz radiation for comparable experimental conditions [17, 19, 20]. The lack of agreement among these studies has prompted the need for further research into the underlying mechanisms driving the emission of intense THz radiation from the target rear surface.

In this work, we resolve this ambiguity by providing a comprehensive and thorough characterization of the THz radiation emission from the rear surface of a thin solid target irradiated by intense laser pulses. We present an accurate temporal characterization of the THz emission using single-shot, spatially-resolved electro-optic (EO) detection. Moreover, we illustrate the directional properties of the THz emission by providing their complete three-dimensional (3D) angular distribution. In order to gain a deeper insight into the generation mechanisms responsible for the THz emission, we perform thorough quantitative measurements of the charged particle emission at the rear surface of the target during the interaction. This includes parametric investigations of the energy, temperature, and angular distribution of the particles. We employ the experimentally recorded electron and ion spectra to conduct a detailed numerical analysis of the THz generation and compare the results of the numerical modeling with the experimental observations.

Different groups have used various laser and target parameters to transfer laser energy into the electron beam [21], however, while most studies measure the integrated energy of the accelerated electrons, detailed studies of the temporal structure of the electron emission are lacking. Many studies either lack single-shot capability or compromise electron beam quality by inserting a detection medium in the beam path. Indeed, obtaining accurate time-resolved data remains challenging, mainly due to the limitations of diagnostics in the sub-picosecond timescales involved. Nevertheless, acquiring temporal information is essential as it provides an invaluable understanding of the energy coupling pathways, enabling the optimization of the interaction. Moreover, due to the velocity and phase matching conditions, an accurate temporal mapping of the electron emission is crucial for efficient post-acceleration using synchronized energy sources such as optical [22] and THz [23] based acceleration schemes.

In this work, we also report on novel experimental results on the temporal structure of the relativistic electrons emitted during intense laser-thin target interaction. We employ a single-shot non-destructive electro-optic detection system to visualize

the Coulomb field of relativistic electron bunches on a sub-picosecond time scale. The transient electric field of the relativistic electron bunches induces a momentary birefringence in an electro-optic crystal (EOC) due to the Pockels effect. The EOC is probed with an ultrashort optical pulse, allowing for a single-shot temporal-to-spatial conversion that can be used to reconstruct the temporal structure of the transients on a sub-picosecond timescale. We experimentally demonstrate, the spatial contraction of the Coulomb field of electron bunches propagating at near relativistic speed as predicted by special relativity under the Lorentz transformation. Furthermore, we directly observe the spatiotemporal evolution of the detected wavefronts of the Coulomb fields as the relativistic electron bunches propagate away from the target. The time-resolved mapping of the contracted Coulomb fields reveals a complex temporal structure of the relativistic electron emission, shedding light on the involved acceleration mechanisms, which vary based on interaction parameters. These results significantly contribute to our understanding of laser-thin target interactions and provide valuable insights for characterizing electron acceleration processes.

This thesis is organized as follows. In **Chapter 2**, we briefly explain the theoretical concepts relevant to the laser-thin target interaction. We also include the electro-optic effect (Pockels effect) and a detailed description of the detection schemes used for THz radiation and relativistic electron bunches. **Chapter 3** presents a comprehensive characterization of the THz radiation from the rear target side during the interaction. This includes a precise temporal waveform, polarization, and 3D angular distribution of the THz emission. In **Chapter 4**, we conduct a parametric study of the charged particle emission from the rear side of the target, analyzing electron and ion energy spectra, temperature, and angular distribution. **Chapter 5** focuses on a detailed numerical investigation of the physical processes leading to the emission of THz radiation, using the experimentally measured electron and ion spectra from the previous chapter. We compare the numerical modeling results with the measured THz emission and estimate the corresponding electron bunch longitudinal length. Finally, in **Chapter 6**, we report on a novel pilot experiment to visualize the temporal structure and spatiotemporal evolution of the wavefronts of the Coulomb field accompanying the emission of relativistic electron bunches during the interaction.

2 Theoretical background

This chapter provides a concise theoretical overview with essential concepts applicable to this work in three main sections: 2.1 presents the fundamental aspects of the laser-plasma interaction and the optical energy transfer leading to the acceleration of electrons and ions. Next, we convey the mathematical treatment of the Pockels effect in electro-optic crystals in Section 2.2, and finally, in Section 2.3, we demonstrate the experimental procedure for detecting transient phenomena during laser-plasma interactions using electro-optic detection.

2.1 Laser-plasma interaction

When an ultra-high peak power laser pulse interacts with a thin target, a pre-plasma can be formed due to heating by the advancing part of the amplified spontaneous emission (ASE) of the laser pulse. If it is suppressed, however, by the use of a plasma mirror, for example, or in a high-contrast laser pulse, a plasma is created due to optical field ionization by the main pulse [24, 25]. The plasma consists of charged particles, i.e. electrons and ions. The particles with the largest charge-to-mass ratio, namely the electrons, are accelerated by the laser first. The motion of electrons in this regime is governed by the dimensionless laser amplitude:

$$a_0 = \frac{eE_0}{m_e c \omega} = \sqrt{\frac{I_0}{1.37 \times 10^{18} \text{ W/cm}^2 (\mu\text{m}/\lambda)^2}} \quad (1)$$

where e and m_e are the electron charge and mass, and I_0 , E_0 , λ , and ω are laser peak intensity, electric field, wavelength and angular frequency, respectively. For a laser wavelength of $\sim 1 \mu\text{m}$ and $I \gg 10^{18} \text{ W/cm}^2$, the dimensionless amplitude is much larger than unity. In this case, a significant number of electrons in the plasma are accelerated to relativistic velocities within a few cycles of the laser electric field, leading to a 'relativistic plasma' [26, 27] with collisionless heating effects [28]. Further, the electron motion is governed by both magnetic and electric fields. For direct ion acceleration, however, the analogous dimensionless amplitude $a_i = eE_0/m_i c \omega$, where m_i is the ion mass, remains much smaller than unity for all experiments performed to date in laboratories around the world. The irradiance value corresponding to $a_i = 1$ for protons is $I \sim 10^{24} \text{ W/cm}^2 (\mu\text{m}/\lambda)^2$.

It is useful to define the following parameters; The plasma density scale length L

is defined as [29]

$$L \equiv n_e \left(\frac{dn}{dx} \right)^{-1} \approx c_s \tau_L; \quad c_s \approx \sqrt{Z^* k_B T_e / M_i} \quad (2)$$

where n_e is the plasma density, dn/dx is the slope of the density at n_e , τ_L is the laser pulse duration, c_s is the speed of the acoustic wave (sound) in the plasma with T_e is the electron temperature, M_i is the ion mass, and k_B is Boltzmann's constant. In addition, the plasma frequency which stems from the collective electron density oscillations caused by charge imbalance against the positive ion background, is given as $\omega_p = \sqrt{4\pi e^2 n_e / m}$ where m denotes the electron rest mass. A plasma becomes overdense if its electron density n_e exceeds the critical density $n_{cr} = \sqrt{\omega_L^2 m / 4\pi e^2}$. This description arises from the expression for the refractive index of transverse electromagnetic waves in plasmas $n_{ref} = \sqrt{1 - \omega_p^2 / \omega_L^2}$. Thus, for $\omega_L < \omega_p$, the refractive index becomes purely imaginary. As a result, the plasma becomes non-transparent to the EM wave, effectively blocking the laser field from reaching the target volume. This has a significant impact on how the laser energy is absorbed by the material.

2.1.1 Absorption mechanisms of intense laser pulses in a plasma

We briefly describe the main mechanisms responsible for the transport of laser energy to plasma electrons under the conditions present in this work. When the intensity reaches $10^{11} - 10^{12} \text{ W/cm}^2$ at the advancing pulse pedestal prior to the main laser pulse, the absorption is dominated by collisional absorption (inverse bremsstrahlung) and resonance absorption [30,31]. However, for intensities above 10^{15} W/cm^2 , the plasma temperature rises rapidly during the interaction, reducing the importance of collisions for coupling energy [32]. In addition, the electron quiver velocity becomes comparable to the thermal velocity, thus further decreasing the effective collision frequency [33]. Therefore, collisional heating cannot explain the observed high absorption rate at high laser intensities [34,35]. In fact, there are a number of alternative mechanisms that can couple laser energy to plasma in collisionless processes. Depending on the sharpness of the plasma gradient, the polarization of the laser light, and the angle of incidence, vacuum heating or $j \times B$ absorption may occur.

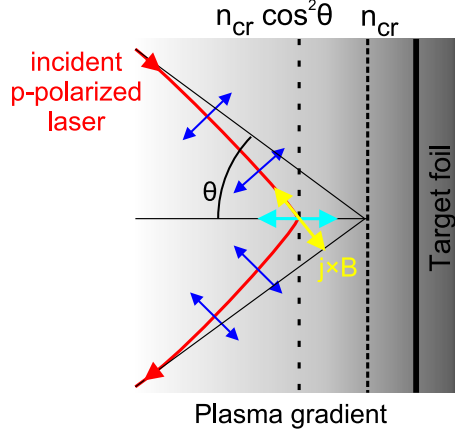


Figure 1: A p-polarized laser pulse is incident obliquely onto a plasma gradient at the front surface of the target. The laser light propagates up to a density of $n_{cr} \cos^2 \theta$ before it is specularly reflected, creating a standing wave at the turning point that leads to an evanescent decaying electric field in the longitudinal direction. The cyan arrow represents a resonantly excited plasma wave that accelerates electrons inside the target along the normal direction. Additionally, the yellow arrow indicates the direction of the ponderomotive acceleration along the laser propagation.

Resonance absorption

In the standard picture [36], we consider a plasma expanding from a solid surface into the vacuum in the z direction with a p-polarized laser pulse being incident at an angle θ with respect to the surface's normal. We also consider a plasma gradient ∇n in the case where $\vec{E} \cdot \nabla n \neq 0$. Using Snell's law, it is easy to show that the laser light propagates up to the density $n_{cr} \cos^2 \theta$ before it is specularly reflected. At the same time, some of the light energy will tunnel into the critical density. If the electric field vector, \vec{E} , of the laser light is in the direction of the density gradient ∇n , an electron plasma wave will be resonantly excited at a depth where the frequency $\omega_p = \omega_L$. The transferred energy goes into accelerating a fraction of the electrons in the plasma. The damping of the oscillation amplitude can be assumed to be due to either collisional or collisionless effects such as particle trapping or wave breaking. In addition, it was found that the energy distribution of the accelerated electrons is roughly a Maxwellian "tail" of hot electrons superimposed on the initial background temperature. The temperature of the hot electrons due to resonance absorption scales as [37, 38]

$$T_{\text{res}} \approx (I[10^{18} \text{ W/cm}^2] \lambda^2[\mu\text{m}^2])^{1/3} \text{ [MeV]} \quad (3)$$

As hinted at earlier, resonance absorption is less effective at very steep density

gradients. In a sharp density profile, the resonance breaks down if the field amplitude of the oscillations exceeds the density scale length L , i.e. if $v_{os}/\omega_0 L > 1$ [39]. It is worth mentioning that at higher intensities, effects such as the rippling of the critical surface due to a Rayleigh–Taylor-like instability may increase the absorption, providing additional regions where $\vec{E}\nabla n \neq 0$. In fact, this may enable resonance absorption for s-polarized light [40].

Brunel (vacuum heating)

Classical resonant absorption becomes less effective for sharp plasma gradients ($L/\lambda \ll 1$) since no resonant plasma waves can be established. This simple fact was pointed out by Brunel [41], who proposed an alternative mechanism in which electrons are directly heated by the p-polarized component of the laser field. The electrons are pulled away from the plasma-vacuum interface, spun around, and accelerated back into the plasma with $v \approx v_{os}$ within half a laser cycle, with $v_{os} = eE/m_e\omega$, ω being the quiver velocity. The accelerated electrons are absorbed and the energy will be eventually spread through collisions in the plasma. The thermal electron temperature implied by this model and by electrostatic PIC simulations is [39]

$$T_{\text{vac}} \propto v_{\text{os}}^2 \approx 3.6I[10^{16} \text{ W/cm}^2]\lambda^2[\mu\text{m}^2] \quad (4)$$

While this model predicts both high absorption and a strong hot temperature scaling, subsequent studies with electromagnetic codes showed that the mechanism saturates at high intensities due to the deflection of the electron orbits by the $v \times B$ force [42,43].

Relativistic $\mathbf{j} \times \mathbf{B}$ heating

For relativistic irradiance and relatively gentle plasma gradients, $\mathbf{j} \times \mathbf{B}$ heating becomes effective [44]. The driving force in this case arises from the oscillating component of the ponderomotive force of the laser. It relies on the large gradient of the laser light near the vacuum plasma interface, due to the penetration of the laser's electric and magnetic fields. For an electron fluid element in the plasma, near the vacuum plasma interface, the equation of motion is

$$\frac{\partial \vec{p}}{\partial t} + \vec{v} \cdot \vec{\nabla} \vec{p} = -e \left[\vec{E} + \frac{\vec{v} \times \vec{B}}{c} \right] \quad (5)$$

where $\vec{p} = \gamma m_0 \vec{v}$, and γ is the Lorentz factor. By rewriting the electromagnetic fields

in terms of a vector potential \vec{A} , one obtains the following equation for the longitudinal component of the electron fluid momentum [31]

$$\frac{\partial \vec{p}_i}{\partial t} = e \vec{\nabla} \phi - m_0 c^2 \vec{\nabla} (\gamma - 1) \quad (6)$$

The first term is the force term due to an electrostatic force. The second term can be identified with a relativistic ponderomotive force, from which the potential can be written as

$$U_p = (\gamma - 1) m_0 c^2 \quad (7)$$

As a result, the electrons are accelerated along the laser propagation direction at twice the laser frequency. The effective electron temperature scales as [45]

$$T_{\text{pond}} = m_0 c^2 \left(\sqrt{1 + \frac{I[\text{W}/\text{cm}^2] \lambda^2[\mu\text{m}^2]}{2.8 \times 10^{18}}} - 1 \right) \quad (8)$$

It is worth mentioning that the effectiveness of this absorption mechanism is reduced when a high-density plasma with sharp gradients is present [31].

Other heating mechanisms, such as the anomalous skin effect, can contribute to the energy coupling process during the interaction and can be found in the reviews [31, 39].

2.1.2 Laser-driven ion acceleration

As previously hinted, a direct acceleration of the ions, especially at the back surface of the target, cannot be obtained directly by the laser light; thus, the acceleration of the ions has to rely on the energetic electrons that can propagate through the target. Indeed, several models have been proposed to describe the emission of positively charged particles from the rear surface of an irradiated target, such as target normal sheath acceleration (TNSA) [46] and radiation pressure acceleration (RPA) [47], or even both in a hybrid acceleration scheme [48]. A detailed review of all possible ion acceleration processes during laser-matter interactions can be found in the review articles [49, 50]. For laser intensities of $\sim 10^{19} \text{ W}/\text{cm}^2$ and thin targets, the TNSA mechanism is the dominant process; Henceforth, we will focus on the TNSA process in this work.

Target normal sheath acceleration (TNSA)

Experimentally, the recorded ion energy spectrum has a characteristic energy cut-off, which can be well described by the simple physical model proposed in [51–53] based on the expansion of the plasma into vacuum [54, 55]. Fast electrons accelerated by the laser on the irradiated side propagate through and then exit the target. As a result, a huge electrostatic field of the order of TV/m is generated due to the charge separation caused by the escaping electrons and the unbalanced charge left behind. This charge separation field ionizes atoms, and the resulting ions start to expand into the vacuum behind the target, following the electrons [46, 56]. The accelerated ions and protons mainly originate from the hydrogen-rich contamination layer and water vapor. These models assume that initially the ions are at rest and form a sharp boundary with the vacuum. Electrons, in contrast, follow a Boltzmann distribution with an electrostatic potential:

$$n_e = n_{e0} \exp \frac{e\Phi}{T_e} \quad (9)$$

where n_e and T_e denote the hot electron density and temperature. The electrostatic potential satisfies the Poisson equation:

$$\frac{d^2\Phi}{dz^2} = 4\pi e(n_e - Z_i n_i) \quad (10)$$

where n_i and eZ_i are the ion density and charge along the spatial coordinate z . In the TNSA model, the plasma is neutral except for a small region near the expansion front, the so-called plasma sheath, which has a width of the order of the Debye length $\lambda_D = \sqrt{T_e/4\pi n_e e^2}$. The integration of Equation 10 gives a measure of the initial electric field at the target rear surface,

$$E_{\text{sheath}} = \sqrt{\frac{2}{e_N} \frac{T_e}{e \lambda_D}} = \left(\frac{8\pi}{e_N} n_e T_e \right)^{1/2} \quad (11)$$

with e_N being Euler's number. Using the 1D isothermal plasma expansion model [51] one can derive the maximum ion energy,

$$\mathcal{E}_{\text{max}}(t) = 2ZT_e \left\{ \ln \left[\frac{\omega_{pi} t}{\sqrt{2e_N}} + \sqrt{\left(\frac{\omega_{pi} t}{\sqrt{2e_N}} \right)^2 + 1} \right] \right\}^2 \quad (12)$$

Here $\omega_{pi} = \sqrt{4\pi Z_i n_{e0} e^2 / m_i}$ is the ion plasma frequency with n_{e0} being the initial

plasma density. The limitation of such a 1D model is that the ion energy grows to infinity at $t \rightarrow \infty$. In actuality, the ion energy is always finite. It is reasonable to assume that the 1D approximation breaks down when the ion front extends to distances of the order of the sheath's transverse size. A more refined expression for the maximum energy of the accelerated ions is given as [57],

$$\mathcal{E}_{\max} = \frac{ZT_e}{\lambda_D} \frac{\sqrt{A_{\text{sheath}}}}{\pi} = 2Zm_e c^2 \sqrt{\frac{\eta P_L}{8.7 \times 10^9 \text{ W}}} \quad (13)$$

whereas $A_{\text{sheath}} = \pi(r + d \tan \theta)^2$ denotes the transverse area of the sheath with r , d , and θ being the focal spot radius, the target thickness, and the half-opening angle of the electrons spread during their propagation through the target. $P_L = E_L/\tau_L$ is the laser power and η is the conversion efficiency of laser energy absorption into hot electron generation. For our experimental parameters, this model gives a maximum proton energy around $\mathcal{E}_{\max} \approx 4 \text{ MeV}$.

It is worth mentioning that laser-driven ion acceleration is a very complex process that is influenced by many physical phenomena [50]. Examples include plasma formation, absorption of laser energy into electrons, plasma evolution driven by laser and collective plasma fields, electron transport, and charge particle dynamics during acceleration.

2.2 The electro-optic effect

Electro-optical detection schemes are widely employed in a myriad of demanding fields such as electron bunching measurements at linear accelerator facilities [58]. The experiments described in this work use the electro-optic effects to reconstruct the temporal profile of the THz radiation and electron bunches emission during laser-plasma interactions. In short, birefringence can be induced in an electro-optic crystal by the field of interest, such as a quasi-static Coulomb field of a relativistic electron bunch or an electromagnetic pulse in the THz regime, and the birefringence is subsequently probed by ultrashort laser pulses. In the following, we review the physical background of the electro-optic effect (Pockels effect).

2.2.1 Wave propagation in anisotropic crystals

It is customary to describe the propagation of an electromagnetic wave (EM) using the well-known Maxwell's equations, which lead to the wave equation in dielectric materials

$$\nabla^2 \mathbf{E} - \frac{1}{c^2} \frac{\partial^2 \mathbf{E}}{\partial t^2} = \mu_0 \frac{\partial^2 \mathbf{P}}{\partial t^2} \quad (14)$$

where \mathbf{E} is the electric field vector, \mathbf{P} is the electric polarization in the material, and μ_0 is the permeability of free space. As the EM wave penetrates the optical material of interest, the electrons respond by generating a new field with electric polarization \mathbf{P} , which counteracts or increases the external flux:

$$\mathbf{P} = \mathbf{D} - \varepsilon_0 \mathbf{E} = \chi_e \varepsilon_0 \mathbf{E} \quad (15)$$

where \mathbf{D} [$\frac{\text{As}}{\text{m}^2}$] is The electric displacement density or flux density, ε_0 is the vacuum permittivity, and χ_e is the electric susceptibility.

In an isotropic medium, the induced polarization is always parallel to the electric field vector and is related to the field by the susceptibility. In the case of an anisotropic medium, however, the induced polarization is not necessarily parallel to the electric field, facilitating the treatment of the susceptibility as a tensor χ_{ij} . The coefficients of the susceptibility tensor depend on the choice of the coordinate system with respect to the crystallographic axis of the lattice. Since the susceptibility tensor χ_{ij} is symmetric for non-absorbing crystals, it can be diagonalized with the non-vanishing eigenvalues, also called main-susceptibilities [$\chi_{ii} \equiv \chi_{11}, \chi_{22}, \chi_{33}$]. The axes, chosen such that the susceptibility tensor is a diagonal matrix, are called the principal axes of the crystal. If the components of χ_{ii} are not all equal, the material will exhibit birefringence. Similarly, the dielectric permittivity tensor will be

$$\varepsilon_{ij} = 1 + \chi_{ij} \quad (16)$$

In this case, the permittivity is a symmetric tensor, and \mathbf{D} in equation 15 is in general not parallel to the electric field.

In an anisotropic crystal, the phase velocity of a plane electromagnetic wave is given by

$$v_p = \frac{c}{\sqrt{\varepsilon}} = \frac{c}{n} \quad (17)$$

which depends on both the direction of propagation and the polarization. We can consider two orthogonal axes U_s and U_f with different phase velocities and, accordingly, different refractive indices. The accounted refractive indices are commonly referred to as n_s (slow) and n_f (fast). In general, during the propagation of a linearly polarized electromagnetic wave through a crystal, the field vector can be decomposed into two components parallel to the two optical axes of the crystal, each with a different phase velocity. As a result, a phase shift between the two components is induced and the polarization of the exiting wave is altered with respect to its initial state.

2.2.2 The Index of ellipsoid

To find the indices of refraction n_s and n_f , it is customary to define the so-called index ellipsoid. Considering that the energy density in the electrical form is half of the total, we can write the energy density of an electric field as

$$w_e = \frac{1}{2} \mathbf{E} \cdot \mathbf{D} = \frac{1}{2} \sum_{i,j} E_i \varepsilon_{ij} E_j \quad (18)$$

If we rotate our coordinate system so that these axes are parallel to the axes of the ellipsoid, we then rearrange into

$$w_e = \frac{1}{2} (\varepsilon_1 E_1^2 + \varepsilon_2 E_2^2 + \varepsilon_3 E_3^2) \quad (19)$$

substituting $E_i = \frac{D_i}{\varepsilon_i}$ gives

$$2w_e = \frac{D_1^2}{\varepsilon_1} + \frac{D_2^2}{\varepsilon_2} + \frac{D_3^2}{\varepsilon_3} \quad (20)$$

By taking a suitable dimensionless vector along the direction of D such as

$$u = \begin{pmatrix} u_1 \\ u_2 \\ u_3 \end{pmatrix} = \frac{D}{\sqrt{2w_e}} \quad (21)$$

and by considering the main refractive indices for a nonmagnetic material $n_i = \sqrt{\varepsilon_i}$; $i = 1, 2, 3$ we get the equation of the refractive index ellipsoid

$$\frac{u_1^2}{n_1^2} + \frac{u_2^2}{n_2^2} + \frac{u_3^2}{n_3^2} = 1 \quad (22)$$

The main axes of the index ellipsoid have the length $2n_i$ and are parallel to the optical axes of the crystal. The electric impermeability tensor is defined by

$$\boldsymbol{\eta} = \boldsymbol{\varepsilon}^{-1} \quad (23)$$

which form in the principal axis system of the crystal as

$$\boldsymbol{\eta} = \begin{pmatrix} \frac{1}{n_1^2} & 0 & 0 \\ 0 & \frac{1}{n_2^2} & 0 \\ 0 & 0 & \frac{1}{n_3^2} \end{pmatrix} \quad (24)$$

The equation of the index ellipsoid can be rewritten as

$$\mathbf{u} \cdot \boldsymbol{\eta} \cdot \mathbf{u} = 1 \quad (25)$$

For light waves propagating in a giving direction, the index ellipse is obtained by defining an intersecting plane through the origin of the ellipsoid perpendicular to the propagation direction, see Figure 2. The index ellipse gives the refractive indices n_s and n_f which indicates the vibration direction of the light waves, as the electric vectors of the waves vibrate along the major and minor axes of the index ellipse. For each direction of travel in an anisotropic medium, there are two plane-polarized light waves that vibrate perpendicular to each other and travel at different velocities, giving rise to the phenomenon of birefringence. Reference [59] offers an interactive model of the index ellipsoid.

2.2.3 The Pockels effect in ZnTe and GaP

An external static (or quasi-static) electric field can alter the properties of an optically active crystal as the refractive index becomes a function of the field. The change in refractive index in some materials depends linearly on the strength of the applied electric field, leading to changes in the orientation and shape of the index ellipse. For sufficiently high electric fields, the polarization shown previously becomes nonlinear and can be written as a power series in field strength:

$$\mathbf{P} = \varepsilon_0(\boldsymbol{\chi}_e^{(0)} \mathbf{E} + \boldsymbol{\chi}_e^{(1)} \mathbf{E}^2 + \boldsymbol{\chi}_e^{(2)} \mathbf{E}^3 \dots) \quad (26)$$

For weak electric fields, all but the first term can be neglected. The linear susceptibility $\boldsymbol{\chi}^{(0)}$ (first-order susceptibility) induces dispersion where in the case of anisotropic

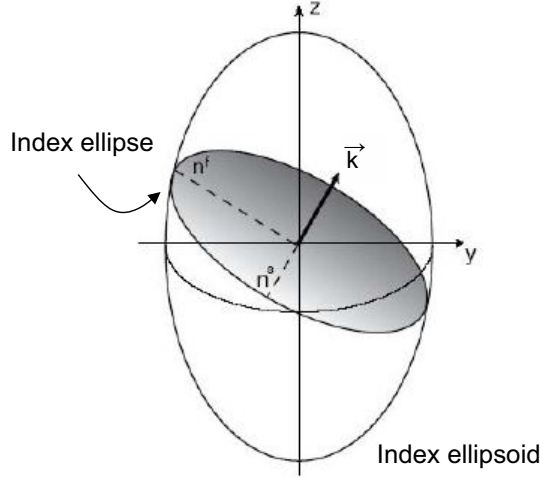


Figure 2: A cross section through the ellipsoid produces a refractive index ellipse for waves traveling normal to that section \vec{k} . The major and minor axes of the ellipse denote the refractive indices encountered by the slow and fast waves, which vibrate with their electric displacement vectors along those two axes. Reference [59] offers an interactive model of the index ellipsoid.

crystals leads to a directional dependence on the speed of light (birefringence). The second-order susceptibility $\chi^{(1)}$ term characterizes how the refractive index depends on the electric field. This is known as the linear electro-optic effect or Pockels effect, on which the work in this thesis relies. Another important implication of $\chi^{(1)}$ is the second harmonic generation. The 3rd order susceptibility $\chi^{(2)}$ leads to a dependency of the refractive index on the intensity of the electric field ($I \sim E^2$) and is called the Kerr or quadratic electro-optical effect. In practice, for intensities below $\sim 10^{16} \text{ W/cm}^2$, polarization terms above third order can be neglected.

In this work we utilize two crystals (ZnTe and GaP) for the detection of THz pulses during the laser-plasma interaction. Such crystals belong to the zinc blende structure group, which features two face-centered cubic lattices shifted by one-quarter of the spatial diagonal, thus leading to a high degree of symmetry. In other words, they can be characterized as isotropic in the absence of an electric field such that $n_1 = n_2 = n_3 = n_0$. However, in the presence of strong electric fields ($E > 10^5 \text{ V/m}$), the force of the electromagnetic field distorts the crystal lattice resulting in an anisotropic crystal. Due to the emerging anisotropy, the susceptibility can be described by a linear dependence on the electric field. We can apply Taylor expansion of χ_e in equation 26 in terms of the electrical field around $\mathbf{E} = 0$ rather than the expansion of the

polarization \mathbf{P} .

Since χ and η are related by equation 16 and 23, the permeability tensor also contains terms of higher order in the presence of a strong external electric field, and can thus be expanded using a Taylor expansion around $E = 0$:

$$\eta_{ij} = \eta_{ij}(0) + r_{ijk}E_k + s_{ijkl}E_kE_l + \dots \quad (27)$$

The case of conventional linear optics can be retained in the first term. In the second term, we have the tensor r_{ijk} that describes the linear electro-optic effect (Pockels coefficients). The next term contains the tensor s_{ijkl} that describes the quadratic electrooptic effect (Kerr coefficients). For the electro-optic crystal used in this work, such as ZnTe and GaP, the term due to the Kerr effect can be neglected as the order of magnitude for both coefficients is:

$$\begin{aligned} r_{ijk} &\approx 10^{-12} \frac{\text{m}}{\text{V}} \\ s_{ijkl} &\approx 10^{-21} \frac{\text{m}^2}{\text{V}^2} \end{aligned} \quad (28)$$

The impermeability tensor thus becomes:

$$\boldsymbol{\eta}(\mathbf{E}) = \varepsilon^{-1} \mathbf{I} + \mathbf{r} \cdot \mathbf{E} \quad (29)$$

Here \mathbf{I} is the identity matrix. Substituting this into the final equation of the index ellipsoid 25 gives

$$\mathbf{u} \cdot \boldsymbol{\eta}(\mathbf{E}) \cdot \mathbf{u} = \sum_{i,j=1,2,3} \left(\varepsilon^{-1} \delta_{ij} + \sum_{k=1,2,3} r_{ijk} E_k \right) u_i u_j = 1 \quad (30)$$

Since the tensor $\boldsymbol{\eta}$ is symmetric ($r_{ijk} = r_{jik}$), it can be simplified by introducing the following nomenclature to contract the indices

(1, 1) → 1	$r_{11k} \rightarrow r_{1k}$
(2, 2) → 2	$r_{22k} \rightarrow r_{2k}$
(3, 3) → 3	$r_{33k} \rightarrow r_{3k}$
(2, 3) → 4	$r_{23k} = r_{32k} \rightarrow r_{4k}$
(1, 3) → 5	$r_{13k} = r_{31k} \rightarrow r_{5k}$
(1, 2) → 6	$r_{12k} = r_{21k} \rightarrow r_{6k}$

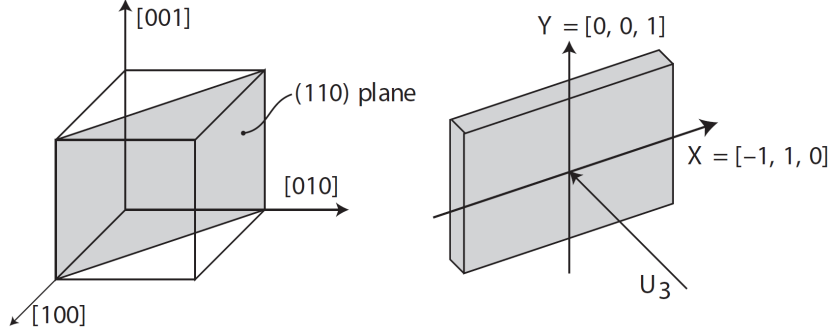


Figure 3: Left: the crystal cut along the (110) plane in the cubic zinc telluride crystal. Right: The coordinate system (X, Y) in the (110) plane. The THz and laser pulses incident along the normal direction U_3 of this plane. This figure is adapted from [60]

The symmetry of a crystal limits the number of independent elements in the matrix of electrooptical coefficients r_{ijk} . Crystals of the zinc blende structure (ZnTe and GaP) feature a high degree of symmetry and as a consequence, the matrix of electro-optical coefficients has only one independent entry ($r_{41} = r_{52} = r_{63}$). We can now calculate the equation for the electro-optically induced index ellipsoid in the following form:

$$\frac{1}{n_0^2}(u_1^2 + u_2^2 + u_3^2) + 2r_{41}(E_1u_2u_3 + E_2u_3u_1 + E_3u_1u_2) = 1 \quad (31)$$

Determination of the main refractive indices

To obtain the principal refractive index, we perform a principal axis transformation where $\eta(\mathbf{E})$ is diagonalized. The crystals used in the following EO experiments are cut in the (110)-plane as schematically presented in Figure 3. It is worth mentioning that the external electric field of interest in this work is assumed to be a linearly polarized electric wave in the terahertz spectral regime \mathbf{E}_{THz} . To maximize the retardation due to the induced birefringence in the presence of a sufficiently strong electric field of THz-radiation, the propagation vectors of both pulses (THz and laser probe) are perpendicular to the cut plane (110); Thus, their electric field vectors vibrate within this plane. A new coordinate system (\mathbf{X}, \mathbf{Y}) is defined in this plane:

$$\mathbf{X} = \frac{1}{\sqrt{2}} \begin{pmatrix} -1 \\ 1 \\ 0 \end{pmatrix}, \quad \mathbf{Y} = \begin{pmatrix} 0 \\ 0 \\ 1 \end{pmatrix} \quad (32)$$

By following the treatment in [60], we assign the angle α between the electric field

component of the perpendicularly incident THz pulse and the X-axis (the $[-1, 1, 0]$ axis of the ZnTe and GaP crystals), giving the components of the electric vector \mathbf{E}_{THz} of the THz radiation in the base system of the crystal lattice as:

$$\mathbf{E}_{\text{THz}} = E_{\text{THz}} \begin{pmatrix} -\frac{1}{\sqrt{2}} \cos \alpha \\ \frac{1}{\sqrt{2}} \cos \alpha \\ \sin \alpha \end{pmatrix} \quad (33)$$

The the field-dependent impermeability becomes:

$$\boldsymbol{\eta}(\mathbf{E}_{\text{THz}}) = \frac{1}{n_0^2} \begin{pmatrix} 1 & 0 & 0 \\ 0 & 1 & 0 \\ 0 & 0 & 1 \end{pmatrix} + r_{41} E_{\text{THz}} \begin{pmatrix} 0 & \sin \alpha & \cos \alpha / \sqrt{2} \\ \sin \alpha & 0 & -\cos \alpha / \sqrt{2} \\ \cos \alpha / \sqrt{2} & -\cos \alpha / \sqrt{2} & 0 \end{pmatrix} \quad (34)$$

In order to find the main refractive indices and the principal axes, we need to write the eigenvalues and eigenvectors of the tensor. The eigenvalues of $\boldsymbol{\eta}(\mathbf{E}_{\text{THz}})$ can be assessed as follows

$$\begin{aligned} \lambda_{1,2} &= \frac{1}{n_0^2} - \frac{r_{41} E_{\text{THz}}}{2} \left(\sin \alpha \pm \sqrt{1 + 3 \cos^2 \alpha} \right) \\ \lambda_3 &= \frac{1}{n_0^2} + r_{41} E_{\text{THz}} \sin \alpha \end{aligned} \quad (35)$$

with the normalized eigenvectors presented in appendix 8.A. Taking into account the relation $n_i = \frac{1}{\sqrt{\lambda_i}}$ along with the approximation $r_{41} E_{\text{THz}} \ll 1/n_0^2$, we get the main indices of refraction of a zinc-blende type crystal in the presence of a strong electrical field:

$$\begin{aligned} n_1 &= n_0 + \frac{n_0^3 r_{41} E_{\text{THz}}}{4} \left(\sin \alpha + \sqrt{1 + 3 \cos^2 \alpha} \right) \\ n_2 &= n_0 + \frac{n_0^3 r_{41} E_{\text{THz}}}{4} \left(\sin \alpha - \sqrt{1 + 3 \cos^2 \alpha} \right) \\ n_3 &= n_0 - \frac{n_0^3 r_{41} E_{\text{THz}}}{2} \sin \alpha \end{aligned} \quad (36)$$

In the crystal plane (110) the axis $\mathbf{U1}$ may enclose an angle of ψ with the X-axis $[-110]$, see Figure 4. The angle ψ can be estimated by computing the scalar product of $\mathbf{U1}$ and \mathbf{X} with the applied relation $\cos(2\psi) = 2 \cos^2 \psi - 1$, giving

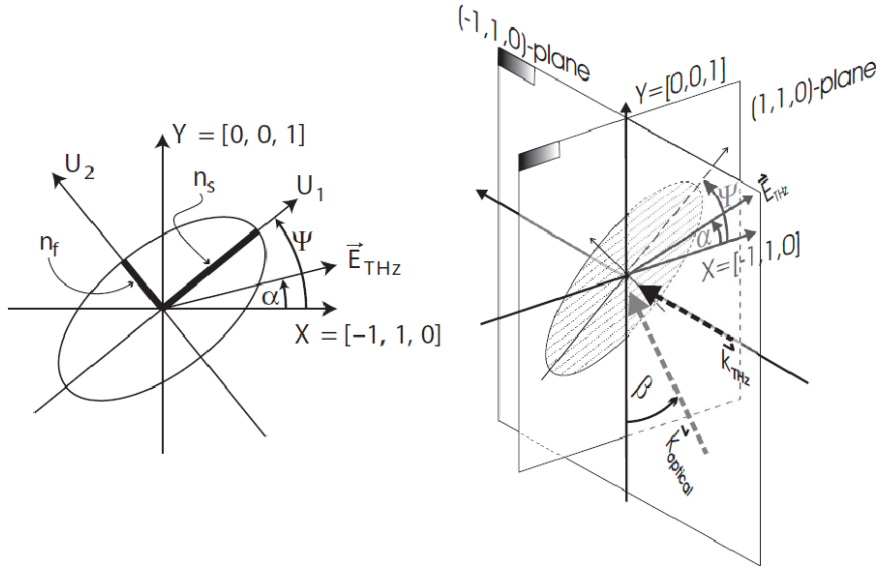


Figure 4: The refractive index ellipsoid projected onto the (110) plane of an electro-optic crystal (ZnTe). The electric vector of the signal of interest \vec{E}_{THz} encloses an angle α with the \mathbf{X} -axis $[-1, 1, 0]$, and the angle between the long half-axis of the ellipse and the \mathbf{X} -axis is given by Equation 37. The larger index implies a slower propagation speed of the light (n_s), where the smaller index corresponds to a faster propagation speed (n_f). Right: both the THz and the laser probe propagate along the normal to the (110) plane. Figure adapted from [60].

$$\cos(2\psi) = \frac{\sin \alpha}{\sqrt{1 + 3 \cos^2 \alpha}} \quad (37)$$

When $\alpha = \pi/2$, the principal axis $\mathbf{U1}$ points in the \mathbf{X} direction, and the axis $\mathbf{U2}$ in the \mathbf{Y} direction. The third principal axis is perpendicular to the (110) crystal plane and parallel to the propagation direction of the THz-radiation. The principal refractive indices corresponding to the first two principal axes are n_1 and n_2 as shown in Figure 4.

When an ultra-short laser probe beam is sent through the crystal along the eigenvector $\mathbf{U3}$ to read the time-dependent birefringence, its wave vector may be tilted by an angle of β with respect to the y-axis (0,0,1) as shown in the right panel in Figure 4. If the angle $\beta \neq 0$, the beam must be p-polarized as to keep the electric vector \vec{E}_{laser} completely within the (110) plane leading to maximum phase shift. This will be the case when detecting THz pulses in Section 3. A modified detection geometry will be utilized in Section 6 where the laser probe beam is incident perpendicularly on the crystal plane. In both cases, however, the laser probe beam is linearly polarized to

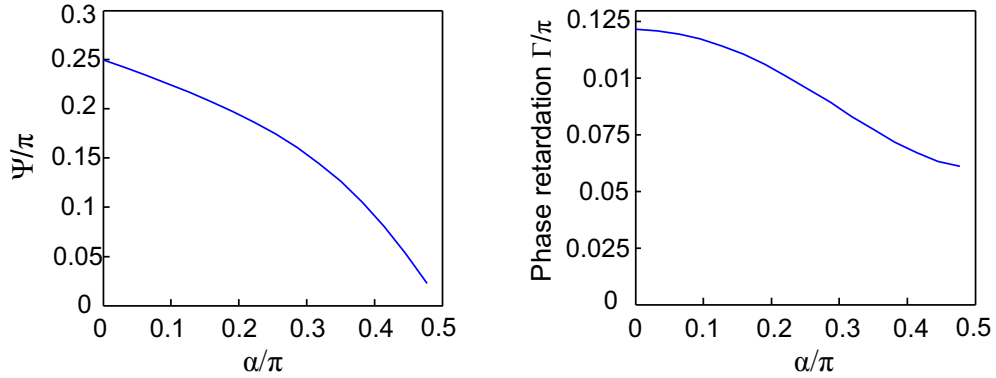


Figure 5: Left: The angle ψ between the long principal axis of the refractive index ellipsoid and the \mathbf{X} -axis in the crystal plane as a function of the angle α between the electric vector \mathbf{E}_{THz} of the THz wave and the \mathbf{X} -axis. Right: The relative phase shift Γ between the two orthogonal components of the laser field $\mathbf{E}_{\text{laser}}$, plotted as a function of the angle α . The retardation Γ is calculated for a $d = 500 \mu\text{m}$ thick ZnTe crystal subjected to a focused THz pulse with a field strength of $E_{\text{Thz}} = 10^6 \text{ V/m}$.

ensure that the laser electric field oscillates in the crystal plane.

In a crystal of thickness d in the presence of a sufficiently strong external THz field, the two components of $\mathbf{E}_{\text{laser}}$ along the principal axes $\mathbf{U1}$ and $\mathbf{U2}$ acquire a relative phase shift of

$$\Gamma = \frac{\omega_0 d}{c} (n_1 - n_2) = \frac{\pi d}{\lambda_0} n_0^3 r_{41} E_{\text{THz}} \sqrt{1 + 3 \cos^2 \alpha} \quad (38)$$

where ω_0 is the angular frequency of the laser light and λ_0 its wavelength in vacuum. The rotation angle ψ of the index ellipse in the (X, Y) plane and the relative phase shift Γ . The phase shift is referred to as retardation parameter, which is proportional to the strength of the external electric field \mathbf{E}_{THz} and depends on the angle α between the field vector and the \mathbf{X} -axis. The angular dependence of $\psi(\alpha)$ is illustrated in Figure 5. The maximum phase retardation can be achieved when $\alpha = 0$ giving $\psi = \pi/4$. The relative phase shift Γ is plotted in Figure 5 as a function of the angle α between the electric vector and the \mathbf{X} -axis.

2.2.4 Electro-Optic Properties of ZnTe and GaP

It is instructive to introduce the parameters we use in this work. When a THz pulse interacts with the crystal lattice of an EO-crystal, a resonance at the transverse oscillation (TO) strongly modulates the complex index of refraction n_{THz} and the electro-optic

coefficient r_{41} . These effects induce a frequency dependence of the electro-optical phase retardation inside an electro-optical crystal.

2.2.4.1 Refractive index in the THz regime For THz frequencies, the complex dielectric function $\varepsilon(f)$ of an electro-optic crystal (ZnTe and GaP) can be obtained from the general case [61] by restricting the frequency sum of the electro-optic response to the lowest transverse optical (TO) lattice oscillation, and can be written as [60]

$$\varepsilon(f) = \varepsilon_{el} + \frac{S_0 f_0^2}{f_0^2 - f^2 - i\Gamma_0 f} \quad (39)$$

with f_j , Γ_j , and S_j being the eigenfrequency, damping constant and oscillator strength of the lattice oscillation j . We used the following fitting parameters as [62]:

ZnTe: $\varepsilon_{el} = 7.4$, $f_0 = 5.3$ THz, $S_0 = 2.7$, $\Gamma_0 = 0.09$ THz
GaP: $\varepsilon_{el} = 8.7$, $f_0 = 10.98$ THz, $S_0 = 1.8$, $\Gamma_0 = 0.02$ THz

The complex index of refraction is given by:

$$n(f) + i\kappa(f) = \sqrt{\varepsilon(f)} \quad (40)$$

2.2.4.2 Electro-optical coefficient in the THz regime The electro-optic coefficient r_{41} is also governed by the lattice oscillations (TO). It can be written as a function of frequency as follows [63]

$$r_{41} = d_E \left(1 + \frac{C f_0^2}{f_0^2 - f^2 - i\Gamma_0 f} \right) \quad (41)$$

In addition to the previously defined parameters f_0 and Γ_0 , we use the following for ZnTe and GaP [64, 65]:

ZnTe: $d_E = 4.25 \times 10^{-12}$ m/V, $C = -0.07$,
GaP: $d_E = 1.1 \times 10^{-12}$ m/V, $C = -0.53$,

2.2.4.3 Velocity difference between THz and NIR pulse in GaP and ZnTe

The phase and group velocities of a THz wave and a NIR pulse of a certain carrier frequency are matched only over a short THz frequency range [66]. A Ti:Sa laser pulse propagates with the group velocity

$$v_g = \frac{c}{n} \left(1 + \frac{\lambda}{n} \frac{dn}{d\lambda} \right) = \frac{c}{n + f \frac{dn}{df}} \quad (42)$$

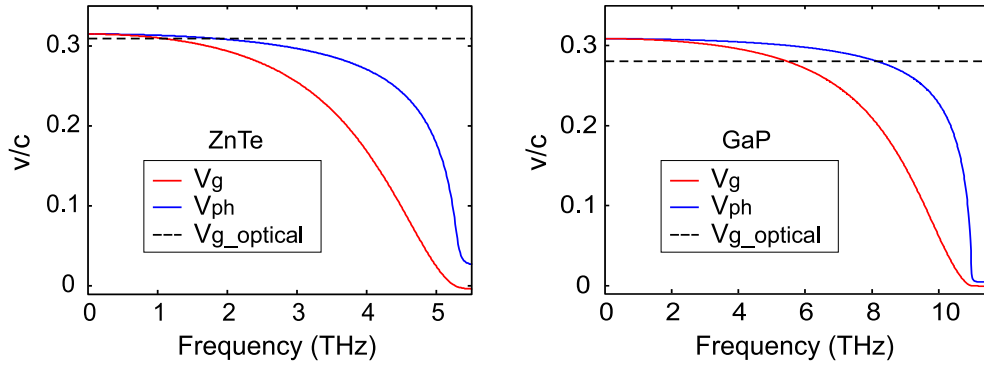


Figure 6: A comparison of phase and group velocities in ZnTe (left) and GaP (right) in the THz range.

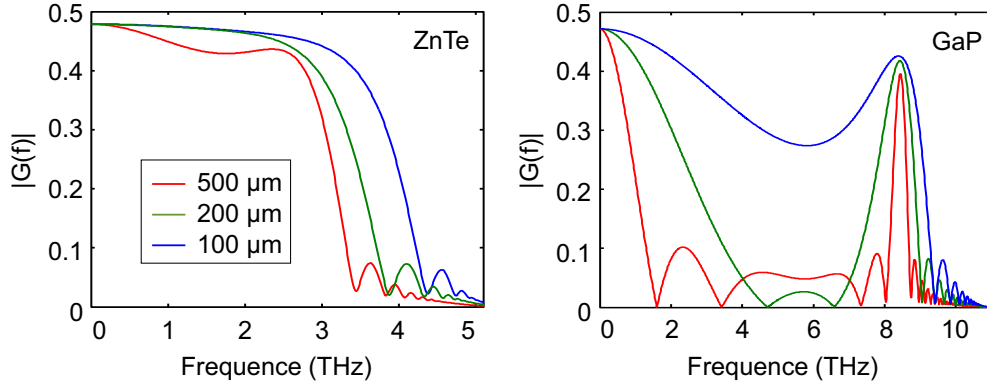


Figure 7: Electro-optic response functions of ZnTe and GaP in the THz frequency range for crystal thicknesses of 100 μm , 200 μm , and 500 μm .

which is lower than the phase velocity of the contributing harmonic waves. On the other hand, the index of refraction in the THz-regime is defined by 39 and 40. The phase and group velocities in ZnTe and GaP are presented in Figure 6 as function of frequency. Compared to the optical group velocity at 800 nm, the THz pulse propagates at a higher velocity at low frequencies, and there is a growing mismatch in velocity when approaching the TO resonance at 5.3 THz in ZnTe and 11 THz in GaP.

2.2.4.4 Electro-optic response function To account for all aforementioned effects, including phase-slippage, the frequency dependence of the refractive index, and the electro-optical coefficient in the THz regime, a response function depending on the frequency f and the crystal thickness d can be defined as [67]

$$G(f, d) = \frac{c}{(1 + n_{\text{THz}})\pi f \Delta n} \left[\exp\left(i2\pi f d \frac{\Delta n}{c}\right) - 1 \right] \quad (43)$$

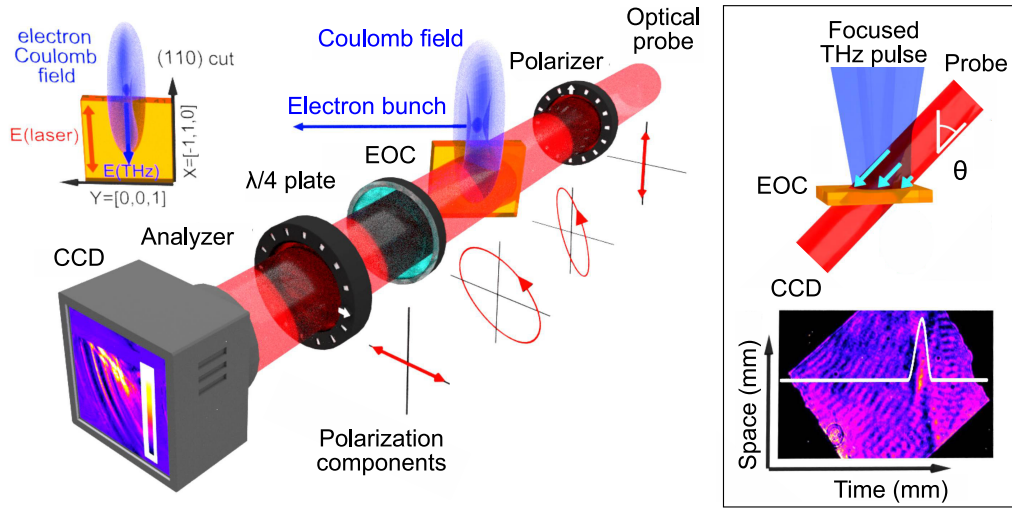


Figure 8: A simplified view of the electro-optic detection scheme: A linearly polarized short laser probe propagates through an electro-optic crystal in the presence of a longitudinally contracted Coulomb field of a transient relativistic electron bunch. The polarization state of the probe beam becomes elliptical and is then controlled by a wave plate. An analyzer splits the s- and p-components of the elliptical polarization to be imaged on a CCD to measure the intensity modulation. The upper-left corner shows the orientation of the polarization components leading to the largest electro-optical effect when using a ZnTe crystal cut in the (110) plane. The inset on the right shows the principle of time-to-space mapping of a transient THz pulse via spatial encoding due to the oblique incidence of the probe.

where the index difference $\Delta n = n_{\text{THz}} - c/v_g$. The EO response function of ZnTe is shown in Figure 7 for various crystal thicknesses, where the TO resonance sets an upper limit to the accessible frequency range. The higher TO resonance frequency in GaP allows for a higher frequency range. A thin crystal ($d \leq 100 \mu\text{m}$) should be used to exploit this capability, otherwise, ZnTe is favored due to its higher EO coefficient r_{41} .

2.3 Electro-optic signal detection

In the following, we address the question of how to experimentally measure the retardation induced within an electro-optic crystal by a transient electric field of the THz wave during their interaction. To achieve this, we describe the technique used to encode the time-dependent retardation onto the laser probe pulse and present the method used to convert the retardation into a detectable signal.

In order to extract temporal information, such as measuring the THz pulse duration

as demonstrated in Chapter 3, we employ a spatially resolved electro-optic setup [68]. In this setup, the temporally induced birefringence is encoded within the laser probe as spatial intensity modulations. The geometry is depicted in the inset of Figure 8, where a THz pulse is focused perpendicularly onto the EO crystal, while a linearly polarized short laser probe is directed towards the EO crystal at an angle θ relative to the crystal surface's normal. Since one side of the laser probe arrives at the EO crystal before the other side, different temporal components in the crystal are observed by different spatial components of the laser. The analyzer converts the spatial modulation of the polarization into a spatial intensity modulation, which is detected by the CCD camera. The mapping between the time coordinate t and the spatial coordinate x can be readily obtained

$$t = \frac{x}{c} \tan(\theta) \quad (44)$$

where θ is the angle (in air) between the two beams. The total window of time, $\Delta T = w \tan(\theta)/c$, probed during the measurement is determined by the width w of the incident probe beam.

To obtain the signal, we consider a collimated laser probe beam exiting the ZnTe crystal and passing through a quarter-wave plate whose main axes are oriented at $\pm 45^\circ$ with respect to the horizontal direction. An analyzer separates the two polarization components of the laser beam to be imaged on a CCD to measure the signal intensity. The analyzer will then be rotated by 90° and the shot will be repeated to obtain the orthogonal polarization component. This configuration is called a balanced¹ detection scheme and is shown in Figure 8 for the case of detecting the transient electric field of electron bunches. In the absence of an external electric field, the laser probe pulse passes through the EO crystal without changing its polarization state. The quarter-wave plate transforms the linearly polarized probe into a circularly polarized one. The analyzer guides the two orthogonal components of a circular wave of equal intensity toward the camera. Consequently, the signal difference vanishes. However, in the presence of a sufficiently strong THz field, the phase retardation induced inside the EO crystal modifies the polarization of the laser probe into an elliptically polarized state, leading to an imbalance between the two measured signals on the camera.

Here, we summarize the treatment in [69, 70] based on Jones calculus. Laser light with a horizontal or vertical polarization is represented by the vectors

¹In a conventional balanced detection scheme, instead of an analyzer, a Wollaston prism is used, which separates the two orthogonal components to be measured simultaneously by two diodes or two cameras to obtain the signal in a single shot. For this purpose, two intensity-sensitive detectors capable of sustaining large background intensities without damage or saturation are required.

$$\mathbf{E}_h = E_{\text{laser}} \begin{pmatrix} 1 \\ 0 \end{pmatrix} \quad \text{or} \quad \mathbf{E}_v = E_{\text{laser}} \begin{pmatrix} 0 \\ 1 \end{pmatrix} \quad (45)$$

and the rotation of the polarization plane can be described by the matrix

$$\mathbf{R}(\phi) = \begin{pmatrix} \cos \phi & -\sin \phi \\ \sin \phi & \cos \phi \end{pmatrix} \quad (46)$$

The Jones matrix of a quarter-wave plate with fast axis in horizontal direction is

$$\mathbf{Q} = \exp(-i\pi/4) \cdot \begin{pmatrix} 1 & 0 \\ 0 & i \end{pmatrix} \quad (47)$$

When an EO crystal of thickness d is subjected to a strong electric field, it acquires the indices $n_s(\alpha) = n_1(\alpha)$, $n_f(\alpha) = n_2(\alpha)$. The Jones matrix of the EO crystal is given by

$$\mathbf{EO}(\alpha) = \begin{pmatrix} \exp(-i n_s(\alpha)wd/c) & 0 \\ 0 & \exp(-i n_f(\alpha)wd/c) \end{pmatrix} \quad (48)$$

By separating out the average phase change $\phi = (n_s + n_f)wd/c$ we get

$$\mathbf{EO}(\alpha) = \begin{pmatrix} \exp(-i\Gamma(\alpha)/2) & 0 \\ 0 & \exp(+i\Gamma(\alpha)/2) \end{pmatrix} \cdot e^{-i\phi} \quad (49)$$

where Γ is given by equation 38. Since only the intensities are calculated, the overall phase factor $\exp(-i\phi)$ can be omitted.

In order to fully simulate the system, the Jones matrices of all optical elements in the path of the laser beam between the EO-crystal and the detector have to be multiplied. To calculate the electric field strength, the electric field of the laser beam $\mathbf{E}_{\text{laser}}$ is rotated into the principle axis system of the EO crystal, then passed through the crystal and finally rotated back into the laboratory system (X, Y). Mathematically, this can be described as a product of matrices:

$$\begin{aligned} & \mathbf{R}(-\psi(\alpha)) \cdot \mathbf{EO}(\alpha) \cdot \mathbf{R}(\psi(\alpha)) \cdot \mathbf{E}_{\text{laser}} \\ &= \begin{pmatrix} 1 & 0 \\ 0 & 1 \end{pmatrix} \cos(\Gamma/2) - i \begin{pmatrix} \cos(2\psi) & \sin(2\psi) \\ \sin(2\psi) & -\cos(2\psi) \end{pmatrix} \sin(\Gamma/2) \cdot \mathbf{E}_{\text{laser}}, \end{aligned} \quad (50)$$

where the angle ψ_α is given by equation 37.

Crossed-polarizer setup The simplest setup for electro-optic detection is where a horizontally polarized laser beam passes through the EO crystal and then through a vertical polarizer in front of the detector. The electric field strength E_{det} at the detector can be calculated by multiplying the electric field vector of the horizontally polarized laser beam \mathbf{E}_h by the rotated matrix of the EO crystal (equation 50). In this system, the vertical polarization component \mathbf{E}_v is calculated

$$\begin{aligned} E_{\text{det}} &= \begin{pmatrix} 1 & 0 \end{pmatrix} \cdot \mathbf{R}(-\psi) \cdot \mathbf{EO}(\alpha) \cdot \mathbf{R}(\psi) \cdot \mathbf{E}_{\text{laser}} \begin{pmatrix} 1 \\ 0 \end{pmatrix} \\ &= -iE_{\text{laser}} \sin(2\psi(\alpha)) \sin\left(\frac{\Gamma(\alpha)}{2}\right) \end{aligned} \quad (51)$$

and the intensity at the detector I_{det} can be calculated as:

$$I_{\text{det}}(\alpha) = \frac{c\varepsilon_0}{2} |E_{\text{det}}|^2 = \frac{c\varepsilon_0}{2} E_{\text{det}}^2 \sin^2(2\psi(\alpha)) \sin^2\left(\frac{\Gamma(\alpha)}{2}\right) \quad (52)$$

for the maximal electro-optic effect $\alpha = 0$ giving $\psi = \pi/4$ and the detected intensity is

$$I_{\text{det}}(\alpha) = \frac{c\varepsilon_0}{2} E_{\text{det}}^2 \sin^2\left(\frac{\Gamma(\alpha)}{2}\right) = \frac{c\varepsilon_0}{2} E_{\text{det}}^2 \sin^2\left(\frac{\omega d}{2c} n_0^3 r_{41} E_{\text{THz}}\right) \quad (53)$$

For small $\Gamma \ll 1$ the intensity is proportional to E_{THz}^2 . In practice, a small background leakage is recorded by the detector even when the two polarizers are fully crossed. Some residual intensity in the system occurs due to imperfections in the EO crystal and mechanical stresses, which can be compensated by a quarter-wave plate between the EO crystal and the analyzer. Other factors can lead to higher background signals, such as imperfect polarization of the input beam, uncompensated residual birefringence, scattering in the crystal, and imperfect polarization in the analyzer. The background signal I_{bg} is proportional to the laser intensity $\frac{c\varepsilon_0}{2} E_{\text{laser}}^2$ and can be added:

$$I_{\text{det}} = I_0 \cdot \sin^2(\Gamma/2) + I_{\text{bg}} \quad (54)$$

Balanced detection In the crossed-polarizer scheme, the detected signal is proportional to the THz intensity. This means that we can only obtain the amplitude but not the phase of the THz pulse. We can add a quarter-wave plate behind the EO crystal and a Wollaston prism (replaced by the analyzer) to set up a balanced scheme

as shown in Figure 8. This scheme enables the detection of both the phase and the amplitude of the electric field and provides much better sensitivity than the crossed polarizer setup. The fast optical axis of the quarter wave plate is rotated by 45° with respect to the polarization direction of the laser beam so that the wave becomes circularly polarized. The intensity of the observed background at either analyzer position is $I_{h,v} = 1/2I_0$. Since the quarter-wave plate is inserted in the optical beam path, we need to rotate the beam into the main coordinate system of the quarter-wave plate, apply the appropriate matrix, and rotate it back. Thus equation 50 becomes:

$$E_{\text{det},v} = \begin{pmatrix} 0 & 1 \end{pmatrix} \cdot \mathbf{R}(-\pi/4) \cdot \mathbf{Q} \cdot \mathbf{R}(\pi/4) \cdot \mathbf{R}(-\psi) \cdot \mathbf{EO}(\alpha) \cdot \mathbf{R}(\psi) \cdot \mathbf{E}_{\text{laser}} \begin{pmatrix} 1 \\ 0 \end{pmatrix} \quad (55)$$

For maximal electro-optic effect i. e. $\alpha = 0$ making $\psi = \pi/4$, the field and the intensity at the detector becomes:

$$E_{\text{det},v} = \frac{E_{\text{laser}}}{\sqrt{2}} (\cos(\Gamma/2) - \sin(\Gamma/2)) \quad (56)$$

$$\begin{aligned} I_{\text{det},v} &= \frac{c\varepsilon_0}{2} E_{\text{det},v}^2 + I_{\text{bg}} \\ &= \frac{c\varepsilon_0}{2} \frac{E_{\text{laser}}^2}{2} |\cos(\Gamma/2) - \sin(\Gamma/2)|^2 + I_{\text{bg}} \\ &= \frac{I_{\text{laser}}}{2} (1 - \sin(\Gamma)) + I_{\text{bg}} \end{aligned} \quad (57)$$

For $\Gamma \ll 1$ the intensity $I_{\text{det},v}$ is proportional to E_{THz} but on a large background ($E_{\text{THz}}^2/2$). When the analyzer is orientated to pass the horizontal polarization components, the latter can simultaneously be measured:

$$I_{\text{det},h} = \frac{I_{\text{laser}}}{2} (1 + \sin(\Gamma)) + I_{\text{bg}} \quad (58)$$

Thus the intensity difference seen by the balanced detector is:

$$I_{\text{det},h} - I_{\text{det},v} = I_{\text{laser}} \sin(\Gamma) \quad (59)$$

For the THz field reported in this work $E_{\text{THz}} \sim 10 \text{ MV/m}$, the phase retardation is $\Gamma \ll 1$. Since the balanced detector signal scales linearly with the electric field E_{THz} of the THz pulse, it is therefore much larger than the signal obtained in the crossed-polarizer setup which is proportional to Γ^2 . However, a detector with a high

dynamic range that does not saturate at half the laser power transmitted through the EO crystal is required.

It is worth mentioning that in some cases balanced detection is not always possible, especially in environments where a single shot detection is necessary, as in accelerator facilities. Other variations of the electro-optic setup can be applied, such as near-crossing polarization.

3 Electro-optic detection of THz radiation

There are several well-known processes in which laser pulses transfer energy to electrons during their interaction with the plasma. The energy transfer can be realized via various pathways as briefly presented in section 2.1.1. Examples are nonlinear forces exerted by the laser pulse, Lorentz force, vacuum heating, etc [50, 71]. Depending on the heating mechanism, the energy gained by the electrons varies from keV to several MeVs, as we will see in the next chapter. Additionally, for ultrathin targets with a thickness comparable to the longitudinal extent of the incident laser pulse, energetic electrons can propagate through the target without significant energy loss and exit at the rear surface, thus, creating a strong quasistatic sheath field. The resulting sheath field is accounted for ionizing and accelerating the positive charges to several MeVs via the TNSA mechanism [46]. The dynamics of the charged particles during the intense laser-foil interaction can include the escape of the electrons with subsequent current generation along the target surface to neutralize the charge void, the formation of a plasma sheath and acceleration of the sheath charges, etc., all leading to the generation of electromagnetic radiation [16, 18, 72]. This radiation can be coherent and/or incoherent, depending on the generation process. The characterization of the emitted radiation can provide useful information about the spatio-temporal dynamics of sources that would otherwise be complex to diagnose.

The first comprehensive observation of THz radiation at the target rear surface was reported prior to this thesis project [18]. Strong THz emission at large angles to the target normal was observed by employing electro-optic techniques to record the temporal and spectral features of the THz radiation. The results showed sub-picosecond pulses with peak powers reaching up to the gigawatt (GW) level and a relatively broad spectrum containing many octaves of frequencies [73, 74]. In this chapter, we present a comprehensive study of the THz radiation at the rear surface of the target, including temporal and spectral features and angular distributions of the emission. The temporal dynamics of the THz emission is acquired using a single shot noncollinear electro-optic setup built outside the interaction chamber, which ensures a clean detection away from the interaction.

3.1 Experimental setup

The experiments on the interaction of intense laser pulses with thin solids have been performed at the JETI40 facility (see appendix 8.B) at the Institute for Optics and

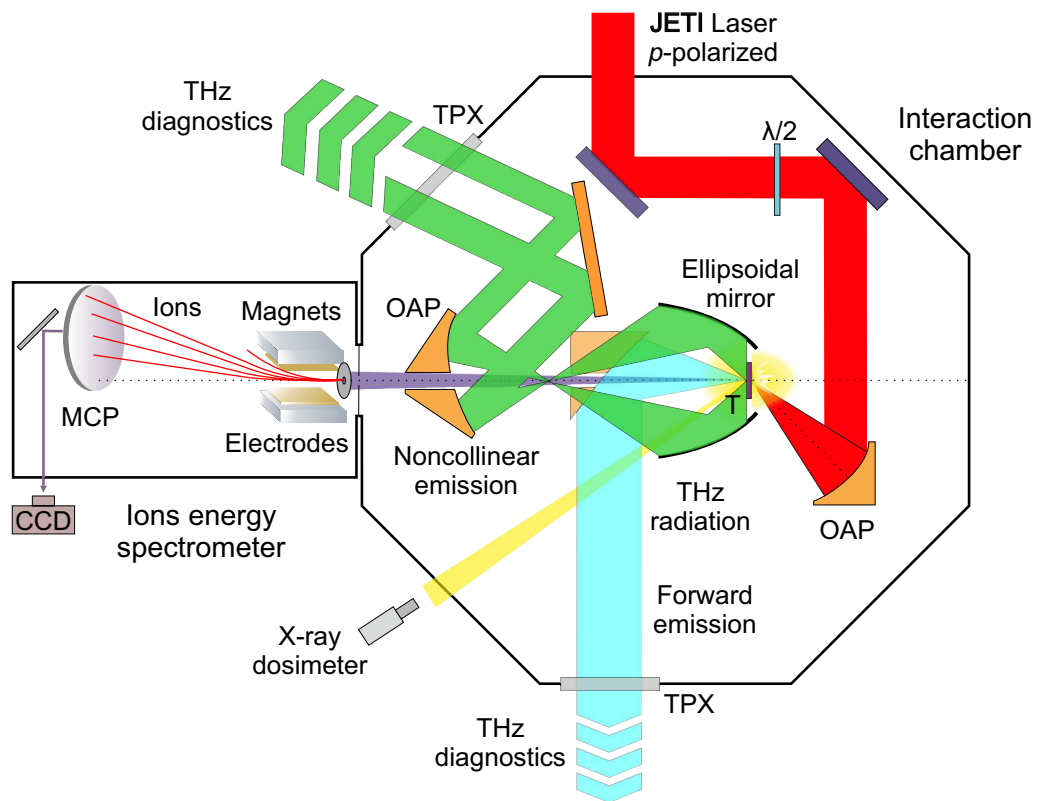


Figure 9: A simplified schematic of the experimental setup for collecting the THz radiation during relativistic laser-thin solid interaction. Ultra-short laser pulses are focused onto a thin metal foil target at an angle of incidence of 45° , achieving relativistic intensities above 10^{19} W/cm^2 . The THz radiation is generated during the interaction due to the dynamics of the accelerated charged particles. Part of the THz radiation emitted from the rear surface of the target is collected separately using two geometries: an ellipsoidal mirror (non-collinear emission NE in green) and a parabolic mirror (forward emission FE in cyan). The collected THz light is then collimated and relayed outside the interaction chamber to the THz diagnostics. Additional diagnostics: a Thomson parabola ion spectrometer and an X-ray dosimeter.

Quantum Electronics in Jena. The experimental setup is presented in Figure 9 where laser pulses are guided inside the interaction chamber in vacuum using dielectric mirrors. The polarization state of the laser is controlled by a 4-inch half-wave plate placed in the collimated beam just before the focus. We consider the polarization state to be p-polarized when the electric field component oscillates parallel to the plane of incidence, while s-polarized light oscillates perpendicular to this plane. Next, the laser pulses are focused by a 4-inch 45° ($f/2$) off-axis parabolic mirror (OAP) onto a thin metallic target. The focus spot size achieved is about $12 \mu\text{m}^2$ at $(1/e^2)$ and is optimized using adaptive optics while being imaged onto a CCD (16-bit) using a

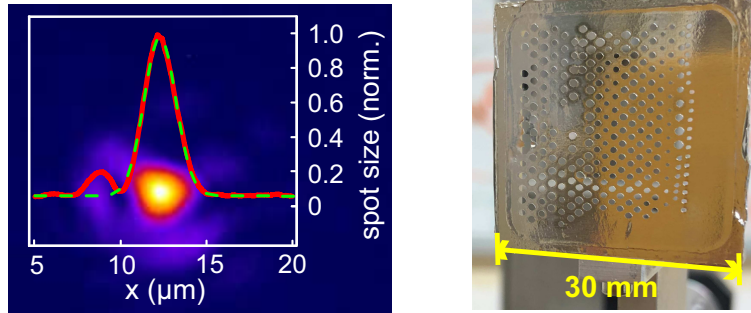


Figure 10: (Left) Laser focal spot obtained from an $\sim f/2$ off-Axis parabolic mirror (OAP) after optimization using adaptive optics. (Right) An aluminum foil mounted on a motorized holder pictured after one of the experiments, different hole sizes are due to the movement of the target through the focus region.

microscope objective placed after the focal region, The resulting focal spot is shown in Figure 10. The pulse energy on the target is monitored by measuring the energy after the vacuum compressor using a calibrated energy meter on a shot–shot basis and is estimated to be around 650 mJ on target with a minimum pulse duration of about 32 fs (FWHM). The calculated intensity, therefore, is above 1×10^{19} W/cm². In this work, we mainly use aluminum and titanium foils with a thickness of 5 μm and lateral dimensions of 30 × 30 mm². Target foils are stretched in a special frame by exploiting the different thermal expansions of the frame and the foil. The target frame is mounted on a 3D stepper motor configuration with x , y , and z translation stages as well as a rotation stage. The energy of the accelerated protons emitted in the normal direction to the target is measured in a single-shot Thomson parabola spectrometer (TPS) (see appendix 8.D) and used to gauge the shot-to-shot fluctuations.

To well set the various properties of the laser, several diagnostics are employed, such as two third-order autocorrelators to measure pulse duration and picosecond contrast (Sequoia) [75], a fast photo-diode for the nanosecond pulse contrast, an interferometer for the pulse front tilt, calibrated energy detectors to measure the pulse energy at different locations down the beam line, and, finally, near- and far-field detectors to monitor the beam positions. The contrast ratio of the final pulse before the interaction chamber is about 10^{-9} within 1 ns of the main pulse and is presented in Figure 11 along with the laser beam profile.

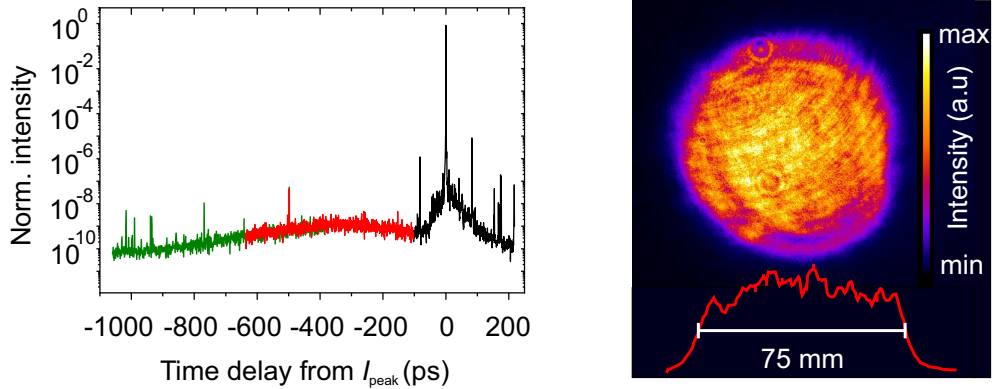


Figure 11: (Left) Contrast scans of the JETI laser system using a third-order autocorrelator. The scan consists of smaller sweeps due to the time limitation of the delay line inside the autocorrelator. A clear ASE-pedestal with a contrast of around 10^{-9} was measured within 1 ns of the main pulse. (Right) A beam profile in the near field of the JETI was captured with a CCD camera and shows a beam diameter of around 75 mm at FWHM with a slightly inhomogeneous profile.

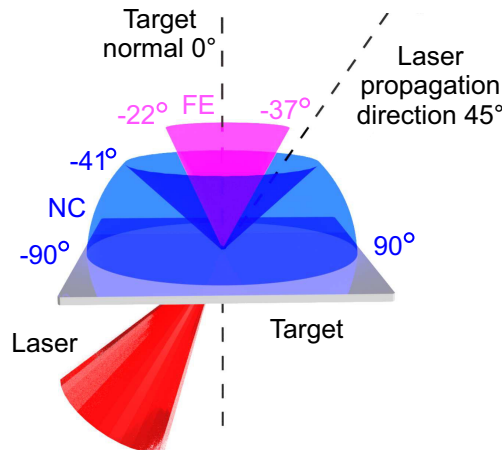


Figure 12: The collection angles of the THz emission via reflective optics behind the target as depicted in Figure 9. An ellipsoidal mirror was used to collect the non-collinear emission (blue), while a parabolic mirror was used separately for the forward emission (pink).

3.2 Electro-optic detection of THz radiation

We collected the THz radiation emitted from the rear surface of the metallic foil target in two separate geometries as illustrated in Figures 9 and 12 with a total solid angle of about 5.12 sr . We refer to the collected emission in the range of $\pm 90^\circ$ to $\pm 41^\circ$ as the noncollinear emission (NE) and collect it using an ellipsoidal mirror. Additionally,

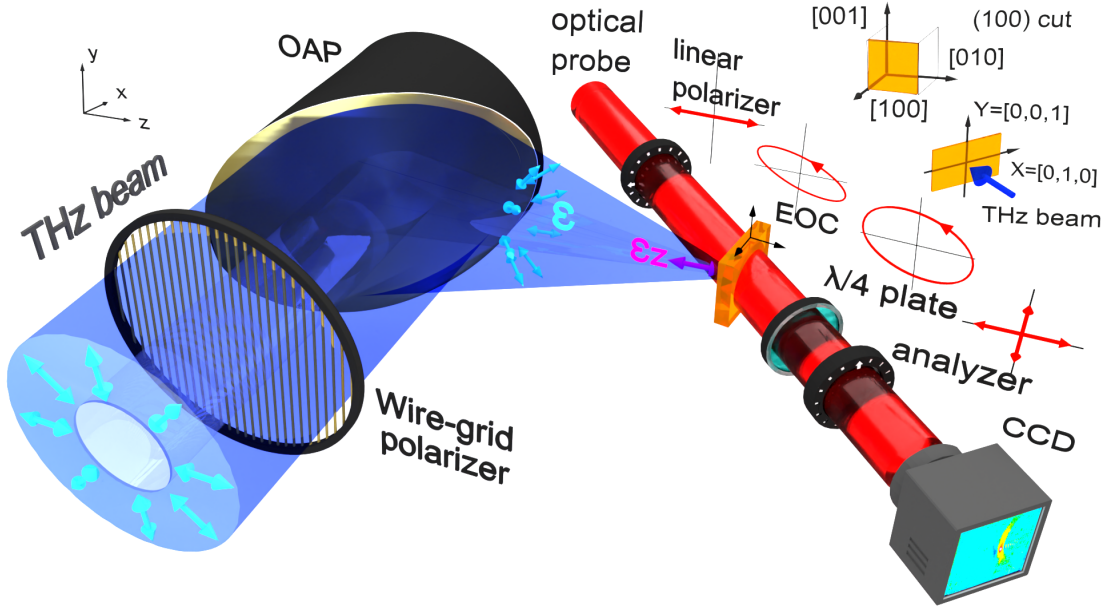


Figure 13: Electro-optical setup for detecting THz pulses during the interaction of ultrashort laser pulses with thin foils. The collected and collimated THz radiation as shown in Figure 9 is focused onto an electro-optic (EO) crystal using an off-axis parabola (OAP). The temporal waveform of the THz pulse is obtained by a single shot noncollinear EO detection, where the horizontal axis of the recorded image provides temporal information and the vertical axis provides the spatial profile of the THz spot. A wire-grid polarizer can be inserted in the collimated beam to determine the polarization state of the THz radiation. Corner: an example of the crystal orientation of a (100) cut GaP used to detect the longitudinal polarization component ϵ_z of the THz pulses at the focus.

we define the emission in the angular range from 0 up to $+37^\circ$ and down to -22° as forward emission (FE) and collect it using an off-axis 3-inch diameter ($\sim f/1$) parabola. After collection, the THz radiation is collimated by an additional parabolic mirror and steered out of the vacuum chamber through a high resistive float zone silicon (HRFZ-Si) or a TPX window using metallic mirrors. The collimated THz beam from a given collection geometry is then focused onto an electro-optic crystal using a 4-inch off-axis parabolic mirror to perform temporal and spectral measurements.

Figure 13 shows the experimental setup employed for the detection of THz emission based on a single-shot noncollinear pump-probe electro-optic EO technique. The THz radiation is focused perpendicularly onto a ZnTe EO crystal. The external field acts as a transient bias and induces time-dependent birefringence in the crystal, which is subsequently probed by a laser pulse. The probe pulse is a 1% split from the main laser beam, temporally delayed using a remote-controlled kinematic stage, and sent

on the EO crystal at an angle of θ with respect to the THz incidence. In this case, the linearly polarized probe pulse experiences an induced ellipticity [73], which is then converted into an intensity modulation via a quarter-wave plate with a polarizer on a CCD camera. Due to the skewed geometry between the THz and the probe, one side of the optical beam reaches the EO crystal earlier than the other. Thus, the temporal profile of the transient birefringence and hence the temporal dynamics of the THz emission can be mapped on the horizontal spatial profile of the optical probe. The time window (t) as presented previously is defined by the diameter (w) of the optical beam and the angle θ between the optical and THz pulse at the EO crystal [68].

$$t = \frac{w}{c} \tan(\theta) \quad (60)$$

The signal of the detected intensity is directly proportional to the intensity of the THz electric field (crossed-polarizer detection scheme). We begin by estimating the crystal response function, which accounts for both absorption and velocity mismatch within the electro-optic (EO) crystal, as detailed in Section 2.2.4.4. Subsequently, we incorporate this response function into the Fourier domain analysis. The outcomes derived from the inverse transformation of this data enable us to estimate the temporal waveform and spectral characteristics of the THz pulse. For a linearly polarized optical pulse, the phase retardation induced is given by Equation 38:

$$\Gamma_{(\theta)} = \frac{\omega d}{2c} n_0^3 r_{41} E_{\text{THz}} \sqrt{1 + 3 \cos^2 \theta} \quad (61)$$

We employ different electro-optic crystals of various thicknesses for the detection of THz pulses in NE and FE geometries due to the variance in radiation energy and crystal sensitivity. For measurements in the FE direction, a 500 μm ZnTe (zinc telluride) crystal and for the NE direction, a 100 μm GaP (gallium phosphide) crystal were employed [76]. The corresponding minimum detectable pulse durations are 250 and 103 fs for the ZnTe and GaP crystals, respectively.

3.3 Temporal structure of the THz emission

We present the temporal structure of the detected THz pulses in the forward and non-collinear directions separately, as shown in Figure 14. We detected multiple pulses with variable amplitudes and durations in the time domain for both detection geometries. The duration (FWHM) of each pulse is sufficiently longer than the inverse detection bandwidth of the diagnostics defined by the electro-optic function of the crystal. In

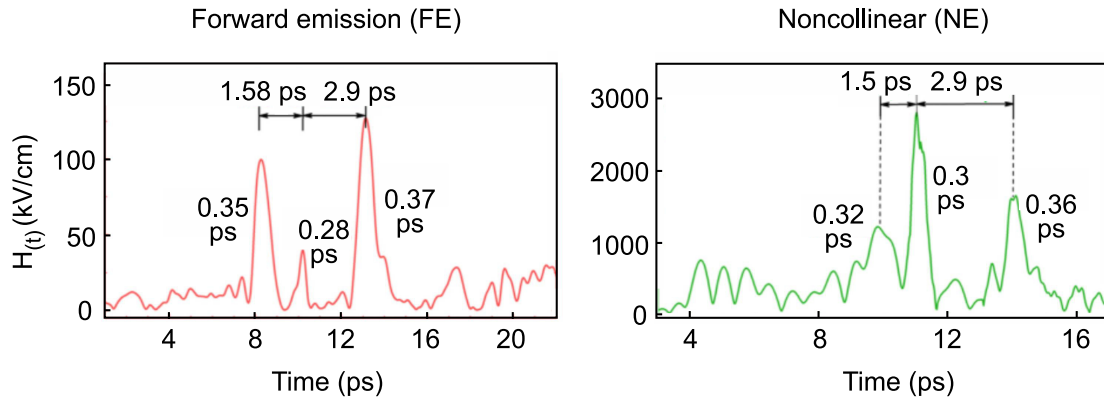


Figure 14: Recorded transient structure of the THz radiation obtained from the electro-optic measurements in a single shot during the intense laser-foil interaction. Multiple pulses with comparable pulse durations and temporal delays are present in both detection geometries as shown on the left: the collected radiation in the forward direction (FE; pink area in Figure 12). On the right: the wide-angle emission (NE; blue area in Figure 12).

the forward direction presented in the left panel, at least three pulses of various field strengths can be identified. These pulses have a duration width of around 0.34 ps . Likewise, the temporal structure of the noncollinear emission presented in the right panel also reveals multiple pulses with similar duration widths but significant field strengths. The field amplitudes of the longitudinal components measured with the GaP $\langle 100 \rangle$ crystal reached an unprecedented $\sim 3 \text{ MV/cm}$ [11]. At such high signals, broadband silicon attenuators are inserted in the collimated beam path to avoid saturation or over-rotation of the EO signal. Similar to the forward emission, the temporal structure reported in the noncollinear direction extends over several picoseconds. It is worth noting that the separation between the detected pulses does not match any extra distance due to internal reflections in the beam path inferring the detection of true distinct pulses.

Additionally, we evaluate the spectral range of the detected pulses from the Fourier transform of the temporal domain. Figure 15 shows the frequency of the THz pulses in both detection geometries, forward emission on the left and wide-emission (non-collinear) on the right. The detected pulses cover a similar frequency range of around 1 THz . Since the separation between the pulses, the temporal widths, and the frequencies are comparable for both emission geometries regardless of the different collection optics, this suggests common and possibly periodic-generation process along various directions.

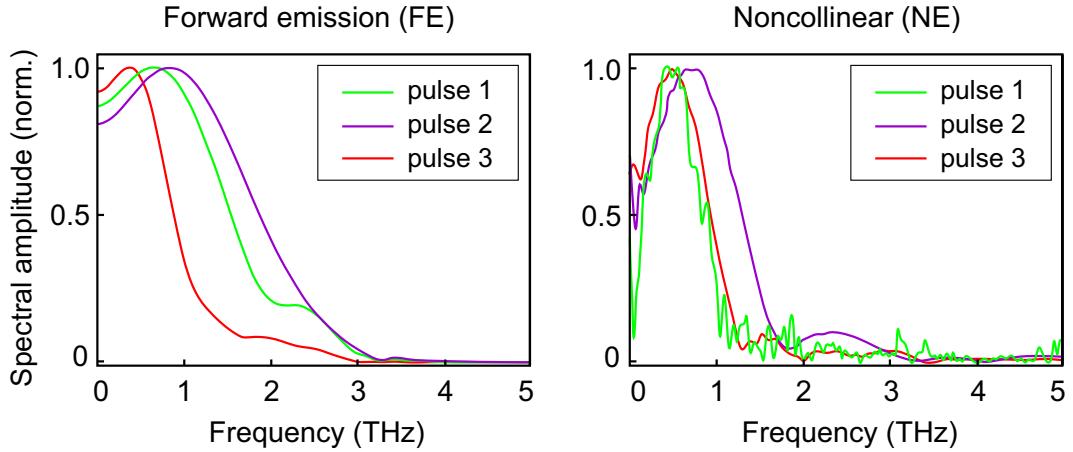


Figure 15: Spectral intensity of the three major THz pulses presented in Figure 14 is obtained from the Fourier transform of the temporal measurements.

3.4 Polarization state of the THz emission

Although we measured the longitudinally polarized THz radiation at the focus due to focusing a radially polarized beam, we separately measured the polarization of the radiation. To this end, we inserted a wire-grid (WG) polarizer in the collimated beam path as shown in Figure 13, and measured the total transmitted THz power for various rotation angles of the WG using a pyrometer. The results are presented in Figure 16, which shows that the collected emission is predominantly radially polarized in both geometries. This can be explained when we discuss the generation mechanisms responsible for the THz emission in Chapter 5.

The obtained outcome aligns well with the reported temporal measurements. When focusing a radially polarized beam, compared to linear polarization, a strong and tightly focused longitudinal field is achieved as the longitudinal components will be added constructively and provide a finite field amplitude, while the transverse components cancel, as illustrated for radially polarized Bessel-Gaussian and Laguerre-Gaussian beams [77–79]. The ratio between the longitudinal to the transverse field is given by the numerical aperture of the focusing optics. The numerical aperture in our case is $NA = 0.33$, experimental measurements yielded a ratio of 0.5, while theoretical estimates indicated a ratio of 0.43.

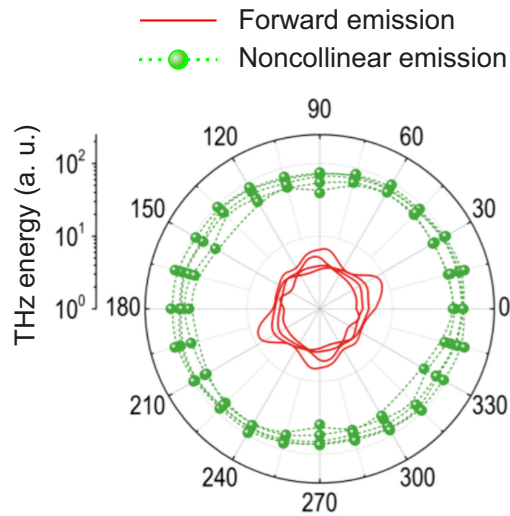


Figure 16: Polarization state measurements of the detected THz radiation using selected wire grid polarizers. The radiation from both collection geometries is radially polarized. Red line: forward emission, green circles: noncollinear emission.

3.5 Angular distribution of terahertz radiation

It is instructive to verify the angular distribution of the THz emission and compare it with that of charged particles. For this purpose, we reconstructed the angular distribution of the THz emission from the back surface of the target by inserting a motorized beam profiler in the collimated beam path before the OAP shown in Figure 13. The beam profiler is a motorized metallic plate with a $5 \times 5 \text{ mm}^2$ window translated in the vertical and horizontal directions in the collimated beam. The transmitted energy is then measured using a calibrated pyroelectric detector placed at the focus. The window size provides a compromise between diffraction effects at long wavelengths and adequate spatial resolution. By careful reconstruction, each section of the collimated beam can be associated with an absolute angle on the ellipse, and similarly for the forward emission. Finally, the two measurements are combined to obtain a full and true three-dimensional representation of the THz emission from the target rear surface.

Figure 17 shows the angular distribution pattern of the THz radiation emitted from the rear surface of the target during the interaction with an ultra-short high-power laser pulse. The reconstructed 3D profile demonstrates a strong asymmetry with multiple peaks and a variety of signal amplitudes, indicating potentially multiple excitation processes. The THz profile consists of a weak but homogeneous background emission dominated by strong directional emission closer to the laser propagation direction, with signal strengths many times higher than the background level. Such multiplicity

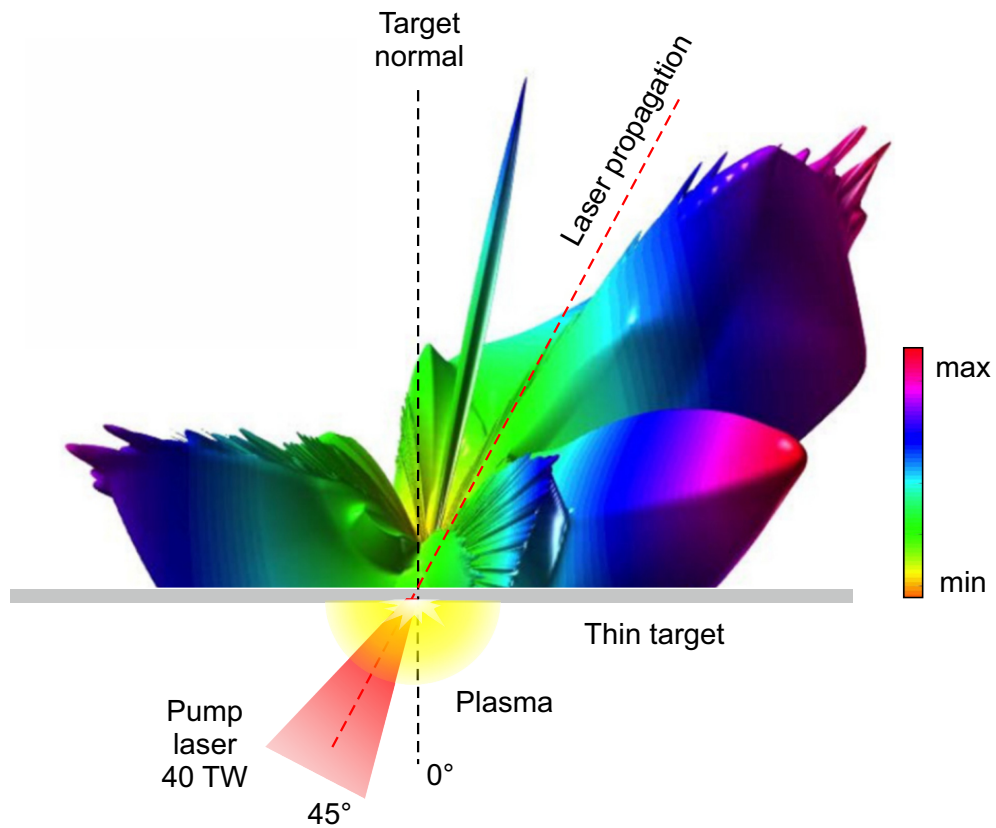


Figure 17: Experimentally measured angular distribution of the terahertz radiation during the intense laser-foil interaction. The 3D profile is reconstructed from the collected THz emission at the target rear surface in the two geometries shown in Figure 12. An ultrashort laser pulse is focused on a thin metal target at 45° reaching relativistic intensity above 10^{19} W/cm^2 . The detected emission of THz radiation is asymmetric, with high-energy peaks around the laser propagation direction indicating a considerable contribution of charged particle dynamics. A complete 360-degree perspective can be seen in [80].

implies a significant contribution from sub-picosecond dynamics, such as the ejection of particle bunches from the rear surface of the target, as the dominant source of THz pulses rather than surface currents [81, 82].

3.6 Conclusion

So far we have examined the emission of the THz radiation away from any signal contamination or interference from the interaction. We presented a true 3D angular distribution of the terahertz emission from the target rear surface, which shows that the emission is asymmetric with multiple peaks at various energy levels. Similarly, the

temporal measurements of the same emission show multiple pulses with variable amplitudes and durations in the time domain for both noncollinear and forward emission geometries, confirming the features noted in the 3D beam profile. Additional testing revealed that the detected THz radiation is mainly radially polarized. The directionality and the multiplicity of the detected THz pulses can be a strong indication of a characteristic contribution of charged particle dynamics as the main generation process of the THz radiation. It can be expected that the emission of electromagnetic radiation in the THz spectral regime is related to the timescale of particle dynamics. It would therefore be advantageous to characterize the emission of charged particles under the same conditions during the interaction. For this purpose, a complete characterization of particle emission with quantitative measurements will be provided in the next chapter, which will help to explain the underlying physics behind the detected subpicosecond emission.

4 Characterization of Charged particle emission

During the intense laser-foil interaction, and depending on the experimental parameters, highly directional hot electron emission with a charge up to \sim nC can be generated via various processes, which subsequently can lead to ion acceleration [51, 83]. Such dynamics could be primarily responsible for the generation of the EM radiation [84] presented in the previous chapter. Quantitative measurements of particle emission are indeed needed to better define the generation mechanisms of EM radiation. Two main processes may lead to coherent² emission of electromagnetic radiation from the back surface of the target [85]. These are (1) transition radiation (TR) due to hot electron bunches crossing the plasma-vacuum boundary at the rear surface and (2) sheath radiation (SR) due to plasma sheath formation, expansion, and the resulting ion acceleration process in the target normal direction. In this chapter, we provide a comprehensive parametric characterization of the charged particle emission from the rear side of the target, including energy spectra, temperature, and angular distributions.

4.1 Angular distribution of electron emission

The spatial distribution of the electron emission behind the target can provide insight into the dominant energy coupling mechanism at the front surface during the laser-target interaction. For this purpose, we utilized highly sensitive radiochromic films [86] and CR39 plastic detectors [87] to reconstruct the spatial distribution of the electron and proton emissions, respectively.

The electron beam profile was acquired using a stack of radiochromic films (RCF) shaped as a semicircle behind the target, covering the entire back side of the target in the horizontal plane and 17° in the elevation plane. The stack consists of 9 RCFs with aluminum sheets of various thicknesses in between, enabling an energy-resolved measurement. Figure 18 provides a visual representation of the RCF films positioned behind the target, where both the target normal and the laser propagation directions are depicted. The dark rectangles in the middle are holes in the films through which the ions can pass toward the ion spectrometer. Since the presented measurements required a large number of shots in order to accumulate a sufficient signal on the films, we used the proton signal to check the consistency of the interaction.

In order to construct the full energy-resolved angular distribution, we scanned the

²The coherent nature of the THz emission will be presented in Chapter 5.

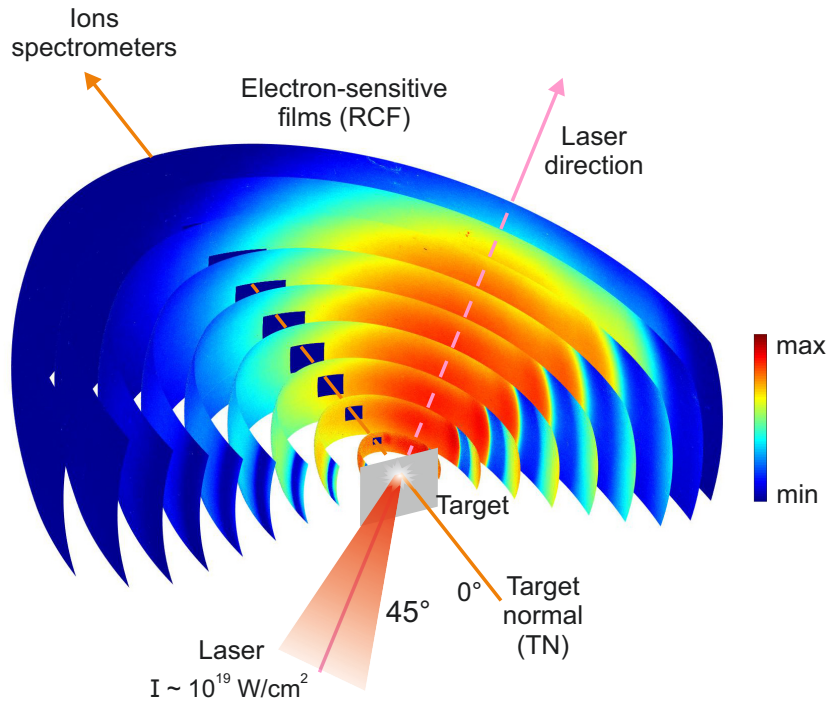


Figure 18: A 3D view of the semi-circular stack behind the target, consisting of 9 electron-sensitive Gafchromic films with metallic filters in between (not shown). Rectangular holes along the target's normal direction were made for passing the accelerated ions to the spectrometer.

RCFs and assigned angular values as seen in the scans in Figure 19. Here we present the signal intensity on the 9 films, each corresponding to a specified energy range, with angular values ranging from 0° in the middle to $\pm 90^\circ$ in the lateral and $\pm 17^\circ$ in the vertical directions. On the first film behind the target (top), we see a more or less uniform distribution of low-energy electrons of 30 – 125 keV. As the accumulated thickness of the Aluminum filter increases in the successive layers, this uniform distribution narrows as the energetic electrons become more concentrated toward the laser propagation direction. A rough estimate of the maximum electron energy in target normal direction, where the electrons induce the sheath acceleration of positive charges, is less than 850 keV. On the other hand, the electrons in the laser propagation direction have peak energies extending above 2.25 MeV.

The result of this measurement can be presented more quantitatively in the polar plot shown in Figure 20. The electron number is integrated over the elevation plane and plotted as a function of the angle. The described heterogeneous distribution indicates the presence of multiple processes through which energy couples from the incident laser pulse to electrons. In addition, such processes can lead to spatiotemporal dynamics of

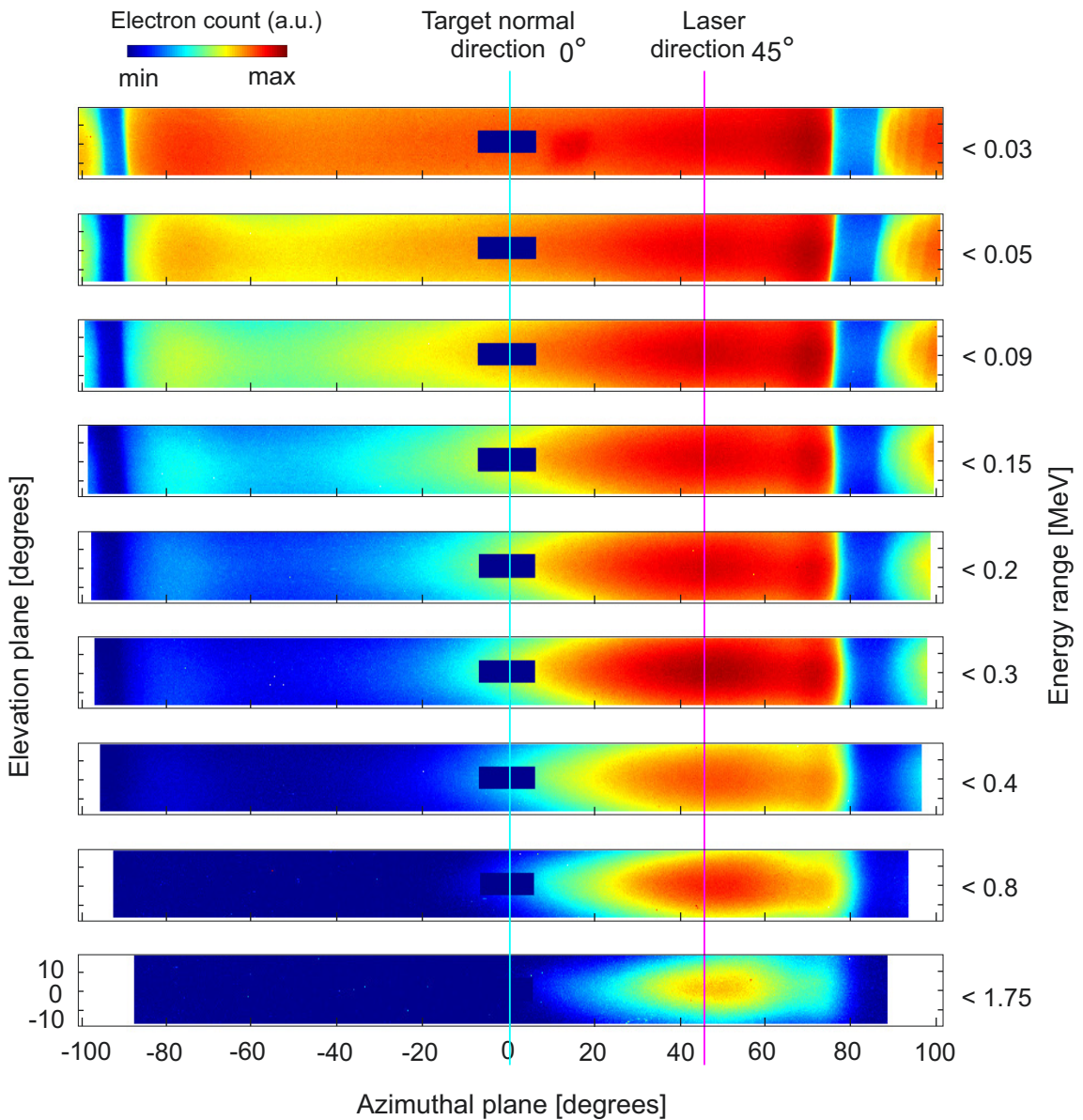


Figure 19: Scans of the same films from Figure 18 are flattened and assigned angles and energy values. A prominent peak of energetic electrons can be seen along the laser propagation direction.

charged particles, which in turn can be a potential source of electromagnetic radiation at the rear of the target, as we will discuss in Chapter 5.

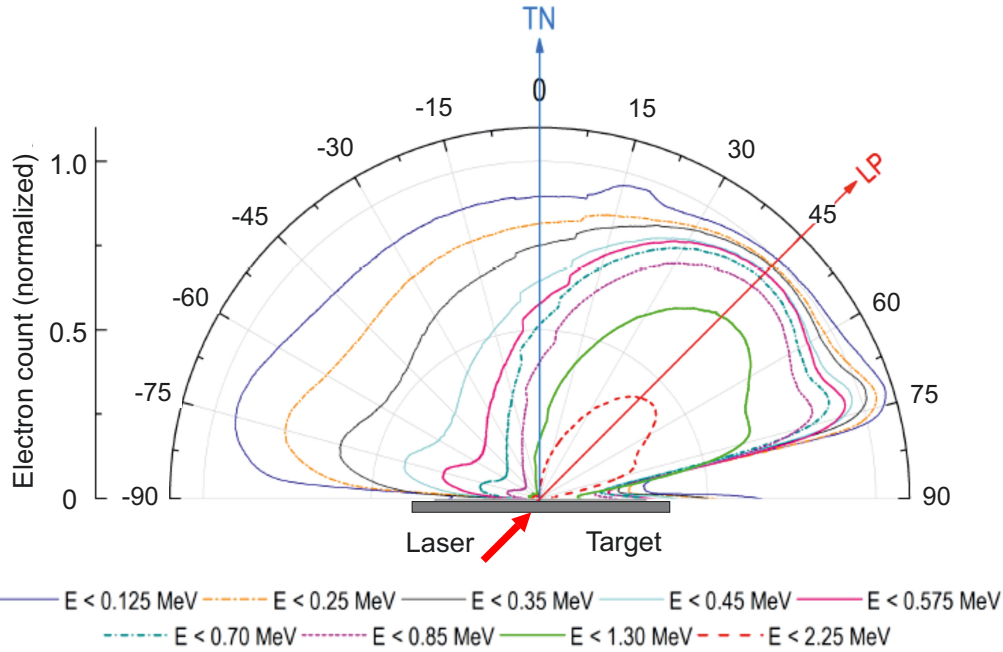


Figure 20: Energy-resolved angular distribution of hot electrons emitted at the back surface of the target during the interaction with intense laser pulses. A uniform distribution of low-energy electrons can be identified, as well as strong directional emission of high-energy electrons along the laser propagation direction LP. TN is the target normal.

4.2 Angular distribution of proton emission

Turning our attention to the proton emission, we reconstructed its angular distribution using CR-39 nuclear track detectors [87] arranged in a semi-circular configuration behind the target, covering the full range of angles in the interaction plane. We chose the CR-39 detector due to its user-friendly nature and its notable sensitivity to protons while being less responsive to electrons. For the measurement, we used the same interaction parameters, such as a maximum laser pulse energy of 1 J and a pulse duration of 32 fs. We used target foils of aluminum and separately of titanium, both with a thickness of $5\ \mu\text{m}$. Unlike the electron beam, the proton and ion beam in Figures 21 and 22 is only observable in the target's normal direction, with an opening half-angle of $23^\circ \pm 1^\circ$. This observation suggests that only the slower electrons ejected in the target normal direction contribute to the ion acceleration. As we will see later, the maximum proton energy measured with the ion spectrometer in the target normal direction exceeds 3.7 MeV.

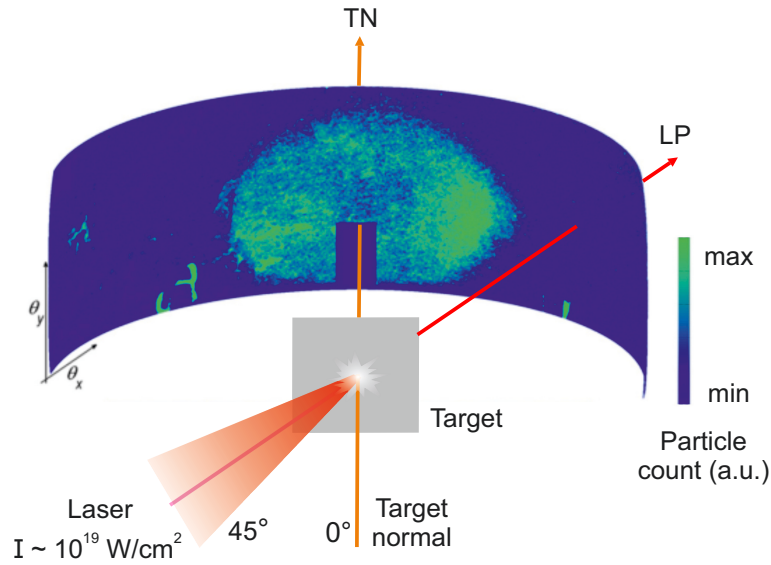


Figure 21: A scan of a CR39 plastic detector placed behind the target to record the angular distribution of accelerated protons and ions during the interaction.

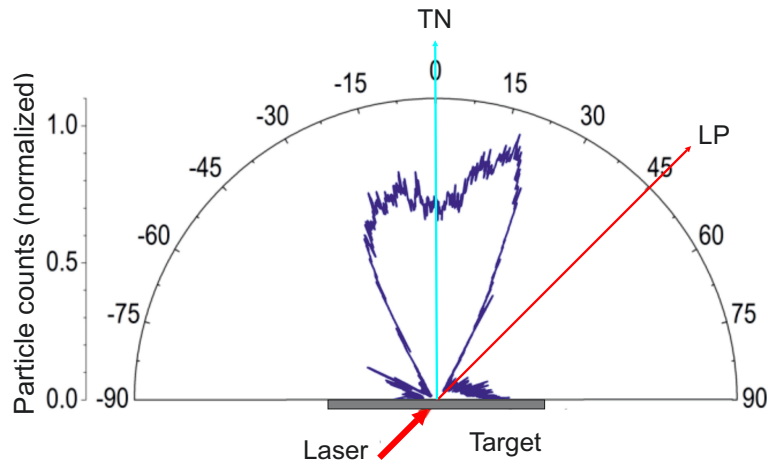


Figure 22: Angular distribution of the sheath accelerated protons and ions from Figure 21 emitted at the back surface of the target during the interaction with intense laser pulses.

4.3 Energy spectra of electrons and protons

By using dedicated energy spectrometers we provide more precise energy measurements of the emitted charged particles at the rear surface of the target during the interaction. Since experimental conditions can also vary between various laser systems around the world with similar characteristics, we wanted to test the dependence of the electron and proton emission on the parameters of our laser system. In the following, we present a full parametric study [88] supported by experimentally measured electron and ion

energy spectra while varying the experimental parameters such as laser polarization, intensity, pulse duration, and laser spot size on the target. We used calibrated electron spectrometers to record the electron energy at 0° and 45° , as well as, a Thomson parabola spectrometer to measure the ion energy at 0° . More on energy diagnostics can be found in the Appendix 8.

4.3.1 Electron temperature

In the following, we present the temperature of the electron emission behind the target in two distinct directions, the target normal (0°) and the laser propagation (45°) direction. We expect various electron temperatures along the aforementioned directions which can reveal the dominant electron heating mechanism at the front surface of the target during the interaction. In this experiment, we used aluminum foils with a thickness of $5\ \mu\text{m}$ as targets. The laser parameters were as follows: wavelength 800 nm, pulse energy 0.65 J, and pulse duration 32 fs. The laser polarization state (p- and s-) was controlled by a motorized 4-inch half-wave plate placed in the parallel region of the main beam before the focus.

The measured electron spectra are shown in Figure 23. All spectra are fitted by a Maxwell-like distribution $N(E_e) \sim \exp(-E_e/kT_h)$ with different linear fits for calculating electron temperatures kT_h (black lines). Starting from the electron spectra at the target normal direction shown on the left side, we find electron temperatures of 0.5 MeV and 0.3 MeV for the laser with p- and s-polarized states, respectively.

The higher electron temperature in the case of the p-polarized light is in good agreement with the theoretical scaling of resonance absorption [31]. During the interaction, a p-polarized laser pulse is incident at an angle ($\theta = 45^\circ$) on a pre-plasma with a gradient length of λ_g . Upon specular reflection, the electric field vector \vec{E} of the laser becomes parallel to the density gradient $\vec{\nabla}n$, thus, an electron plasma wave can be resonantly excited along the direction of the density gradient, and a fraction of the laser energy is transferred to the electrons. The temperature scaling in the case of resonant absorption follows $T_{\text{res}} = a(I\lambda^2)^{0.3}$ where a is an experimental constant. By substituting the values from the experiment we get an electron temperature of $T_{\text{res}} = 0.16(I = 50 \times 10^{18}[\text{W}/\text{cm}^2]\lambda^2 = 0.8^2[\mu\text{m}^2])^{0.3} = 0.5\ \text{MeV}$.

For s-polarization, we observe a Maxwellian-like distribution, albeit with a lower electron temperature of 0.3 MeV. This reduction can be attributed to the condition of the parallel electric field vector at the vacuum-plasma boundary, resulting in reduced energy coupling through resonance. However, resonant energy transfer can still occur

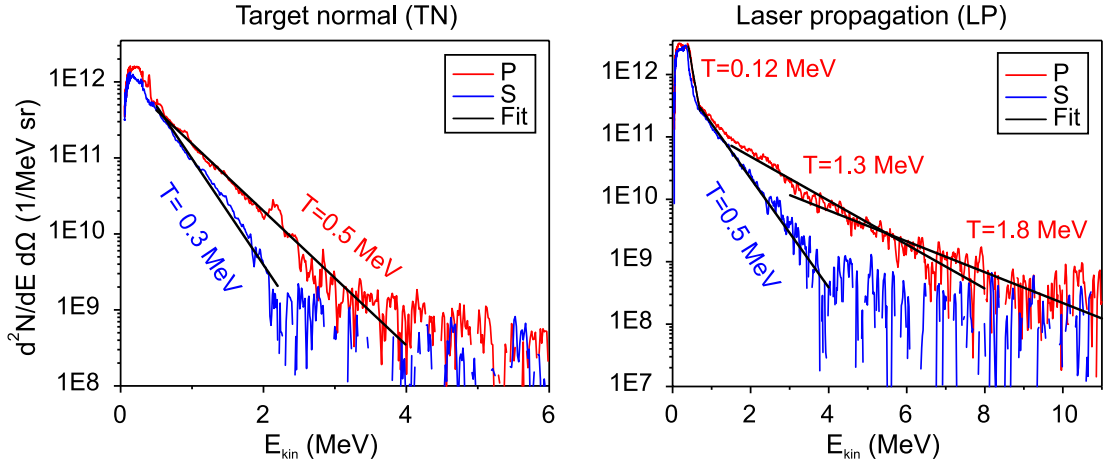


Figure 23: Recorded electron spectra with corresponding temperatures at the target normal direction 0° and laser propagation direction 45° for laser polarization states P and S. Black lines are linear fits.

at such high laser intensities due to the rippling of the critical surface and instabilities at the vacuum-plasma boundary, which can lead to additional regions where $\vec{E}\nabla n \neq 0$ [40]. If we lower the experimental value (a) and the scaling to compensate for the unfavorable conditions for resonance heating, we get $T_s = 0.12 [(I = 50 \times 10^{18} \text{ W/cm}^2) (\lambda^2 = 0.8^2 \mu\text{m}^2)]^{0.26} = 0.3 \text{ MeV}$. These values will be validated in the coming section.

Moving on to the energy spectra of the electron emission in the laser propagation direction (right graph in Figure 23). The electron temperature can be estimated by the ponderomotive potential of the laser pulse U_p with a scaling of $T_{\text{pond}} \propto (I\lambda^2)^{1/2}$ [45] and empirically as $T_{\text{pond}} = 0.511(\sqrt{1 + a_0^2} - 1) \text{ MeV}$ [89] with a_0 being the dimensionless laser parameter. With respect to the Jeti-40 laser parameters used here, we substitute

$$T_{\text{pond}} = m_0 c^2 \left(\sqrt{1 + \frac{(I_0 = 5 \times 10^{19} \text{ W/cm}^2) (\lambda^2 = 0.8^2 \mu\text{m}^2)}{1.6 \times 10^{18}}} - 1 \right) \quad (62)$$

and arrive at a temperature of $T_{\text{pond}} = 1.8 \text{ MeV}$. We measured a similar temperature near the high-energy tail of the electron spectrum as presented in 23.

However, the electron spectrum in the case of the s-polarized state has a lower temperature of 0.5 MeV . Such decrease in the temperature can be also seen in the simulations presented by Wilks in [31]. It is worth reminding that ponderomotive heating arises from the oscillating component of the ponderomotive force induced

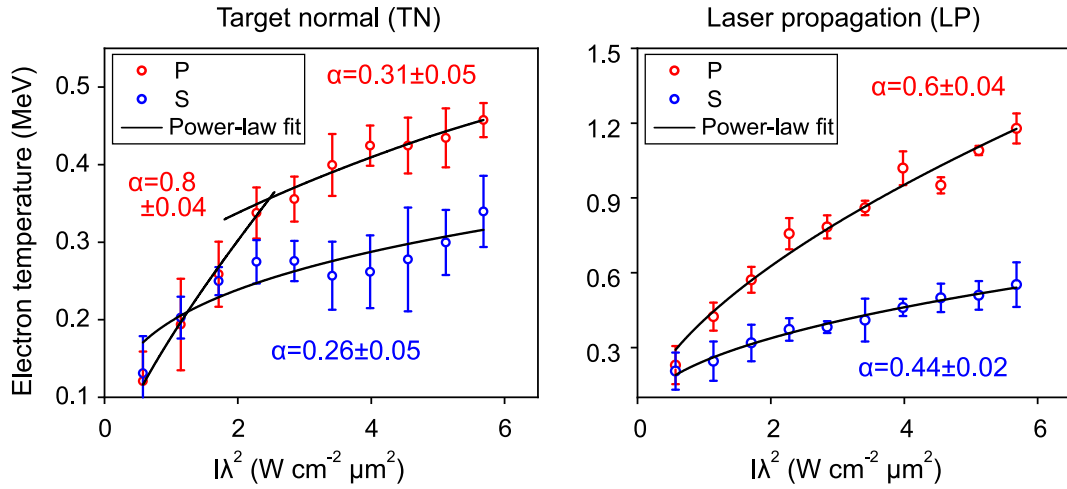


Figure 24: Electron temperatures as a function of the laser intensity show the scalings for vacuum and resonance heating at the target normal direction 0° and Pondermotive scaling at the laser propagation direction 45° . Black lines are power-law fits.

by the laser. When the magnitude of this force is sufficiently high, electrons at the vacuum-plasma interface will oscillate non-resonantly, aligning with the laser's vector direction. Nevertheless, the vector is the same for linearly p- and s-polarized light.

An additional feature in the electron spectra at the laser propagation direction is the clear multi-temperature distribution, see multiple line fits in the right panel of Figure 23. For example, on the low energy side ($E < 1 \text{ MeV}$), the electron temperature measures about 125 keV for both polarization states. For comparison, this feature is less apparent in the spectra measured at the target normal direction shown on the left in the same figure. It is possible that electron spectra integrated the emission with various temperatures due to multiple energy coupling mechanisms.

4.3.2 Laser Intensity Scan

We investigated the dependence of the electron and proton emission on the laser intensity for p- and s-polarized light. To control the laser intensity, we varied the pulse energy on the target from 10 mJ up to 650 mJ in steps $< 100 \text{ mJ}$, while keeping the pulse duration and the focal spot size fixed. We plotted the temperature against the equivalent laser intensity multiplied by the square of the wavelength $I\lambda^2$, and used a power-law fit $y = ax^\alpha$ to estimate the scaling that can be associated with the interaction mechanism.

Starting with the electron temperature recorded along the target's normal direction, as shown on the left in Figure 24. For p-polarized and moderate light intensities,

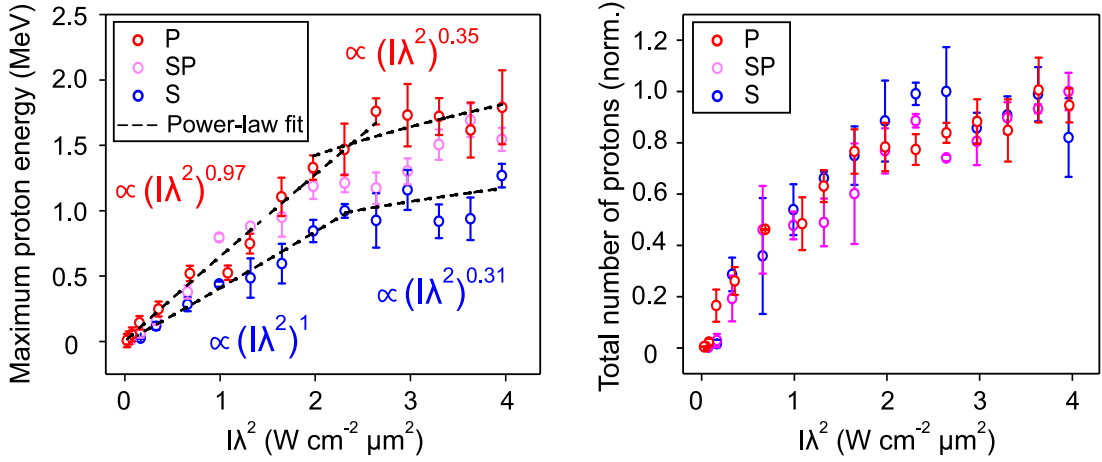


Figure 25: Maximum proton energy (left) and normalized proton numbers (right) as a function of laser intensity for p-, sp-, and s- laser polarization states. Dashed lines are power-law fittings.

the electron temperature increases rapidly with laser intensity, with a scaling of $\alpha = 0.8 \pm 0.04$ MeV up to around $\sim I = 2.1 \times 10^{19}$ W/cm². Such linear scaling indicates a significant contribution from vacuum heating and a sharp plasma density gradient at the plasma-vacuum boundary [41, 90]. At higher laser intensities, however, the scaling reduces to $\alpha = 0.31 \pm 0.05$ MeV and follows the scaling expected for resonant heating. The corresponding power-law fit is $T_{\text{res}} = 0.14(I\lambda^2)^{0.31}$, in good agreement with reference [31]. For the s-polarized light, the scaling is lower at $\alpha = 0.26 \pm 0.05$ MeV, which is due to the non-optimized conditions of vacuum and resonant heating. The fit, in this case, is $T_s = 0.12(I\lambda^2)^{0.26}$, which was used in the previous section to estimate the theoretical electron temperature against the experimental value we derived from figure 23.

For the recorded temperature of electrons propagating in the laser direction, shown on the right in figure 24, we see a clear pondermotive scaling, $\alpha = 0.5$ [45, 91]. The scaling follows $\alpha = 0.6 \pm 0.04$ MeV for the p-polarized light and is slightly lower for the s-polarized light at $\alpha = 0.44 \pm 0.02$ MeV.

During the laser-foil interaction, the dynamics of the charged particles at the rear surface of the target involve the acceleration of ions along the target normal direction. For laser intensities $\sim 1 \times 10^{19}$ W/cm², the TNSA mechanism is the dominant process. TNSA typically produces broad Maxwellian-like energy spectra with an exponentially decreasing profile with a sharp cutoff as the ion energy increases [92]. It has been found that the maximum energy of the accelerated protons is proportional to the temperature of the hot electrons, i.e. $E_{\text{proton}}^{\text{max}} \approx \beta T_{\text{hot}}$ [93]; The beta factor will be determined for

a variety of parameters.

To acquire the energy spectra for the accelerated ions, we employed a Thomson-parabola spectrometer as illustrated in figure 44. We are mainly interested in the proton signal since they have the highest charge-to-mass ratio of all TNSA accelerated ions. In figure 25 we present the maximum energy and total number of protons as a function of laser intensity for the p, s, and (45°) sp-polarized states. On the left, we see the recorded maximum proton energy as it increases with laser intensity. Similar to the increase in electron energy reported previously in figure 24, the maximum proton energy follows a power law of $\alpha \approx 1$ for intensities up to $2.1 \times 10^{19} \text{ W/cm}^2$. At higher intensities, the power-law scaling decreases to $\alpha_p \approx 0.35$ and $\alpha_s \approx 0.31$ for p- and s-polarized light, respectively. In addition, the increase in the maximum proton energy when using sp-polarized light lies in between the reported scaling values, since the sp-polarization state can be considered as a superposition of p- and s-states.

Given the maximum proton energies of $E_p^{\text{max}} \sim 2 \text{ MeV}$ and $E_s^{\text{max}} \sim 1.5 \text{ MeV}$, and the electron temperatures of $T_p = 0.5 \text{ MeV}$ and $T_s = 0.3 \text{ MeV}$, we estimate the beta factors to be $\beta_p \approx 4$ and $\beta_s \approx 5$ for p- and s-polarized light, respectively. This comes in good agreement with the work in reference [94].

In the right panel of Figure 25, we present the recorded total number of emitted protons entering the spectrometer for the three polarization states. We integrated the total number of protons collected by the Thomson-parabola from the lowest detectable energy of 30 keV up to the maximum proton energy recorded. Each spectrum is then normalized to its maximum. We could not observe a significant difference in the relative growth of the proton number due to the polarization of the incident light.

It is worth mentioning that when acquiring the electron spectra, the electron spectrometer was inserted in the beam path of the ion spectrometer, thus blocking the latter. As a result, the ion and electron spectra were not taken simultaneously, but consecutively under comparable conditions.

4.3.3 Laser Pulse Duration Scan

Next, we fix the laser energy on target at the maximum value of 0.65 mJ and vary the temporal duration of the laser pulse and measure the corresponding energy of the charged particles. The scan range started from the optimized minimum pulse duration of 32 fs up to 180 fs. In the case of energy resolved measurements of electrons, the duration range is shorter, from 32 fs up to 100 fs. We employed an acousto-optic programmable dispersive filter (Dazzler device) to vary the group delay dispersion [95]

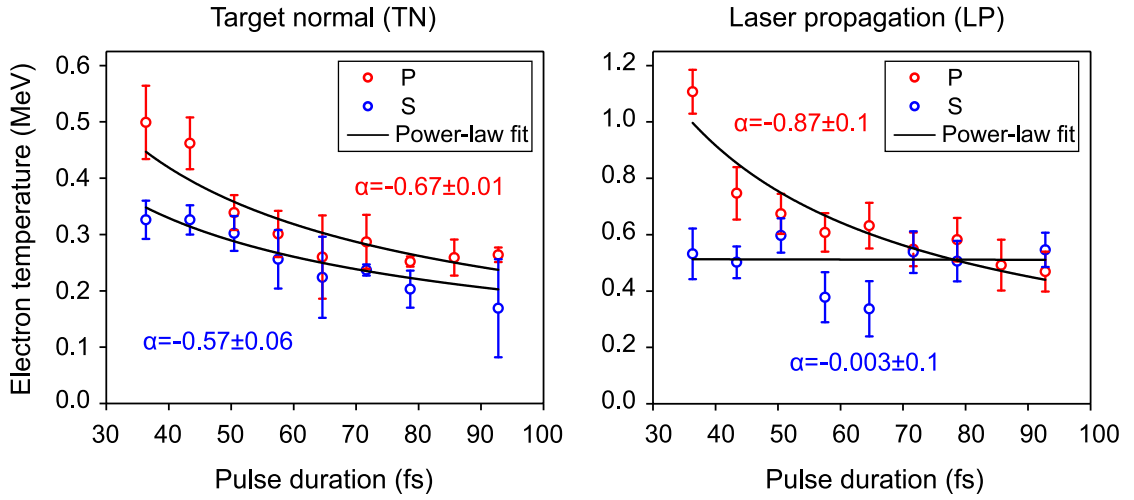


Figure 26: Electron temperature as a function of laser pulse duration recorded at target normal (0°) and in laser propagation direction (45°) for p- and s- laser polarization states.

and Spider and Wizzler devices [96] to measure the pulse duration for different Dazzler parameters.

In Figure 26 we present the measured electron temperature as the duration of the laser pulse increases. A general downward trend is seen for both p- and s-polarized light when extending the pulse duration from 32 fs to 93 fs at 0° and 45° . We found that the decrease in electron temperature can be presented with a scaling power of -0.67 ± 0.01 MeV for p- and -0.57 ± 0.06 MeV for s-polarized light in the normal direction (0°), and -0.87 ± 0.1 MeV for p-polarized light for electrons at 45° . Interestingly, the electron temperature for s-polarization at 45° does not show a significant dependence on the pulse duration.

Moving on to the recorded maximum proton energy presented in Figure 27, the resolution is higher compared to the electron scan as we recorded more data over a longer duration span. We can see a slight energy increase followed by a general downward trend with increasing pulse duration. This behavior agrees with the work in [97]. It is worth mentioning that the intensity is not kept constant when varying the pulse duration, but only the energy, which is set to a maximum value on target. The intensity is shown on the upper axis. In the case of p-polarization, and less clearly in s-polarization, the highest proton energy was reached for around 70 fs. After this peak, the energy decreases with the laser pulse duration with a scaling law of 0.5 for both polarization states. This is in agreement with the analytical model of a radially confined surface charge induced by laser-accelerated electrons on the target rear surface [98]. To

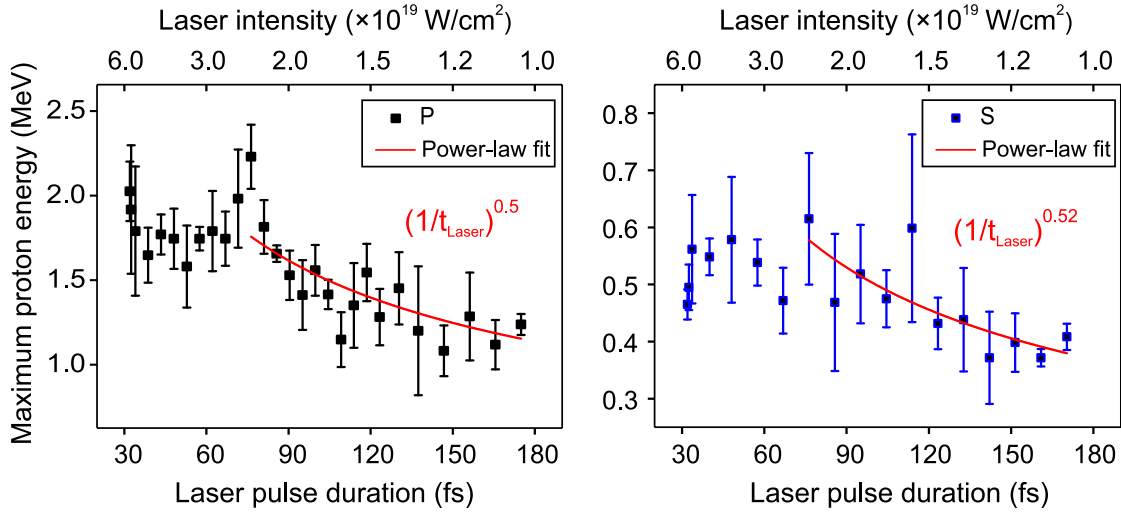


Figure 27: Proton maximum energy as a function of laser pulse duration for (left) p-, and (right) s-polarized laser. The red (solid) line is a power-law fitting.

establish the scaling for the reduction in maximum proton energy with increasing laser pulse duration, we consider that the laser energy (E_L) is converted with an efficiency of η into hot-electron energy over the time of the pulse duration (τ_L). The maximum possible energy an ion could gain for a certain laser power $P_L = E_L/\tau_L$ is [98]

$$E_{\text{proton}} = \alpha 2m_e c^2 \left(\eta \frac{E_L}{\tau_L P_R} \right)^{1/2} \quad (63)$$

where $P_R = mc^3/r_e = 8.7 \text{ GW}$ is the relativistic power unit, r_e is the classical electron radius, and $\eta = 0.4$ [99, 100] is the conversion efficiency of energy transfer from the laser into hot-electron. We used a factor of $\alpha = 0.11$ to obtain the same maximum proton energy of $E_{\text{proton}} = 2.3 \text{ MeV}$ as seen in the left panel of Figure 27 at a pulse duration of $\tau_L = 70 \text{ fs}$. After substitutions, Eq.63 becomes equivalent to

$$E_{\text{proton}} = 9.8 \times 10^{-20} [\text{J}] \left(\frac{1}{\tau_L [\text{s}]} \right)^{1/2} \quad (64)$$

We used a quantity of $9.8 \times 10^{-20} [\text{J}]$ in Equation 64 to fit the data for the maximum proton energy after the peak at $\tau_L = 70 \text{ fs}$ and indeed we obtain a scaling of $(1/\tau_L)^{0.5}$.

On the other hand, when plotting the proton yield as a function of the laser pulse duration, as seen in Figure 28, we find an uptrend for both polarization states. The energies of the summed protons start at the low energy threshold of 30 keV of the spectrometer and go up to the maximum reported in Figure 27. We compare our experimental findings with the theoretical estimation of the total number of protons

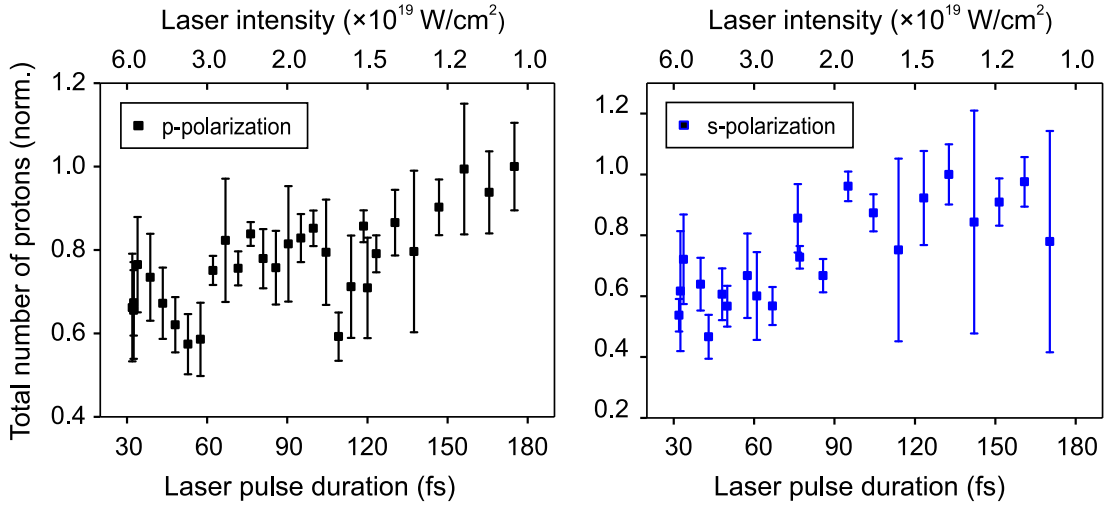


Figure 28: Total number of protons recorded along the target normal direction (0°) as a function of laser pulse duration for p- (left) and s-polarized light (right).

given by the fluid model of Mora [51], and after some work we obtain

$$N_p = n_e c_s t_{\text{acc}} S_{\text{sheath}} \exp\left(-\sqrt{\frac{2E}{T_{\text{hot}}}}\right) \Big|_{E_{\text{max}}}^{E_{\text{min}}} \quad (65)$$

where N_p is the total number of accelerated protons over a given energy range, n_e is the electron density, c_s is the sound speed, $t_{\text{acc}} = 1.3\tau_L$ is the acceleration time [93], and S_{sheath} is the sheath size at the target rear surface. We can observe that the number of accelerated protons can increase with the pulse duration, even though the maximum energy available per particle is lower due to the finite energy distribution over a longer time span. Finally, it is crucial to limit an effective 'acceleration time' (t_{acc}); otherwise, the fluid model in [51] would predict endless proton acceleration due to the isothermal hypothesis, which assumes no energy depletion of the electrons.

4.3.4 Laser focus Spot Size

At this point, we fix both the laser energy and pulse duration, while varying the laser spot size on the target by moving the target along the focus, and as a result, the intensity of the laser varies with the spot size w_z . To properly estimate the intensity, we measured the spot size of the laser beam around the focus at lower energies under vacuum using a motorized objective and a CCD camera. Figure 29 (left) shows the measured spot size at $1/e^2$ of the maximum value at each z position fitted using a Gaussian equation to estimate the laser spot size further along the propagation axis as

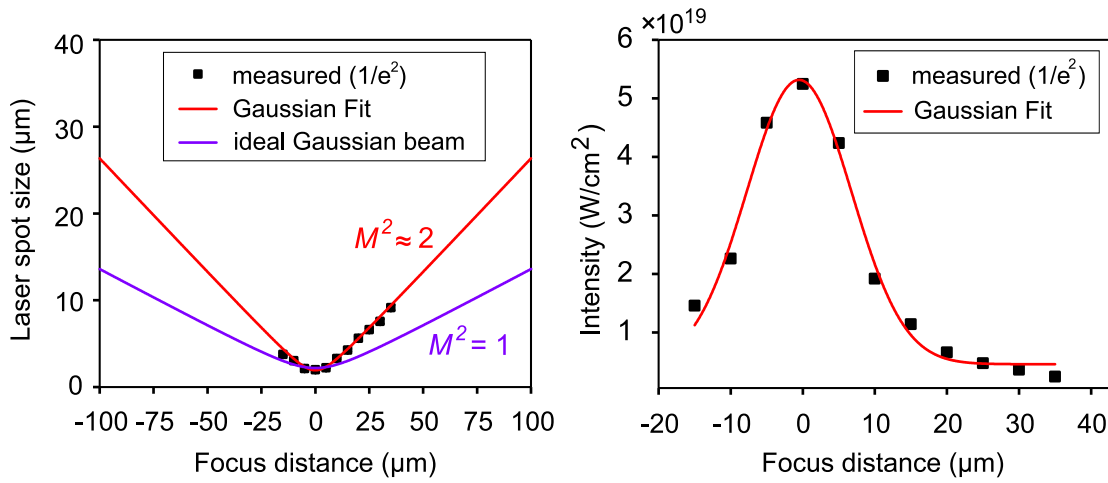


Figure 29: (Left) measured laser spot size along the focal axis z . Red line is a fit of a Gaussian beam. The magenta line shows an ideal Gaussian beam with a beam quality factor of $M^2 = 1$. (Right) the corresponding intensity fitted with a Gaussian profile.

$$w(z) = w_0 \sqrt{1 + \left(\frac{z}{w_R}\right)^2} \quad (66)$$

where the spot waist at $z = 0$ is $w_0 = 1.93 \pm 0.05 \mu\text{m}$ and the experimental Rayleigh range is $w_R = 7.37 \pm 0.3 \mu\text{m}$. This gives a beam quality factor of $M^2 = \pi w_0^2 / w_R \lambda \approx 2$, to be compared to an ideal Gaussian beam with $M^2 = 1$. We also estimated the equivalent intensities on target as shown in the right panel of Figure 29 with Gaussian beam fitting.

Going back to characterizing the proton emission, we measured the maximum proton energy at each target position, see Figure 30. As previously presented, we achieve the highest proton energy when using p-polarized light and the lowest energy when using s-polarized light. Furthermore, for all polarization states, the proton gains its maximum energy at the focal point corresponding to the highest intensity and beyond the Rayleigh range of the focused laser, the energy decays rapidly.

When estimating the proton yield recorded at each focal position as presented in Figure 31, we see a double-peak structure with the minimum at the zero position of the focus. This feature is evident for both polarization states (p and s) and can be accounted for by the volumetric effect. Although the laser intensity decreases fast away from the focus, the irradiated area on the target becomes larger, meaning that more particles are involved at a given volume. However, this is only applicable if the intensity is still sufficient to generate hot electrons that propagate through the target

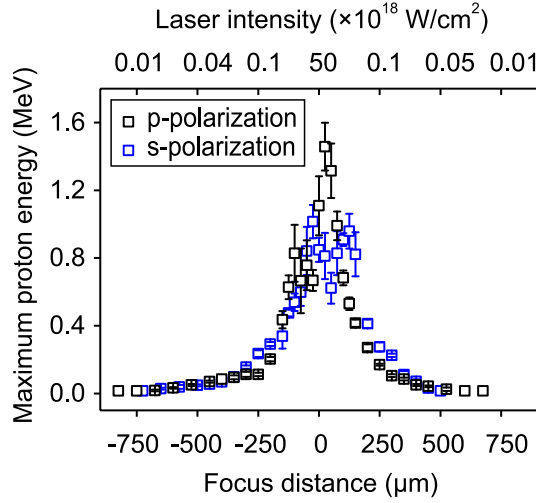


Figure 30: Maximum proton energy as a function of the target position along the laser focus when employing p- and s-polarized light.

and accelerate the protons at the rear surface. To test that, we employed a Gaussian fit to the measured proton yield and found that the average position of the peak in the case of p-polarization is around $\pm 155 \mu\text{m}$ and slightly larger for the s-polarization state of around $\pm 220 \mu\text{m}$. Next, we calculate the equivalent intensity at these positions using the fitted Gaussian beam profile shown in equation 66. This gives an intensity just below 10^{18} W/cm^2 . At such an intensity, the electron temperature can be derived from the left panel in Figure 24 where it is experimentally measured as $T_{\text{hot}} \approx 0.1 \text{ MeV}$. These hot electrons must still be involved in creating a strong enough sheath field to ionize and accelerate the protons at the rear surface of the target. We use a simple equation to estimate the electric field of the sheath at the exit behind the target as [89]

$$E_{\text{TNSA}} = \frac{\sqrt{2} k_B T_e}{e \lambda_D} \quad (67)$$

where λ_D is Debye length. The (TNSA) electric field when the target is at the position where the maximum number of protons is detected is roughly $1 \times 10^{11} \text{ V/m}$, which is about one order of magnitude lower than its value at the focus $z = 0$, yet it is still strong enough to ionize hydrogen atoms at the target side via barrier suppression of the atoms Coulomb field BSI [101] with a threshold electric field strength of

$$E_{\text{ion}} = \frac{\pi \epsilon_0 (U_{\text{bind}}^2 = 13.6 \text{ eV})}{e^3 (Z = 1)} \approx 10^{10} \text{ V/m} \quad (68)$$

In the case of s-polarization, we estimate an electron temperature of around $T_{\text{hot}} \approx$

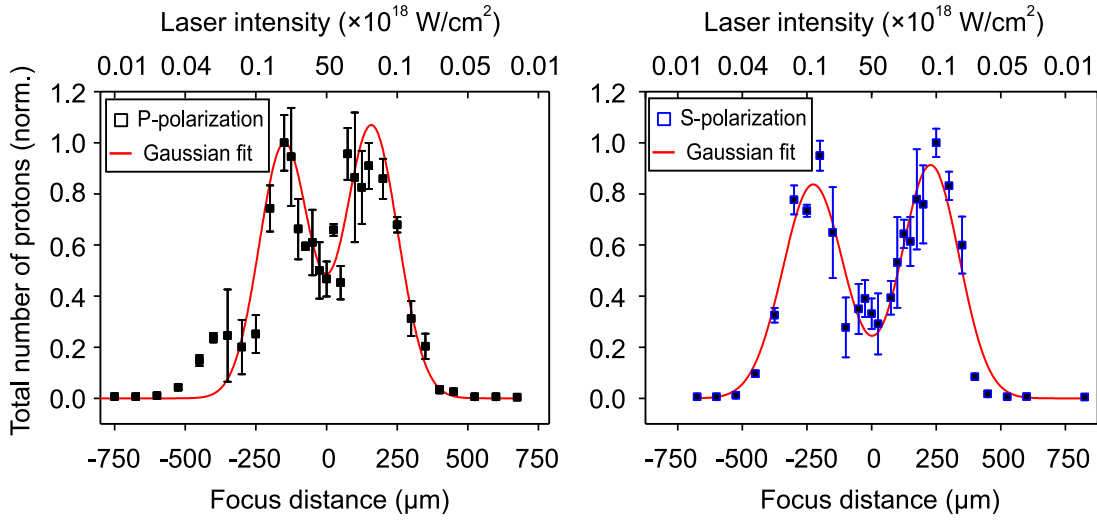


Figure 31: Total number of protons as a function of the target position along the laser focus for a laser polarization state of p- (left) and s-(right). The red (solid) line is a Gaussian peak fit.

40 keV, which corresponds to a sheath field of $E_{\text{TNSA}} = 3 \times 10^{10}$ V/m compared to $\sim 7 \times 10^{11}$ V/m at the focus position.

To elaborate more on the volumetric volume effect responsible for the two-peak feature seen in the proton yields, we calculate the TNSA electric field and the interaction volume at different target positions. We start with the TNSA field, which, as discussed before, depends on the electron temperature T_{hot} and the Debye length $\lambda_D = \sqrt{\epsilon_0 k_B T_e / e^2 n_e}$, where n_e is the electron density at the target rear surface neglecting recirculation [89]. To estimate the electron temperature behind the target, we first calculate it at the target front surface at different target positions (which correspond to different laser intensities), using the power scaling from the intensity scan from Figure 24, $T_{\text{hot}} \propto (I\lambda^2)^{0.8-0.31}$. These electrons are then injected into the target where their energy decreases mainly due to collisional energy transfer to bound atomic electrons following ‘‘Bethe’’ theory [102]. The TNSA field is then calculated for each target position. As expected, the TNSA electric field decreases as the electron temperature decreases rapidly from the focus position, see the left panel in Figure 32. We also added a field ionization threshold limit of $\sim 10^{10}$ V/m for ionizing hydrogen atoms behind the target.

The counteracting factor in our model is the increasing interaction volume of the incident laser pulse and the plasma created on the irradiated side of the target. We consider an interaction volume of $V_{\text{inter}} = (\pi w_z^2)(t_{\text{pre}} c_s)$ as shown in the right panel in

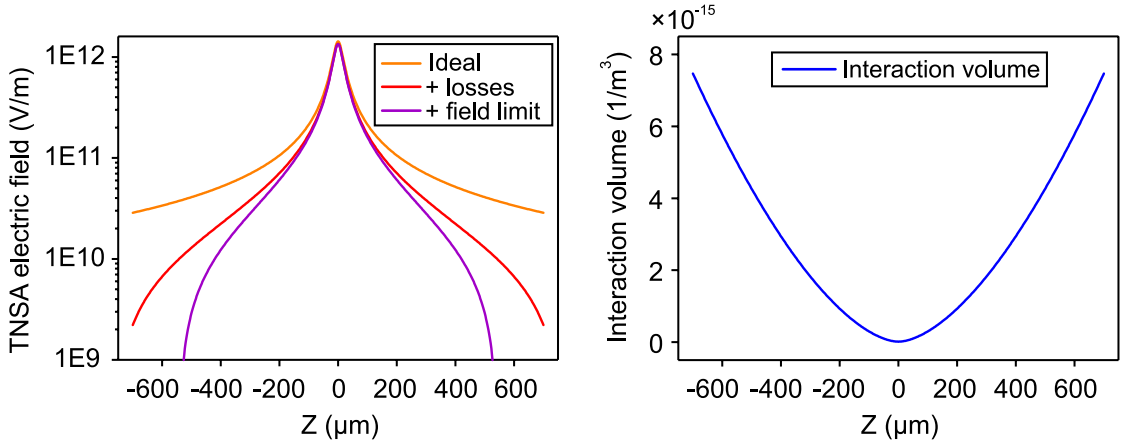


Figure 32: Theoretical calculations for TNSA electric field at the target rear surface at various conditions as a function of the target position (left), and the interaction volume at the target front side (right).

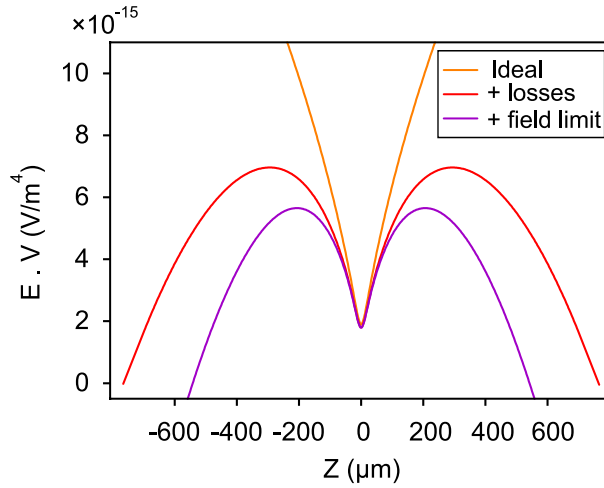


Figure 33: The product of the modified TNSA electric field and the interaction volume as a function of the target position along the laser focus. The product reveals a double-peak feature similar to the experimentally measured proton yield in Figure 31 regardless of the laser polarization.

Figure 32, where πw_z^2 is the focus spot size at the target position, $t_{\text{pre}} = 10$ ps is the time between the main laser peak and the pre-pulse from the contrast scan, and c_s is the pre-plasma expansion velocity. The product of $(E_{\text{TNSA}} \cdot V_{\text{inter}})$ displayed in Figure 33 shows matching behavior to the measured proton yield, particularly when using the ionization limit of $E_{\text{ion}} = 10^{10}$ V/m. It is worth mentioning that this simple model neglects some aspects that are crucial for the laser-plasma interaction, such as the changing pre-plasma dynamics for different laser intensities and the interplay between

various absorption mechanisms at different polarization states. To adequately address this task, however, extensive simulations are required.

4.4 conclusion

In this chapter, we have presented a complete parametric characterization of the emission of charged particles from the rear side of the target during the interaction with intense laser pulses. Such work serves as a valuable addition to the field of laser-particle acceleration. In addition, having a fully quantified characterization of the charged particles enables the construction of a fitting numerical model, which will be presented in the next chapter, to reveal the dominant physical processes that can lead to the previously detected emission of sub-picosecond radiation.

In summary, we have recorded the angular distribution of the hot electrons exiting the target, revealing the presence of two distinct electron heating mechanisms: resonant absorption and ponderomotive heating. We have also delivered precise energy-resolved measurements of the electron emission along two distinct directions: the target normal and the laser propagation direction, all while varying the laser parameters. We have measured the temperature of accelerated electrons, demonstrating the heating mechanism responsible for the energy transfer during the interaction.

As for characterizing the emission of accelerated protons during the interaction, we have experimentally investigated the effect of different laser parameters on the number and maximum energy of protons. The total number of protons increased with laser intensity for all polarization states of the incident laser, with a slight saturation above $3 \times 10^{19} \text{ W/cm}^2$. A similar trend was also observed in the case of maximum proton energy. The measured scaling of the maximum proton energy with the electron temperature is around $E_p \approx 4-5 T_e$, in agreement with theoretical work [103]. Further, we observed a slight increase in the maximum proton energy when increasing the laser pulse duration from 32 fs up to 70 fs, however, the maximum energy decreased when increasing the laser pulse duration for all polarization states. For p- and s-polarization states, we obtained a scaling of $E_p^{\text{max}} \sim \left(\frac{1}{\tau_{\text{Laser}}}\right)^{0.5}$. Finally, we also varied the laser spot size on the target and observed a double peak structure in the number of protons for both polarization states, which was accounted for by the volumetric effect.

In short, we have quantified the energetic and directional emission of charged particles that could be primarily responsible for the generation of the detected EM radiation, as we will see next.

5 Theory of THz generation processes

So far we have measured sub-picosecond radiation pulses in the THz spectral range, where we detected three strong pulses with field strengths up to MV/m. We have also delivered complete measurements and characterization of the accelerated charged particles including electrons and protons. All of the above is emitted during the interaction of a high-intensity laser pulses with thin targets. While we expect that such strong radiation is induced by the transient dynamics of the accelerated charged particles, we still need to quantify this relation.

In this chapter, we present a detailed numerical investigation of the dominant physical processes leading to the emission of THz radiation based on experimentally measured electron and ion spectra at the rear surface of the target. We compare the results of the numerical modeling with the experimental observations of the radiation presented in Chapter 3. Additionally, we also estimate the longitudinal bunch duration of the particle bunch exiting the target rear surface and the source size of the plasma sheath generating the THz radiation.

5.1 Coherent transition radiation

Transition radiation (TR) is emitted when an electron passes through an interface that separates two media with different dielectric constants (relative permittivity) ϵ_r [104, 105]. This can be treated using classical electrodynamics. By using the macroscopic form of Maxwell's equations the problem reduces to

$$\nabla \times \mathbf{H} = \frac{\partial \mathbf{D}}{\partial t} + ev\delta(r - vt), \quad (69)$$

$$\nabla \times \mathbf{E} = -\frac{\partial \mathbf{B}}{\partial t}, \quad (70)$$

$$\nabla \cdot \mathbf{B} = 0, \quad (71)$$

$$\nabla \cdot \mathbf{D} = e\delta(r - vt), \quad (72)$$

where \mathbf{H} , \mathbf{E} , \mathbf{D} , \mathbf{B} are the magnetic field, electric field, displacement density, and the magnetic flux density, respectively. Additionally, δ denotes the Dirac distribution and $r = vt$ defines the trajectory of the electron. In the case of laser-accelerated electrons in a semi-infinite plasma, as considered in [106, 107], the full solution of this system of equations is the sum of the solution of the homogeneous and inhomogeneous problems.

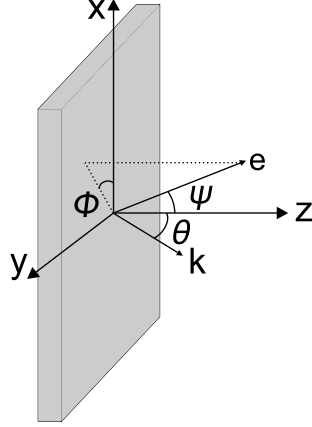


Figure 34: Geometric parameters considered in the TR calculations are as follows: e represents the particle's direction, k denotes the wave (observation) vector, and z is the target normal.

The field associated with the charged particle in the inhomogeneous solution does not 'see' the presence of an interface [84]. In contrast, the homogenous solution ensures the continuity of the tangential components of E and H and of the normal components of D and B . However, the boundary conditions can not be fulfilled by the particle's field alone, and, as a result, requires the presence of a unique solution to the problem which is the emission of a radiation field (TR).

In the case of laser-plasma interaction, where the hot electrons propagate across the boundary between a plasma with dielectric constant $\epsilon_r \rightarrow \infty$ and a vacuum $\epsilon_r = 1$, the angular and spectral distribution of the energy of the TR emitted by a single electron reads [84]

$$\frac{d^2\epsilon_e}{d\omega d\Omega} = \frac{d^2\epsilon_e^{\parallel}}{d\omega d\Omega} + \frac{d^2\epsilon_e^{\perp}}{d\omega d\Omega} \quad (73)$$

where indexes \parallel and \perp designate the parallel and perpendicular components of the TR electric field with respect to the radiation plane. The two orthogonal polarization components are given by

$$\frac{d^2\epsilon_e^{\parallel}}{d\omega d\Omega} = \frac{e^2 \beta^2 \cos^2\psi}{4\pi^3\epsilon_0 c} \left[\frac{\sin\theta - \beta \sin\psi \cos\phi}{(1 - \beta \sin\theta \sin\psi \cos\phi)^2 - \beta^2 \cos^2\theta \cos^2\psi} \right]^2, \quad (74)$$

$$\frac{d^2\epsilon_e^{\perp}}{d\omega d\Omega} = \frac{e^2 \beta^2 \cos^2\psi}{4\pi^3\epsilon_0 c} \left[\frac{\beta \cos\theta \sin\psi \sin\phi}{(1 - \beta \sin\theta \sin\psi \cos\phi)^2 - \beta^2 \cos^2\theta \cos^2\psi} \right]^2, \quad (75)$$

where e and β describe the charge and the reduced velocity of the electron, c is the

light velocity in vacuum, and ψ is the electron incidence angle at the boundary, i.e. 0° (target normal) and 45° (laser direction) in our experiments. θ is the angle between the direction of the emitted radiation and the observer, while ϕ defines the azimuthal angle defined in the boundary plane (XY).

In the previous chapter, we presented the energy spectra of the accelerated electrons during the laser-solid target interaction. A large number of electrons are accelerated and transported to the rear side of the target. As a result, the total energy of the emitted TR is the superposition of the radiated fields from a beam of N_e individual electrons crossing the plasma-vacuum boundary with a longitudinal bunch length σ_z . For emitted wavelengths much shorter than σ_z , the radiation field from each electron adds up incoherently and scales only with N_e . For wavelengths, λ_{TR} longer than σ_z , however, the TR emitted by individual electrons adds up coherently and scales with $\sim N_e^2$. Considering the recorded electron spectra presented in this work, which show a sufficiently large number of hot electrons of $\sim 10^{10}$ electrons/pulse, we can neglect the part of incoherent transition radiation. The angular and spectral distribution of the coherent component of the radiation (CTR) by an electron bunch with N_e electrons can be estimated as [106]

$$\frac{d^2 \varepsilon_{\text{CTR}}}{d\omega d\Omega} \approx \frac{e^2 N_e^2}{4\pi^3 \epsilon_0 c} \left(\left| \int d^3 p g(p) \xi^{\parallel} F(\omega) D(\omega, \rho) \right|^2 + \left| \int d^3 p g(p) \xi^{\perp} F(\omega) D(\omega, \rho) \right|^2 \right) \quad (76)$$

here p is the electron momentum and $g(p)$ is the electron bunch momentum distribution. ξ^{\parallel} and ξ^{\perp} denote the electric field amplitudes in the plane parallel and perpendicular to the radiation plane, respectively. $D(\omega, \rho)$ represents the diffraction function that includes the diffraction effects on the CTR spectrum emerging from the finite transverse size ρ of the boundary [106], whereas $F(\omega)$ is the bunch form factor (the coherence function) which is the Fourier transform (FT) of the normalized electron bunch distribution. The spatial form in the factor F can be written for a near-divergenceless beam at the plasma vacuum boundary ($\psi \ll 1$) as $F \approx \exp[-(\omega\sigma_z/\nu)^2/2]$.

In the following, we estimate the temporally integrated angular and spectral distribution of the CTR for hot electron bunches exiting the rear surface of the target along the 0° (target normal) and the laser propagation direction at 45° . From the energy spectra presented in the previous chapter in Figure 23, both electron emissions have Boltzmann-like energy distributions. In addition, we consider the broadening of the bunch due to energy dispersion while propagating through the target. We assume that

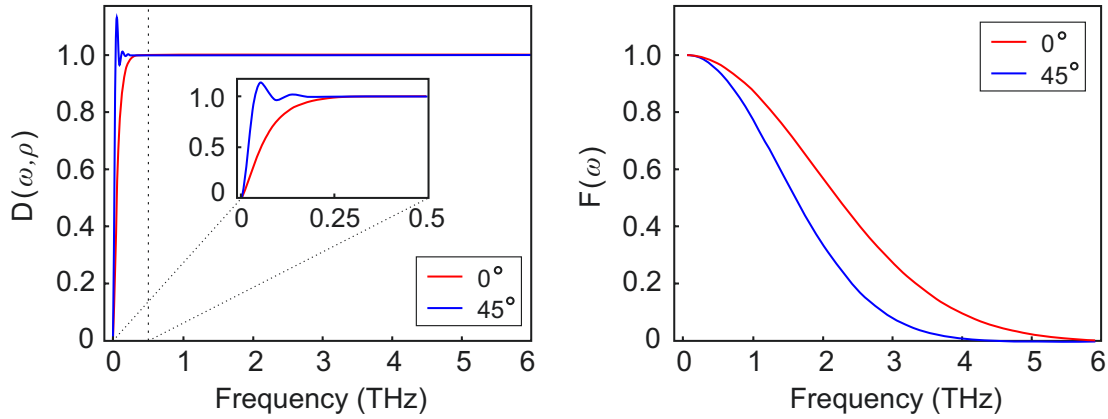


Figure 35: Left: the diffraction function $D(\omega, \rho)$, calculated for a transverse boundary of radius $\rho = 5$ mm, and right: the coherence function (form factor) $F(\omega)$, calculated for electron bunches exiting the target in the 0° and 45° directions. The dynamics of the electron bunches at the plasma-vacuum boundary with longitudinal lengths around 120 fs and 166 fs define the spectrum of the CTR emission to be in the THz spectral range.

an electron bunch is accelerated by a laser pulse on the front side of the target with an initial bunch length of $\sigma_z = \tau_L \cdot c \approx 9 \mu\text{m}$ for a laser pulse duration of $\tau_L = 30$ fs. The estimated bunch lengths at the rear surface of the target due to broadening are $\sigma_{z,0^\circ} = 36 \mu\text{m}$ and $\sigma_{z,45^\circ} = 50 \mu\text{m}$.

Figure 35 shows the calculated bunch form factor $F(\omega)$, and the diffraction function $D(\omega, \rho)$, for a boundary of the transverse size of a $\rho = 5$ mm radius. We also assume the bunch length previously presented, which is equivalent to a temporal dimension of $\sigma_{z,0^\circ} = 120$ fs and $\sigma_{z,45^\circ} = 166$ fs. Consequently, the frequency range of the emitted CTR lies in the THz spectral range. We can see that the radiation is sufficiently coherent for wavelengths $\lambda = 2\pi c/\omega$ that are large compared to the dimension of the bunch $\lambda \gg \sigma_z$. On the other hand, for radiation wavelengths such as $\lambda \ll \sigma_z$, the spatial form factor vanishes $F \simeq 0$ and the beam does not radiate coherently $\varepsilon_{\text{CTR}} \simeq 0$.

Next, we calculate the angular distribution of the CTR with parallel (\parallel) and perpendicular (\perp) electric field components to the radiation plane as the electrons exit the target in the 0° and 45° directions, see Figure 36. The theoretical expressions for ε^\parallel and ε^\perp can be found in [84, 105]. We find that the CTR radiated due to the exiting electrons in the 0° direction is purely radially polarized, as there is no perpendicular polarization component of the electric field. On the contrary, the CTR emitted by the electron at 45° has both orthogonal components, albeit with distinct magnitudes, as

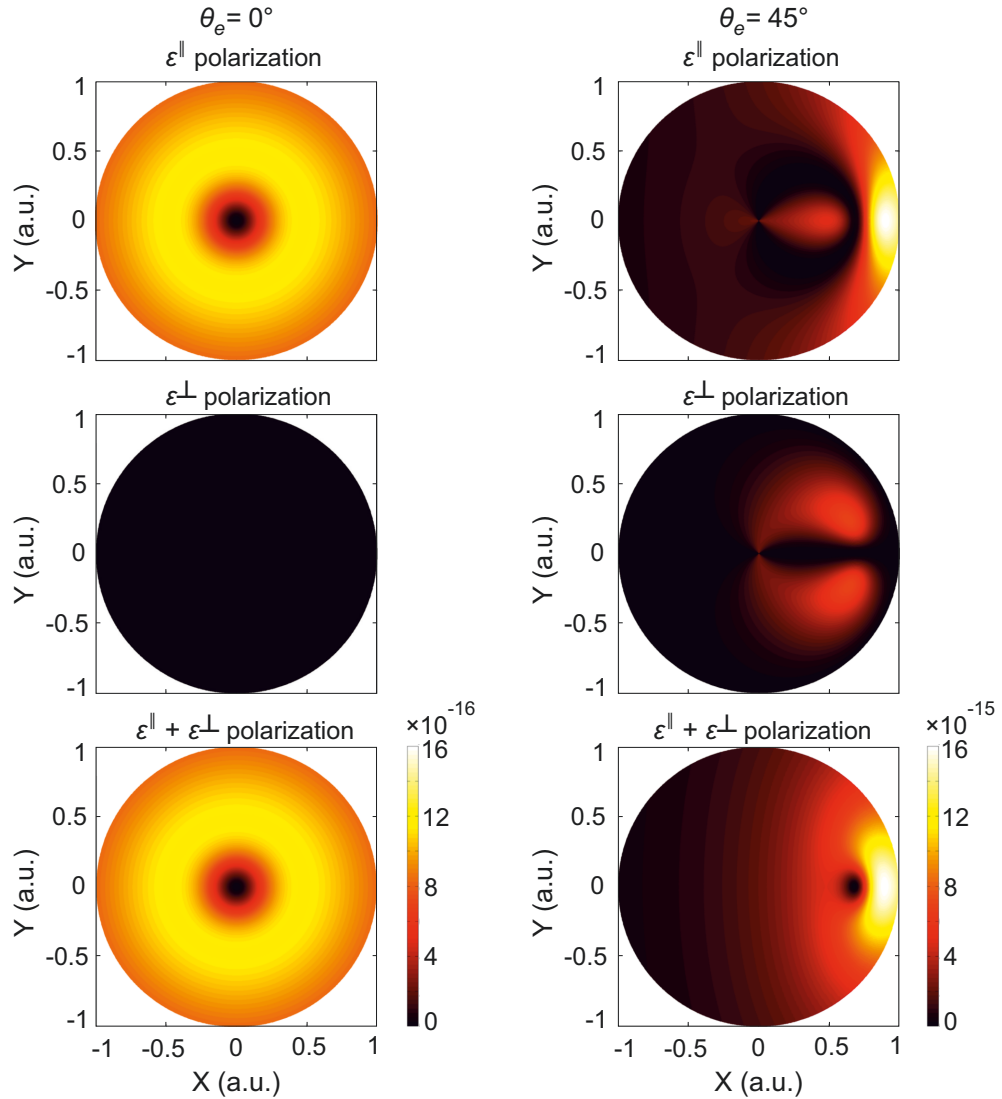


Figure 36: Spectrally integrated angular distributions of energy radiated in the form of coherent transition radiation (CTR) in the XY plane when electrons exit the target at 0° (left column) and 45° (right column). The top panels show the parallel component ε^{\parallel} , the middle, the perpendicular component ε^{\perp} , and the bottom, the sum of the two polarization components $\varepsilon^{\parallel} + \varepsilon^{\perp}$ of the electric field.

the energy of the parallel component (\parallel) is twice that of the perpendicular one (\perp). Moreover, the asymmetric distribution agrees with the previously presented 3D angular distribution of the THz emission in Figure 17. In addition, the polarization features also agree with the experimental data observed previously in Figure 16, where a stronger radial field component was measured in the direction of the laser propagation.

So far we have presented CTR emission quantities with no wavelength dependence. To show the spectral components of the CTR, we combine the coherence and diffraction

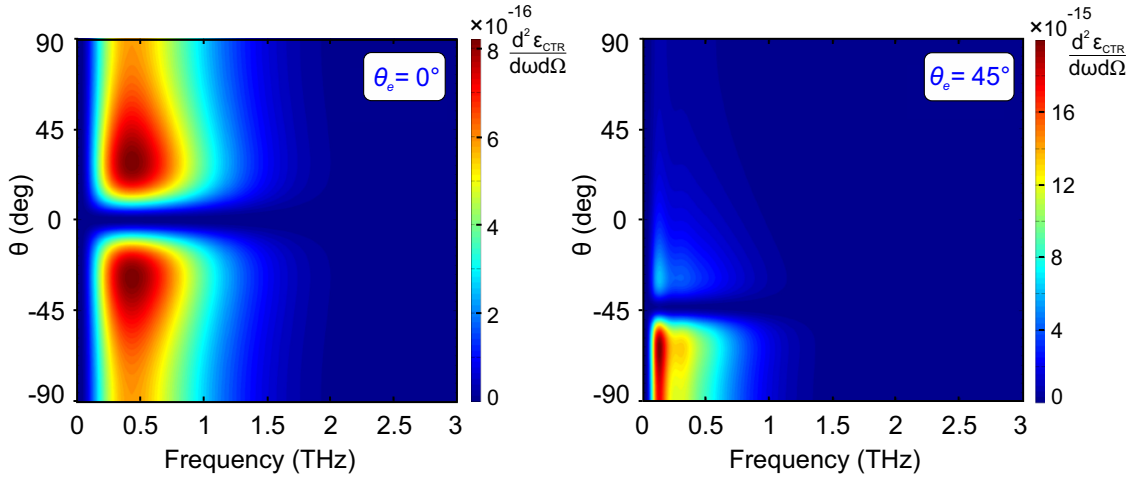


Figure 37: Angular distribution of energies ε_{CTR} of different spectral components in the THz range in the form of CTR emission from hot electron bunches exiting the target at 0° (left) and 45° (right).

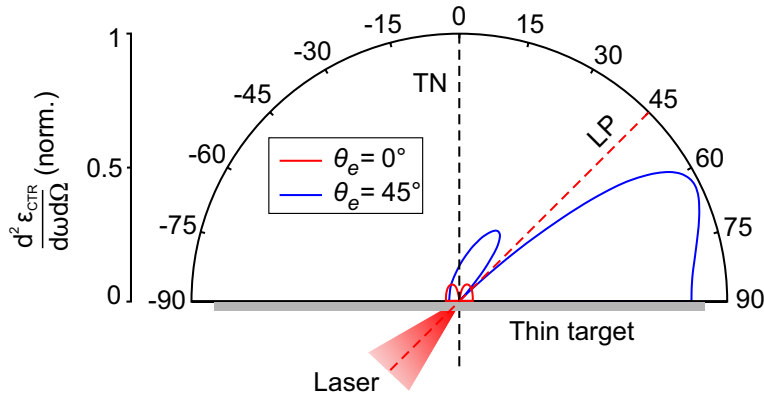


Figure 38: Angular distribution of the CTR emission in the radiation plane $\phi = 0^\circ$. TN is the target normal direction and LP is the laser propagation direction.

functions given previously. The angular and spectral distributions of CTR emission from electrons exiting the target at 0° and 45° are shown in Figure 37. We note that most of the energy of the radiation lies within a spectral range of < 2 THz. In addition, an alternative perspective on the angular distribution of CTR radiation in the emission plane perpendicular to the target ($\phi = 0^\circ$) can be seen in Figure 38.

To obtain the temporal structure of the emitted CTR, we can switch to the time domain by performing an inverse Fourier transform on the angularly integrated spectra. The resulting temporal waveform can be seen in Figure 39. The pulse durations of the CTR emission at FWHM are $\tau_{0^\circ} \approx 295$ fs and $\tau_{45^\circ} \approx 487$ fs. These numerical estimates are comparable to the experimentally measured THz pulse durations with

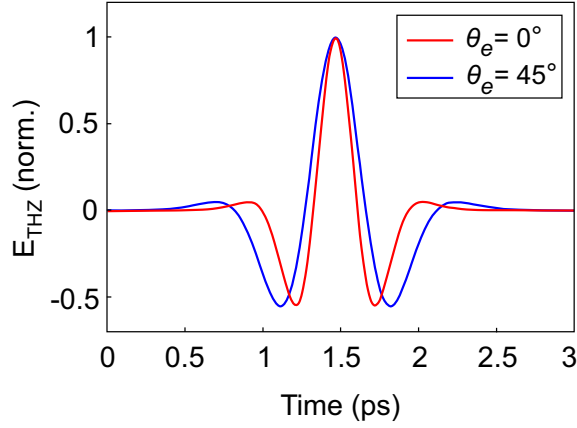


Figure 39: Temporal structure of the CTR-THz pulses from the inverse Fourier transform on the angularly integrated spectra. The pulse durations of the CTR emission at FWHM are $\tau_{0^\circ} \approx 295$ fs and $\tau_{45^\circ} \approx 487$ fs.

the electro-optic technique reported in Figure 14.

The expected CTR emission due to electron bunches exiting the target rear surface has a broad angular distribution due to the contribution of a large number of low-energy electrons with a Boltzmann-like distribution. The broadening in the CTR emission is more significant in the 0° direction due to the lower temperature of the electron emission ($T_{e,0} = 0.5$ MeV) along the target normal (0°) compared to the electrons exiting at 45° , ($T_{e,45} = 1.8$ MeV). Moreover, the asymmetry in the angular profile of the CTR from electrons exiting at 45° can be attributed to the oblique trajectory of the electron bunch with respect to the target surface. Another possible explanation could be the slight asymmetry in the distribution of electrons on both sides of 45° -direction, as seen in Figure 19 in the previous chapter. It is worth mentioning that additional effects on the CTR emission, such as electron scattering inside the target material, are neglected, although scattering effects would be detrimental for low-energy electrons, however, for MeV electrons at relativistic intensities, can be neglected.

5.2 Sheath radiation

We established that the emission of THz radiation can follow the transient dynamics of charged particles during the interaction. A prominent application of the interaction of intense laser pulses with thin targets is the acceleration of ions by the target normal sheath acceleration (TNSA). Such a dynamical mechanism could result in the emission of coherent THz radiation during the interaction. In short, during the interaction of the laser with the target, hot electrons propagate through the target to the rear side,

and some of the electrons with sufficient energy escape toward the vacuum leading to an unbalanced charge at the target's rear surface, which in turn creates a strong electrostatic field of the order of TV/m [46]. The field is strong enough to trap and confine most of the escaping electrons, creating a hot electron sheath with a Debye length of $\lambda_D = \sqrt{\epsilon_0 k_B T_e / n_e e^2}$. In addition, the electrostatic field ionizes the neutral atoms found at the rear surface, leading to the expansion of the plasma and acceleration of the positively charged ions in the target normal direction.

According to the plasma expansion model by Mora [51,52], the electrostatic potential Φ can be obtained from the Poisson equation $\epsilon_0 \partial^2 \Phi / \partial x^2 = e(n_e - n_p)$, taking into account the electron and proton densities. At the beginning of the expansion, $t = 0$, the proton density, n_p , is steplike with $n_p = n_{e,0}$ in the target. Thus, at the front of the expanding plasma sheath, $n_{e,\text{front}} \neq n_{p,\text{front}}$. The unbalanced charge densities lead to an emerging current equivalent to the uncompensated net charge where eventually, the accelerated ions reach the front. The dynamics of the moving net charge can be thought of as a transient electric dipole, and may give rise to a dipole-like emission of electromagnetic radiation.

By adapting the treatment found in Mora's work [51] and by assuming that the sheath is a pure electron-proton plasma expanding in the z -direction (TN), the velocity of the expanding plasma front v_f as a function of time t is estimated as

$$v_f(t) \simeq 2c_s \ln(\tau + \sqrt{\tau^2 + 1}), \quad (77)$$

where $c_s = (Zk_B T_e / m_i)^{1/2}$ is the ion-acoustic velocity, $\tau = \omega_{pi} t / \sqrt{2e_N}$ is the normalized acceleration time, with $\omega_{pi} = (n_{e,0} Z e^2 / m_i \epsilon_0)$ is the ion plasma frequency, $n_{e,0}$ is the electron density in the unperturbed plasma, Z is the ion charge number, and $e_N = 2.718\dots$. The plasma expansion velocity increases steadily with time until $t = \tau_0 = \sqrt{2e_N} / \omega_{pi}$. Afterward, for $t > \tau_0$, the acceleration diminishes when the ions reach the expansion front, where we can consider the latter to be moving with a uniform velocity. This model leads to a change in the electron and proton densities at the expanding plasma front which is given as [51]

$$n_{e,\text{front}} \simeq 2n_{e,0} / \omega_{pi}^2 t^2, \quad (78)$$

$$n_{p,\text{front}} \simeq 4n_{e,0} / \omega_{pi}^2 t^2, \quad (79)$$

We can describe the time-dependent charge density distribution and the plasma

current distribution along the z -direction (TN, 0°) as

$$\rho(r, z, t) = e[n_{e,\text{front}}(z, t) - n_{p,\text{front}}(z, t)] \exp(-r^2/R^2), \quad (80)$$

$$j(r, z, t) = -v_f(t)\delta(z - v_f t + \lambda_D)\rho(r, z, t), \quad (81)$$

where $R = r_0 + d \tan \alpha \approx 3.4 \mu\text{m}$ is the transverse radius of the sheath with $r_0 = 1.25 \mu\text{m}$ is the laser focal spot radius, $\alpha = 23^\circ$ is the half-angle of the electron emission obtained from the angular distribution of the proton beam in Figure 22, and $d = 5 \mu\text{m}$ is the target thickness. Since the intensity and temporal profile of the focused laser is Gaussian, we consider the density distribution of electrons in the sheath to be Gaussian as well, and their mean energy at a defined position to be radially homogeneous [108].

The transient nature of the plasma sheath dynamics can lead to the emission of radiation which can be estimated from the Liénard-Wiechert potential [109]. For an observer far from the plasma current source ($r \gg \lambda_D$), the near-field term can be neglected and only the radiation term in the far-field from the accelerated charge is present. The electric field of the radiated wave can be obtained by incorporating the charge density ρ and plasma current j given previously as follows:

$$\xi(\mathbf{r}, t) = \frac{1}{4\pi\epsilon_0} \int \left\{ \frac{\mathbf{n}}{cr} \frac{d}{dt} [\rho(\mathbf{r}', t')]_{\text{ret}} - \frac{1}{c^2 r} \frac{d}{dt} [j(\mathbf{r}', t')]_{\text{ret}} \right\}, \quad (82)$$

In our case, we treat the charge and current densities with arbitrary time dependence. Thus solving the radiation fields in the frequency domain is favored due to dispersion and retardation. Therefore, we write the electric field in Fourier space as

$$\xi(\mathbf{r}, \omega) = -k(\omega) \frac{qc_s \sin \theta}{4\pi\epsilon_0 rc} \exp[ik(\omega)r] F(\omega, \theta), \quad (83)$$

where $k(\omega) = \omega/c$ and $q = e\rho V_{\text{sheath}}$ is the net charge in the sheath with $V_{\text{sheath}} = \pi R^2 \lambda_D$ being the sheath volume. Similar to the previously presented, the form factor $F(\omega, \theta)$ specifies the frequency-angular dependence of the radiation field and defines a space-time Fourier transform of the current density, which can be expressed as [110]

$$F(\omega, \theta) = i\omega\tau_0 \frac{1 - \exp(-1 - i\omega\tau_0)}{(1 + \omega\tau_0)^2} \exp\left(-\frac{\omega^2 R^2 \sin^2 \theta}{4c^2}\right), \quad (84)$$

Finally, by employing the sheath parameters, we can estimate the sheath radiation emitted during the expansion of the plasma into the vacuum, leading to the radiated

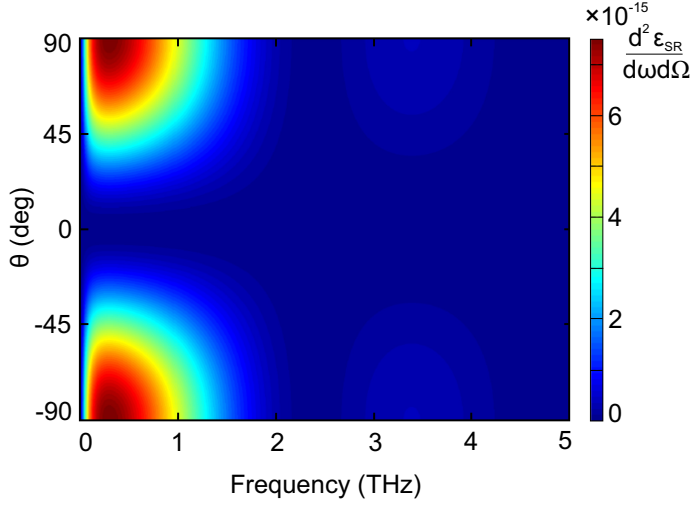


Figure 40: Spectral and angular distribution of the radiation emission due to the plasma sheath dynamics in the THz range. Most of the radiation is emitted normal to the direction of acceleration.

energy per angular frequency and solid angle as

$$\frac{d^2 \epsilon_{\text{SR}}}{d\omega d\Omega} = \frac{c\epsilon_0 r^2}{\pi\omega^2} |\xi(\omega)|^2 = \frac{q^2 c_s^2}{4\pi^3 \epsilon_0 c^3} |F(\omega, \theta)|^2 \sin^2 \theta. \quad (85)$$

In our case, the protons are accelerated via the TNSA mechanism in the target normal direction (TN) with a half-angle opening of $23^\circ \pm 1^\circ$ as experimentally verified in Figure 22. The emitted radiation during the sheath acceleration process is numerically estimated by using the experimentally acquired electron energy spectra and temperature of the bunch propagating in the TN-direction. The resulting angular and spectral profiles of the sheath radiation are shown in Figure 40. It is clear that most of the emission is emitted at large angles with respect to the target normal, with emission spectra being mostly below 2 THz.

The spectrally integrated angular distribution of the SR emission is shown in Figure 41. We note that, unlike CTR, SR radiation is emitted predominantly at wide angles with respect to the direction of acceleration and deceleration of charged particles in the plasma sheath (z -direction). Similar to before, we obtain the temporal waveform of the SR by performing IFT on the angularly integrated SR spectrum, resulting in a FWHM pulse duration of $\tau_{\text{SR}} = 350$ fs. We find that the estimated theoretical value of the SR pulse duration lies in the range of the experimentally measured THz pulses at a wide detection angle presented previously in Figure 14, although a wide-angle detection may accept emission from both suggested mechanisms, CTR and SR.

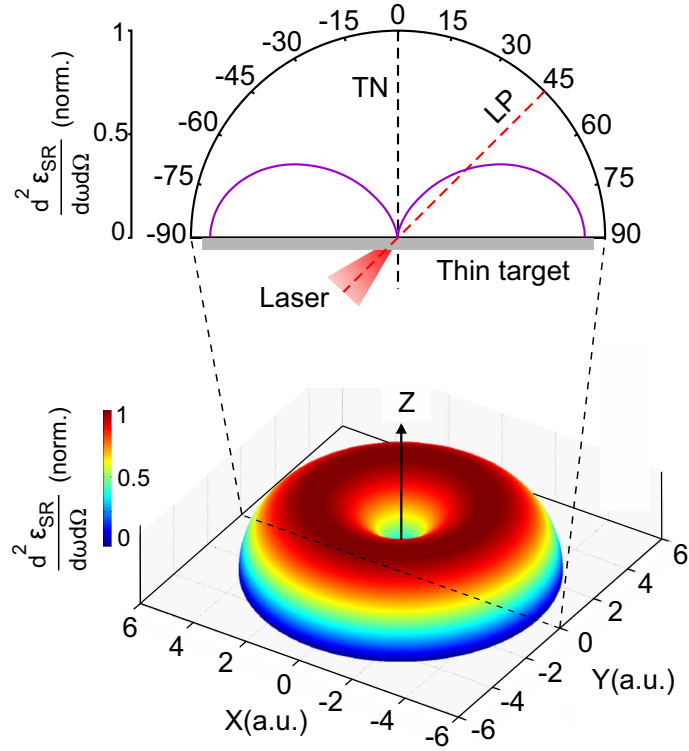


Figure 41: Angular distribution of sheath radiation (SR) with a cross-section along the XZ-plane perpendicular to the target. TN is the target normal along the z-direction and LP is the laser propagation direction.

5.3 Bunch length estimation

We can reconstruct the longitudinal length of an ultrashort electron bunch from the spectrum of coherent transition radiation emitted by the bunch as it exits the thin target [111]. For this purpose, we employ the experimentally obtained CTR temporal waveforms from the single-shot electro-optic measurements reported in Chapter 3. The minimum pulse duration that can be measured with this technique is limited by the crystal response function, which is around 111 fs for the thinnest GaP crystal [8]. Therefore, it is valid to consider the experimentally recorded temporal duration as the actual pulse duration of the radiation. The CTR spectrum obtained from the FT of the temporal waveform is determined by the form factor $F(\omega)$, which sets the high cutoff frequency, and diffraction effects, which set the low cutoff. The longitudinal bunch length σ_z can then be extrapolated and compared to the numerical estimate.

Temporal measurements of THz radiation in Chapter 3 revealed 3 main consecutive THz pulses, whose origin can be attributed to the generation mechanisms discussed previously. We consider pulses 1 and 2 generated by the CTR process as they appear

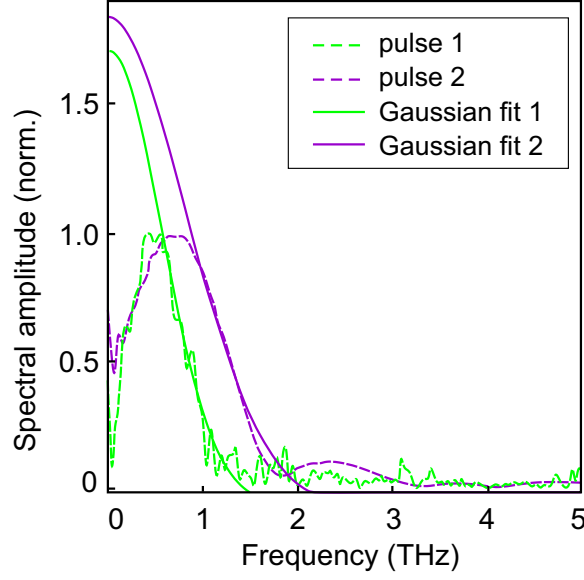


Figure 42: Measured spectra of two CTR pulses (dashed lines) with the corresponding Gaussian fit function of Equation 87 (solid lines).

early in time. The bunch form factor for an uncorrelated spatial distribution is denoted as $F(\omega) = F^\perp(\omega)F^\parallel(\omega)$, where $F^\perp(\omega)$ is related to the transverse distribution of the electron bunch and $F^\parallel(\omega)$ is related to the longitudinal profile. The electron bunch that generates the CTR can be assumed to have a Gaussian spatial profile, and with the lateral size $\sigma_r \ll \sigma_z$ and $\omega = 2\pi\nu$, the form factor reduces to [112]

$$F(\omega) \sim \exp\left(-\frac{\omega^2 \sigma_z^2}{c^2}\right), \quad (86)$$

To define the longitudinal size σ_z we employ the following Gaussian function on the CTR spectrum to determine the spectral width of the CTR pulse σ_{rms}

$$g(\nu) \sim \exp\left(-\frac{(\nu - \nu_c)^2}{2\sigma_{\text{rms}}^2}\right), \quad (87)$$

An analytical expression for the bunch size σ_z with spectral width σ_{rms} can be written as [113]

$$\sigma_z \approx \frac{1}{2\sqrt{2\pi}} \left(\frac{c}{\sigma_{\text{rms}}}\right), \quad (88)$$

The corresponding spectra with the resulting fits are shown in Figure 42. Additionally, we deliver the computed results from the CTR fits and the estimated values from the electron energy spectra in Table 1. It is worth mentioning that the finite size

From CTR spectra fits		
Pulse	σ_{rms} (THz)	σ_z (μm)
1	0.552	61
2	0.825	41
From hot electron spectra		
θ_e	-	σ_z (μm)
0°	-	36
45°	-	50

Table 1: Comparison of the extrapolated values of the bunch lengths σ_z from the CTR spectra σ_{rms} and the hot-electron spectra.

of the plasma-vacuum boundary suppresses, i.e defines, the low-frequency components in the CTR spectrum. To verify this effect, we evaluate the distortion in the Gaussian fit in the region $\nu \gg \sigma_{\text{rms}}$ in the above figure. We note that the spectral region above pulses $\sigma_{\text{rms},1} = 0.552$ THz and $\sigma_{\text{rms},2} = 0.825$ THz is only weakly distorted, confirming the reliability of the bunch length estimates. After this acknowledgment, we find a reasonable agreement between the bunch sizes obtained by fitting a Gaussian function on the detected CTR spectra as $41 \mu\text{m}$ and $61 \mu\text{m}$, and the estimated values from the measured energy spectra of the hot electrons as $36 \mu\text{m}$ and $50 \mu\text{m}$. This further demonstrates the reliability of the extrapolation of the temporal properties of electron bunches generated during the laser-solid interaction from the spectral characteristics of the CTR emitted by the bunches.

5.4 Comparison of the model and the measured data

Given the experimentally measured THz pulses in Chapter 3 and the calculated THz beam profiles, we may now compare both data sets in order to fully characterize the phenomenon of picosecond radiation generation from the rear surface of the target during the laser-plasma interaction. Figure 43 combines the following:

Modeled:

- 1- the dashed blue line represents the estimated angular distribution of the combined coherent transition radiation emitted by the electron bunches when exiting the target at 0° and 45° as shown in Figure 38.

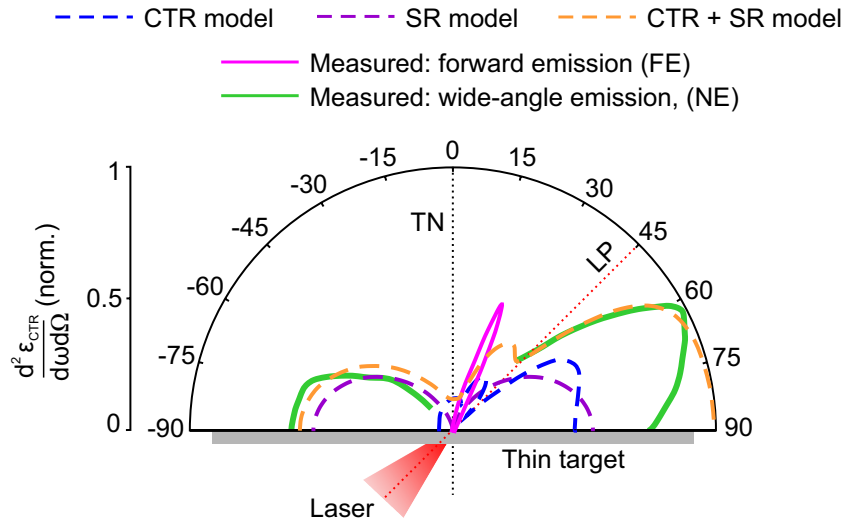


Figure 43: Comparison of the angular intensity distributions of the modeled and measured sub-picosecond radiation emission in the THz spectral range during the laser-thin target interaction. Numerical estimates include the coherent transition radiation CTR emission estimated for the electrons exiting the target rear surface (dashed blue), and sheath radiation emitted by the plasma expansion (dashed magenta). The sum of these two numerical estimates is plotted in dashed orange. The measured THz emission consists of forward emission in solid pink and noncollinear emission in solid green

2- the dashed magenta line represents the expected sheath radiation SR from the sheath acceleration process TNSA shown in Figure 41. The dashed orange line shows the sum of the three numerically estimated emissions CTR_0 , CTR_{45} , and SR.

Measured: the solid line indicates the experimentally measured angular distribution of the THz radiation taken from Figure 17, which is the sum of the forward emission (FE) and wide-angle non-collinear emission (NC).

Here we report on the good agreement between the experimentally measured and theoretically estimated THz beam profiles, and we may now characterize the emission process for each detected THz pulse. For this aim, we consider the propagation time taken by the charged particles to exit the target at various angles, as well as the geometry of the emission and amplitude of the transient peaks. Additionally, we may remind the reader about the collection geometry of the THz emission shown in Figure 12, which consists of the forward emission FE and the wide-angle non-collinear emission NE. With this in mind, we may attribute the first peak observed in both detection geometries (Figure 14) to the CTR emission due to the electrons

escaping in the target normal direction. The strong second peak in the NC can originate from the CTR emission by the energetic electrons accelerated by the ponderomotive force of the laser exiting along the laser propagation direction at 45° . The same origin can be given to the weak second peak in the forward emission albeit a rather weaker signal due to the narrow solid angle of detection geometry and as a result, the collection optics employed for the FE measurements did not collect the whole left lobe of this CTR emission. The CTR_{45° pulse is the strongest emission seen in the beam profile, which could also contain high-frequency components extending beyond the optical regime [114]. However, such high-frequency components do not affect the measurements as they are filtered out using the appropriate filters. The temporal durations from both measurements are comparable while the discrepancy in the field strengths can be attributed to the solid angles of the collection optics.

Moving on to the third pulse presented in Figure 14, which appears after 2.89 ± 0.02 ps, it can be attributed to the expansion of the plasma sheath described by the TNSA acceleration process. This dipole-like emission is caused by the transient dynamics of the low-energy electrons exiting the target in the TN direction and, subsequently, the following positively charged particles. The measured signal amplitude is higher in the NE measurement than in the FE measurement because such dipole-like emission occurs over a wide angle.

5.5 Conclusion

In this chapter, we have presented a theoretical estimate of the THz radiation emission from the conditions found during our experiments in this work. The experimental data presented in Chapter 3 can be explained by coherent transition radiation (CTR) and plasma sheath radiation (SR). CTR radiation is emitted when accelerated electrons exit the thin target and such radiation strongly depends on the energy and number of electrons. We have found that the CTR radiation from accelerated electron bunches in the direction of laser propagation (LP) is an order of magnitude higher than that from electrons emitted in the target normal (TN) direction. Additionally, the low-energy electrons emitted in the TN direction generate a symmetric distribution of CTR, while the contribution from energetic electrons emitted in the LP direction is inhomogeneous and tilted at wider angles. Further, we have shown that most of the energy of the CTR emission lies in the THz spectral range between 0.1 and 1.5 THz.

The second possible source of picosecond radiation is the transient dynamics of the expanding plasma sheath formed at the back surface of the target in the TNSA

mechanism. This can lead to plasma sheath radiation (SR) that is predominantly emitted in the non-collinear direction, that is, away from the target normal TN direction. The SR spectrum mostly contains frequencies below 2 THz. It is worth mentioning that the plasma sheath expansion model used here only considers the expansion in the z -direction and is expected to fail in three dimensions. However, the 3D treatment does not significantly affect the longitudinal expansion shorter than the transverse sheath size R [108, 115, 116]. For instance, at $t = t_{acc}$, the plasma front propagates $z_f \approx \lambda_D \approx 0.53 - 1 \mu\text{m}$ which is smaller than the transverse size $R \approx 3.4 \mu\text{m}$. Thus for a time interval $t \leq t_{acc}$, our treatment using the 1D model suffices in describing the expansion and the corresponding dipole radiation.

Finally, we have estimated the longitudinal bunch duration of the electron bunches σ_z . We have calculated the expected longitudinal duration of two fast electron bunches from the measured CTR spectrum and compared them to the values obtained from the hot electron spectra. The reasonable agreement between the two estimates suggests that CTR in the THz range is a valid diagnostic for particle bunches generated during laser-matter interaction.

6 Direct visualization of Coulomb field of relativistic electron bunches from laser-plasma interaction

In this chapter, we present novel experimental results on the detection of the spherical wavefronts of the Coulomb field around relativistic electron bunches during the interaction of an ultrashort laser pulse with a thin metallic target. We also investigate the spatiotemporal evolution of the detected wavefronts as the relativistic electrons propagate away from the target. When a short and intense laser pulse interacts with a thin metallic foil, energy is transferred to electrons in the plasma through various mechanisms. These energetic electrons can propagate through and out of the target on timescales comparable to the main laser peak. Previous studies have focused on the energy and angular properties of the electron emission [117], but accurate time-resolved studies have been challenging due to the limitations of the diagnostics compared to the short timescales of the relativistic regime. Obtaining temporal information on the electron emission is crucial for post-acceleration using synchronized energy sources like optical [22] and THz [23] post-acceleration schemes, which rely on velocity and phase matching criteria. In this chapter, we demonstrate a proof of concept for measuring the temporal profile of electron emission at near-relativistic energies. Furthermore, mapping the structure of the contracted Coulomb field can accurately represent the temporal dynamics of the interaction, as the mechanism varies depending on the interaction parameters. Relativistic electrons generate anisotropic and radially extended Coulomb fields perpendicular to the electron beam direction, which can be detected using the electro-optic effect. Electro-optic detection offers non-destructive and single-shot characteristics, making it an ideal diagnostic tool in accelerator facilities.

6.1 Experimental setup

The experimental setup is presented in Figure 44, where laser pulses from the JETi-40 laser system (see appendix 8) are focused onto a thin metallic target using a 4-inch 45° off-axis parabolic mirror. We employed aluminum and titanium targets with a thickness of $5\ \mu\text{m}$. The laser spot size at the focus was imaged to be around $12\ \mu\text{m}^2$ at $(1/e^2)$ with a laser pulse energy of $0.65\ \text{J}$ at target and a pulse duration of $32\ \text{fs}$, accounting for a light intensity above $1 \times 10^{19}\ \text{W}/\text{cm}^2$. Further detailed properties of the interaction can be found in Section 3.1.

The detection system in this experiment is based on the electro-optic effect and is

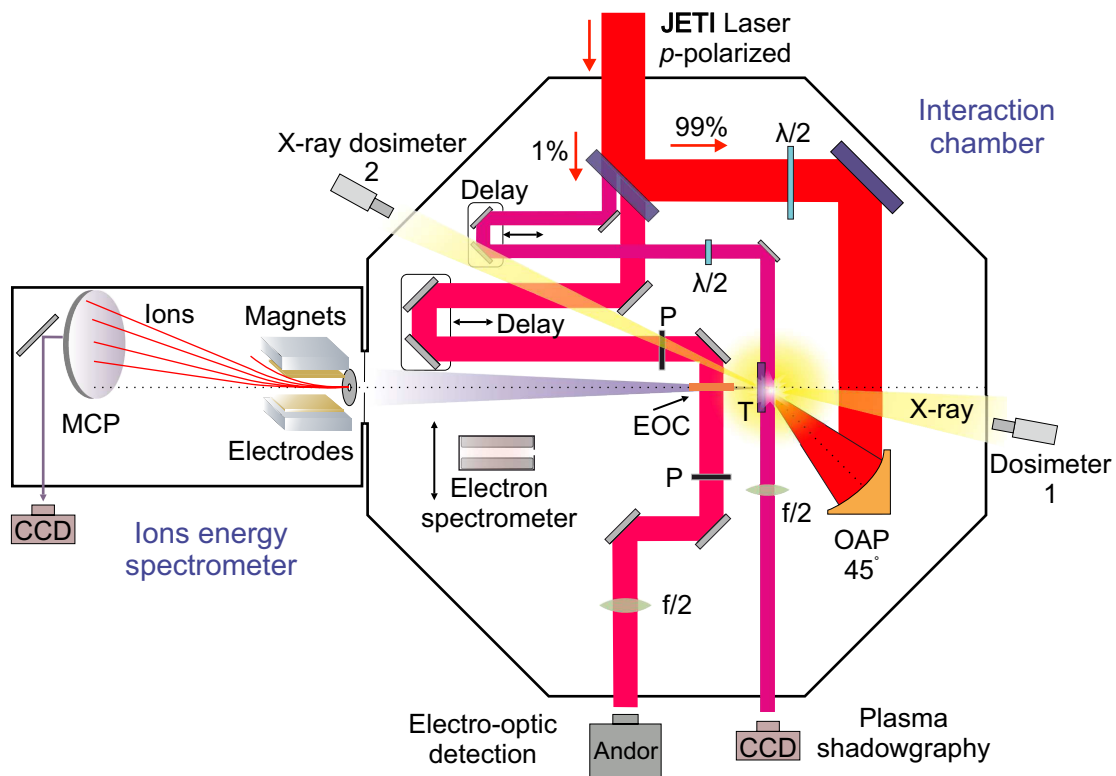


Figure 44: A simplified schematic of the experimental setup at JETi-40 for the observation of long-lasting transient emission. Laser pulses are focused onto a thin metallic target (T) reaching light intensities above $1 \times 10^{19} \text{ W/cm}^2$. Electrons are accelerated on the irradiated side and then transported through the thin target, leading to transient dynamics of charged particles on the rear side. A detailed temporal structure of the resulting emission in the THz regime is obtained using an electro-optic detection technique with a delayed laser probe. In addition, the emerging plasma at the front surface of the target is simultaneously imaged via time-resolved shadowgraphy. Additional diagnostics: a Thomson-parabola spectrometer, electron spectrometers, and X-ray dosimeters. P is a polarizer, $\lambda/2$ is a half-wave plate, and EOC is an electro-optic crystal.

similar to the one we presented previously in Chapter 3.2. We employed Zinc Telluride (ZnTe) crystals with thicknesses of 200 and 500 μm , all are cut along the $\langle 110 \rangle$ crystal plane. A preview of the detection setup is shown in Figure 45. The ZnTe crystal is placed in a special frame with its upper edge fully exposed and aligned parallel to the path of the accelerated electrons along the target normal direction at 0° and, separately, at the laser propagation direction at 45° . The frame is mounted on a high-precision motorized 3D stage with submicrometer resolution (from Smaract). In addition, the crystal optical x-axis $[-110]$ is aligned parallel to the polarization direction of the probe beam to ensure maximum electro-optic signal [118]. A blocking plate of various

6 DIRECT VISUALIZATION OF COULOMB FIELD OF RELATIVISTIC ELECTRON BUNCHES FROM LASER-PLASMA INTERACTION

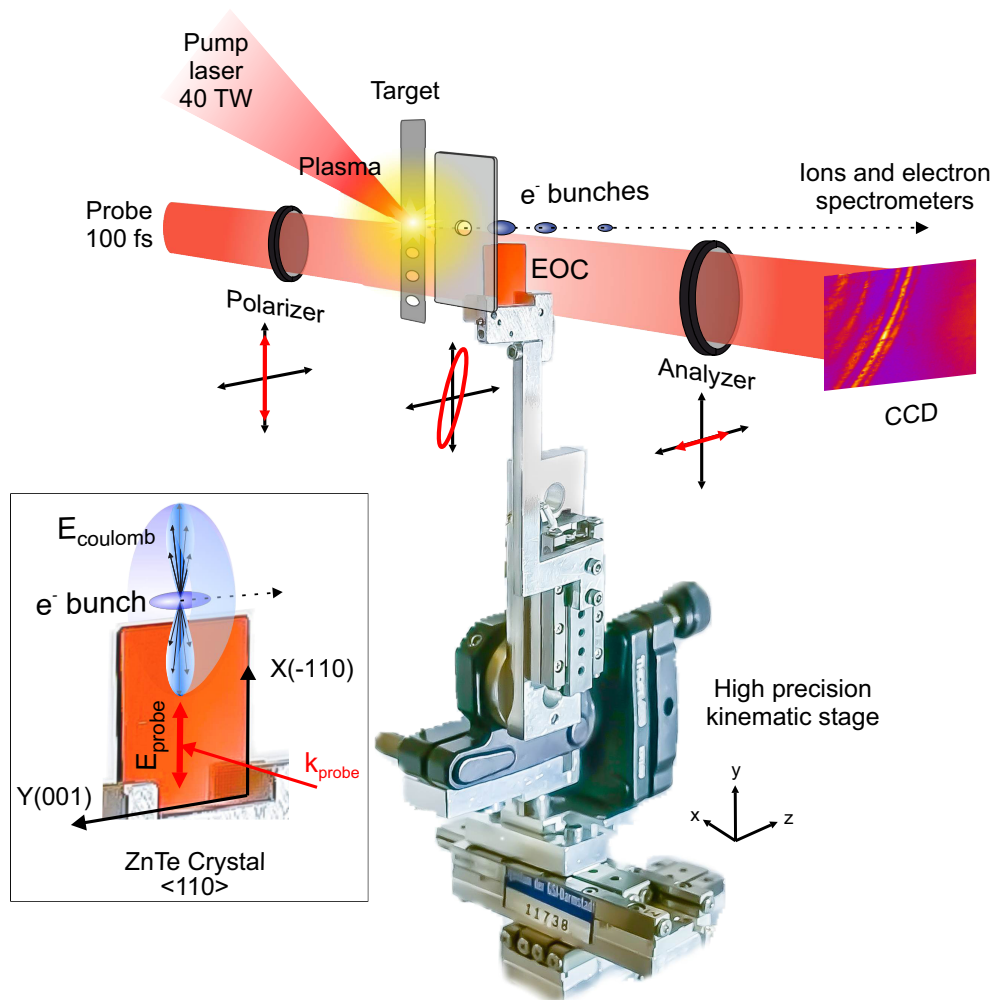


Figure 45: A simplified preview of the electro-optic setup employed to map the temporal profile of long-lasting picosecond dynamics during intense laser-thin foil interaction. Relativistic electron bunches (blue) pass over a thin electro-optic crystal (ZnTe). The transient electric field creates a time-dependent birefringence inside the crystal, which induces an optical phase shift in a synchronized 100 fs optical probe. A pair of crossed polarizers converts that into a spatial intensity distribution recorded on a CCD camera leading to a single-shot temporal-to-spatial conversion. Inset shows the orientation of the Coulomb field of an electron bunch and the polarization direction of the probe beam with respect to the z -axis of the crystal.

thicknesses and materials with a 1 mm hole is used to shield the detection system from unwanted electromagnetic radiation and to protect the crystal from debris.

As illustrated in Figure 45 and previously in Figure 8, transient electric fields in the form of contracting Coulomb field of relativistic electron bunches from the interaction traverse the top of the EO crystal. Although the transverse electric field of the electron

bunch is radially polarized, at the position of the laser beam at a distance r from the electron bunch, the field can be approximated as a linearly polarized THz field [57]. This field acts on the EO crystal as a quasi-DC bias, inducing the Pockels effect, which in turn generates a transient birefringence inside the crystal. An ultrashort optical pulse is incident normal onto the EO crystal to probe the time-dependent variation of the birefringence. As the probe pulse propagates orthogonal to the direction of the electron beam, the time profile of interest is encoded at different spatial locations for each time delay, leading to a single-shot temporal-to-spatial conversion. Using a pair of crossed polarizers, the induced optical phase shift across the full area of the crystal is converted into an intensity modulation, which is subsequently detected by a high-performance 16-bit-cooled CCD camera (Andor).

The probe pulse is collected from the main laser pulse through the first dielectric mirror with a transmission of 0.4% and a thickness of 18 mm, leading to the stretching of the probe pulse [119]. The final probe pulse duration was measured by setting up a scanning third-order cross-correlator (Sequoia, Amplitude Technologies) inside the chamber and was found to be less than 100 fs. In addition, we consider the exact time event of the arrival of the main laser pulse at the focus as the time zero by performing plasma shadowgraphy. This was achieved by utilizing a dedicated objective to image the focal region via the probe beam which has a diameter of about 5 cm that also covers the interaction point. During time calibration i.e. setting time zero, the target was lowered and the energy of the main pulse was reduced to a few microjoules by turning off the final amplification stage and using neutral density filters of known thickness and material. Next, the time delay was varied using a linear stage inside the interaction chamber in steps of 10 μm , corresponding to 33 fs. As a result, a faint but still detectable plasma shadow in the air was imaged using a lens and a CCD camera.

Similar to previous experiments, other diagnostics are employed to characterize the interaction conditions, such as a Thomson-Parabola ion spectrometer, electron spectrometers, and X-ray dosimeters.

6.2 Observations of relativistic electron bunches along the target normal direction

In the following, we demonstrate a direct visualization of the Coulomb field of relativistic electron bunches from the laser-plasma interaction along the target normal direction. We placed two ZnTe electro-optic crystals in the crystal holder as shown

6 DIRECT VISUALIZATION OF COULOMB FIELD OF RELATIVISTIC ELECTRON BUNCHES FROM LASER-PLASMA INTERACTION

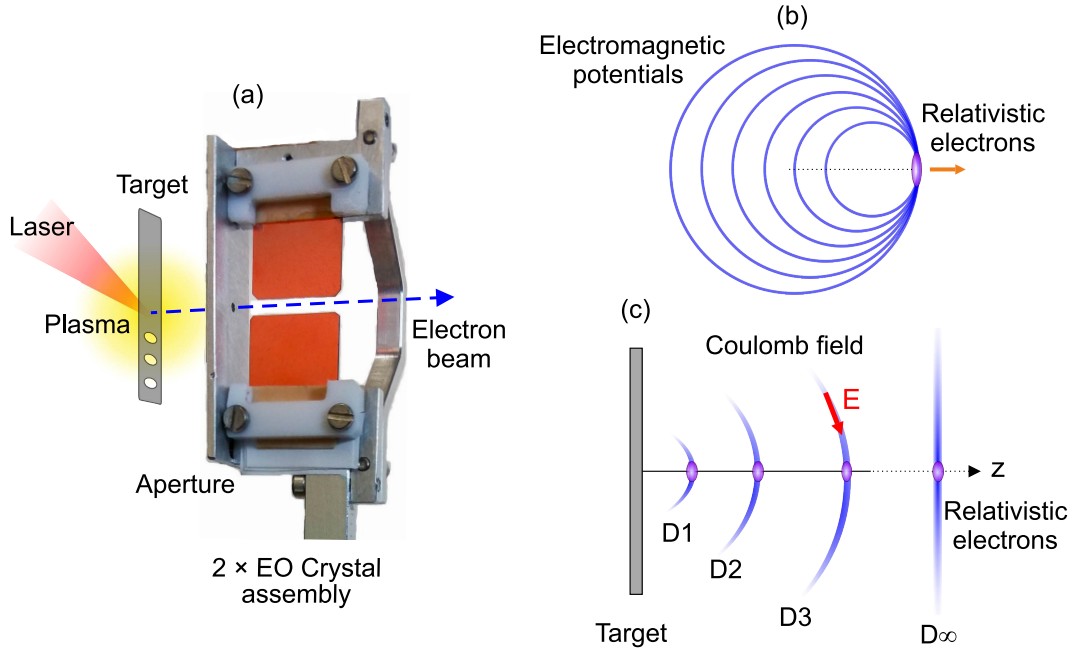


Figure 46: (a) Two EO crystals assembly for observing the evolution of the Coulomb fields of relativistic electron bunches. (b) Illustration of a spherical wavefront generated by the superposition of electromagnetic fields emitted by a relativistic electron bunch. (c) Evolution of the spherical electromagnetic potentials around a relativistic electron at distances $D_1 < D_2 < D_3 < D_\infty$ after passing through a metallic boundary. The wavefront can be considered to be flat at D_∞ . Vector E represents the electric field of the electromagnetic wave derived by the Liénard-Wiechert potentials with axial symmetry around the z -axis.

in Figure 46. Both crystals are placed along the target normal direction as shown in Figure 45 for a single crystal. The upper crystal has a thickness of $500 \mu\text{m}$, while the bottom crystal has a thickness of $200 \mu\text{m}$, both at a distance of 6 mm from the interaction point. In addition, an aluminum plate with a thickness of 1 mm and an aperture of 1 mm covers both crystals, with a distance of 1.3 mm between the crystals and the plate. The two crystals are separated by 1.67 mm , and both are centered around the electron beam axis defined by the aperture. We focused a laser pulse with a maximum available energy of 0.65 J onto a $5 \mu\text{m}$ thick aluminum target, resulting in an intensity of $\sim 5 \times 10^{19} \text{ W/cm}^2$.

We varied the probe delay and recorded the EO signal accordingly as shown in Figure 47. We report the direct detection of spherical wavefronts of Coulomb fields accompanying relativistic electron bunches emitted during the intense laser-plasma interaction. The EO measurements show concentric semi-spherical profiles of various intensities propagating near the speed of light with radii equal to the propagation

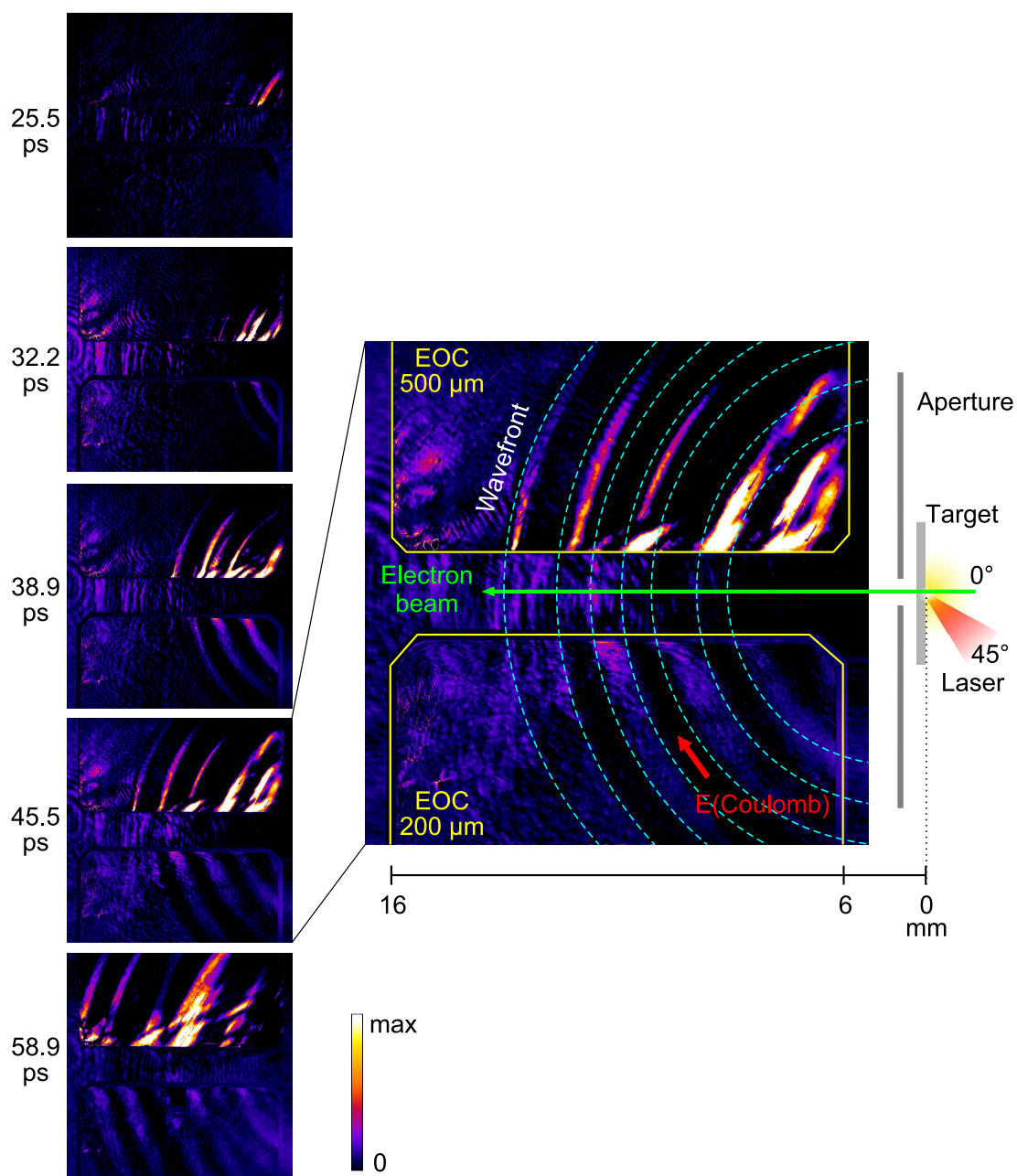


Figure 47: Observations of spherical wavefronts of Coulomb fields accompanying relativistic electron bunches during the laser-plasma interaction. The panels on the left show the electro-optic measurements at various probe delays with one instant enlarged for clarity. The outer edges of the two EO crystals are traced in yellow and can be seen in Figure 46 (a).

distance. The observation starts from 6 mm away from the interaction point up to the full length of the crystal of 16 mm. The EO signal extends over 15 ps in time, and while additional EO signals can still be observed later, they lack the same well-defined

structure and appear objectively faint and diffuse. The long EO signal can be explained by the velocity dispersion of the electrons, leading to a dispersed temporal structure that extends spatially with propagation distance, as we will discuss later.

So far, we have observed the electric field profile around the relativistic electron bunches as concentric spherical waves. To explain the spherical shape, we consider the energetic electrons in the plasma when their Coulomb field is shielded, however, once the electrons are ejected out of the plasma volume, the Coulomb field distribution evolves from the plasma-vacuum interface due to the loss of quasi-neutrality [120]. As the electron bunches propagate away from the target, the Coulomb field wavefronts expand as spherical waves with the interaction point located at the center.

Special relativity predicts a contraction of the Coulomb field around a charged particle moving uniformly at high velocity [109]. The associated characteristic electric field profile can be derived using the Liénard-Wiechert potentials assuming the Lorentz gauge under the Lorentz transformation. The wavefront of the Coulomb field around a moving electron is derived by integrating multiple retarded spherical electromagnetic potentials propagating at the speed of light, see Figure 46b. In the general case, the spherical curvature of the electric field wavefront caused by boundary passage can be ignored at infinity, as depicted in Figure 46c.

We can consider the contracted Coulomb field around a relativistic electron bunch in the propagation direction of the beam as a transient half-cycle terahertz pulse because of the unidirectional nature of the field amplitude and the temporal scale of the event. The electric field vector points toward the electron bunch, implying that each crystal perceives the field in the opposite direction. However, we employed a crossed-polarizer scheme where the resulting signal is proportional to the square of the electric field. When crossing the two polarizers, however, we typically place a single crystal in between as a reference to minimize background signal caused by incomplete extinction due to inherent birefringence and mechanical stresses in the crystal [67]. A phase shift is introduced into the detection scheme when we place the thinner crystal side-by-side with the thicker one to create a two-crystal system. This shift can alter the helicity of the probe in the thin crystal due to the lower material thickness and the increased susceptibility to mechanical stress caused by the holder. This alteration could explain the discrepancy in the amplitude direction of the observed signal between the thinner (bottom) and the thicker crystal (top) in Figure 47. Finally, the high oscillations, appearing as thin and intense lines on the thicker crystal at the top, will be discussed in more detail later.

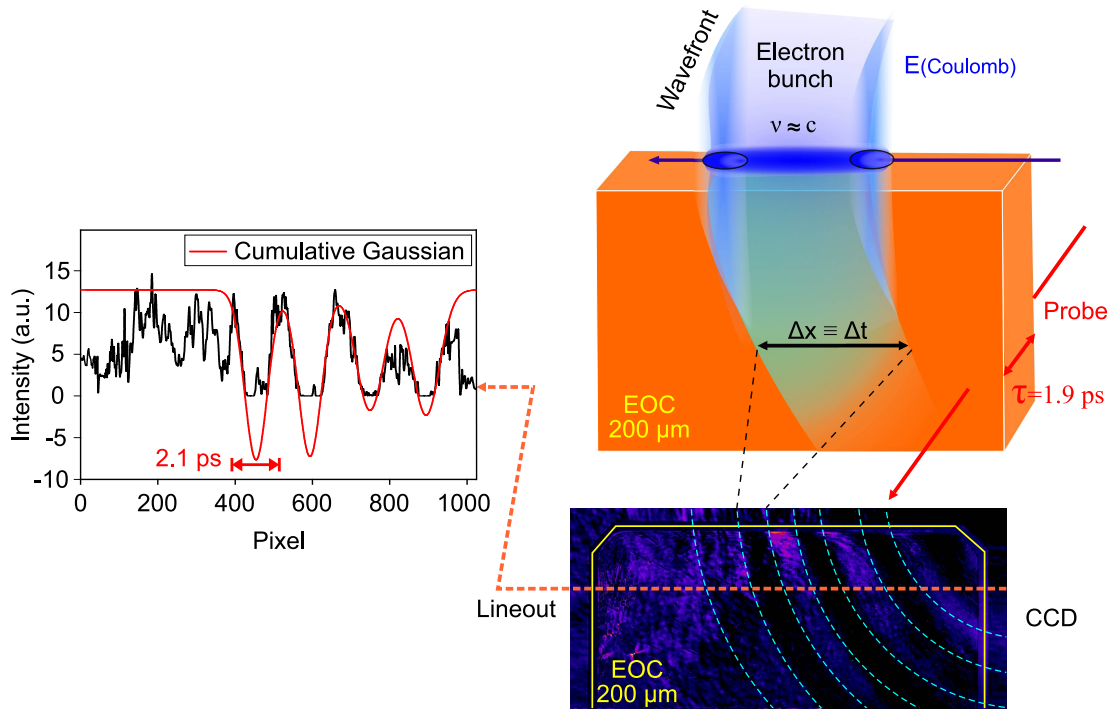


Figure 48: (Right) EO signal broadening of one electron bunch propagating at relativistic speed during the exposure time of the laser probe through the thickness of the crystal. (Left) a lineout from the EO measurement fitted with a cumulative Gaussian function to estimate the signal width.

6.3 Electron bunch length estimation

Here, we employ a distance-to-time conversion to obtain temporal information from the EO measurements. The detected signal propagates for a distance Δx on the crystal when adding a delay of Δt . Thus, we can convert the travel distance on the horizontal axis of the image to a temporal value and, hence, perform a spatiotemporal conversion. The fact that the probe is orthogonal enables a true one-to-one projection of the signal onto the crystal, which can be employed to visualize the spatiotemporal evolution of the Coulomb spherical wavefront. Moreover, we can directly calculate the propagation velocity of the signal as $v = x/t$. The reported setup with a thinner crystal can also be used as a bunch arrival time detector.

The temporal resolution is limited by the propagation time of the laser probe through the thickness of the crystal, see Figure 48. In the case of a $200\ \mu\text{m}$ thick ZnTe crystal, the temporal resolution is $\tau_r = d(200\ \mu\text{m})/c \cdot n(2.85) = 1.9\ \text{ps}$. This implies that the probe's response to the birefringence induced by the bunch's Coulomb field will be integrated over the entire time it takes for the probe to propagate through

6 DIRECT VISUALIZATION OF COULOMB FIELD OF RELATIVISTIC ELECTRON BUNCHES FROM LASER-PLASMA INTERACTION

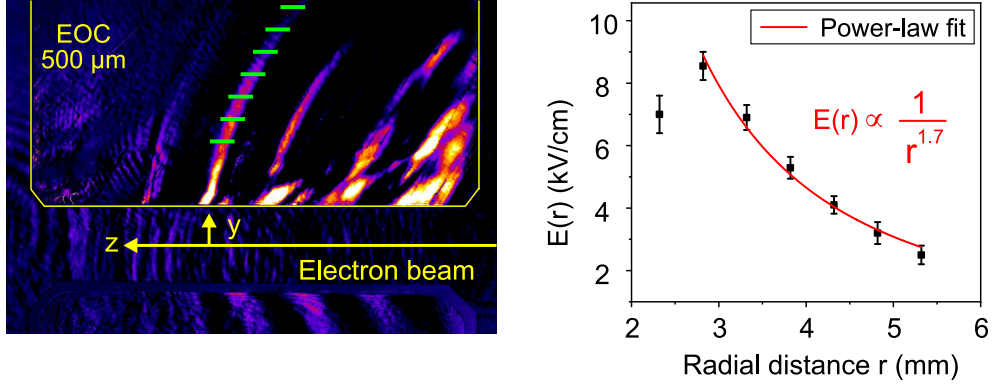


Figure 49: (Left) EO signal from the 500 μm EO crystal shown in Figure 47. Green lines mark the locations where the electric field is measured. (Right) The dependence of the electric field on the radial distance.

the crystal's thickness, which means that the minimum signal width obtained for a bunch propagating at near the speed of light will be comparable to the spatiotemporal resolution of the crystal, which in our case is 1.9 ps.

To estimate the longitudinal size of the electron bunch σ_z , a Gaussian function is employed on the EO signal obtained from the 200 μm crystal, as depicted in Figure 48. We find the signal width of the first bunch to be 58.8 ± 0.8 pixels, which is equivalent to 2.1 ps after applying the spatiotemporal transformation of 35.8 fs/pixel. We consider the measured signal to be the convolution of the bunch's longitudinal size with a Gaussian charge distribution and the probe inside the crystal with a tophat-like distribution with a width of 1.9 ps. The deconvoluted bunch length is estimated to be around 1.1 ps at a propagation distance of 12 mm. The long bunch width can be attributed to velocity dispersion, which will be discussed further later. We note that this model neglects the transverse charge distributions of the bunch, which can be addressed in future work.

6.4 Electric field dependence on radial distance

In the cross-polarization setup employed here and as derived in theory, the detected signal $I_{\text{EO}} \propto \sin^2(\Gamma/2) \propto E_{\text{THz}}^2$, and thus for small phase retardation $\Gamma \propto E_{\text{THz}}$. We estimate the electric field strength from the EO measurements using the 500 μm EO crystal at various radial distances away from the propagation axis and plot the results in Figure 49. We find that the electric field decreases inversely with radial distance as $E(r) \propto r^{-1.7 \pm 0.2}$, which is not far from the Coulomb field dependence. However, we can consider that the radiation field consists of two terms [109, 121, 122], 1-the near

field, which decreases as the square of the distance ($\propto r^{-2}$) following the Coulomb field for a particle at rest, and 2-the far field, which scales as the inverse of the distance ($\propto r^{-1}$) for accelerated charges. This suggests a dependence on the detector location as to which field term becomes dominant. It is worth mentioning that we neglect the EO signal near the edge of the crystal close to the beam axis, as it can be affected by the diffraction effect of electrons on the crystal.

Electro-optic detection using a 500 μm EO crystal

In the following, we perform a longer delay scan to demonstrate the full temporal structure of the emission. We performed the delay scan using a single 500 μm thick EO ZnTe crystal placed in the same holder behind and along the target normal. We chose the thick crystal due to its higher signal outcome despite the lower temporal resolution. The vertical edge of the crystal is 5.65 ± 0.046 mm away from the interaction point, and its upper edge is lowered by 0.5 mm from the beam line defined by the aperture. We varied the probe delay and recorded the EO signal accordingly, then blocked the pump for each delay to obtain a signal-free image as background, which was subtracted from the signal image. However, an all-zero background was not possible due to incomplete extinction and pointing instabilities. Figure 50 displays the results, indicating that the emission of relativistic electrons exhibits a periodic temporal structure spanning several tens of picoseconds. This resemblance to the previous scan can be explained by velocity dispersion, as we will discuss later. Furthermore, Figure 51 presents a close comparison of the EO signal at various consecutive delays. We note that there are 6 to 7 main curves with various intensities at nearly equal spacing. The 4th line in the middle of the emission has the highest intensity, which rules out the possibility of internal reflection inside the EO crystal. Moreover, 3 distinct straight diagonal lines can be seen in the middle of the emission. All detected signals propagate across the crystal at nearly the speed of light $v \approx c_0$.

A noticeable feature is the fine structure in the EO signal, which appears as thin lines between the main stripes. The correlation between the measured electro-optic traces and the THz pulse is affected by the strong coupling of the THz light to the TO-phonon resonance around 5.3 THz for ZnTe. This is described in 2.2.4.1, causing the frequency components of the THz pulse to propagate as a dispersive wave packet. As a result, a THz pulse appears as a main peak followed by an oscillatory tail, which is detected as thin lines [123].

6 DIRECT VISUALIZATION OF COULOMB FIELD OF RELATIVISTIC ELECTRON BUNCHES FROM LASER-PLASMA INTERACTION

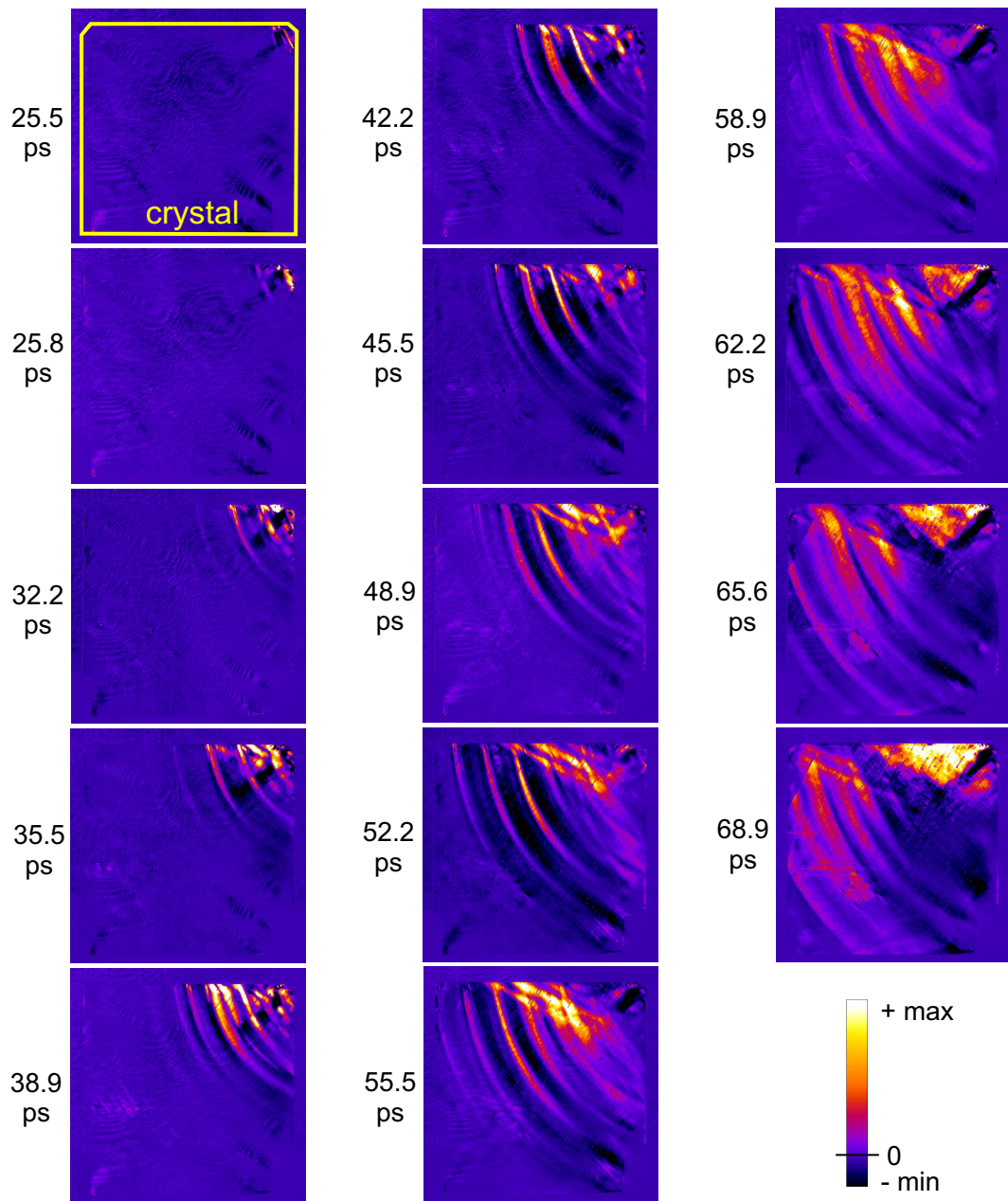


Figure 50: Spatiotemporal evolution of the spherical wavefront of the Coulomb fields of relativistic electron bunches emitted during the interaction with ultrashort high-intensity laser pulses. The first image in the upper left panel shows the outer edge of the electro-optic crystal in yellow. The signal appears from the right side of the crystal in each frame. All images are background subtracted.

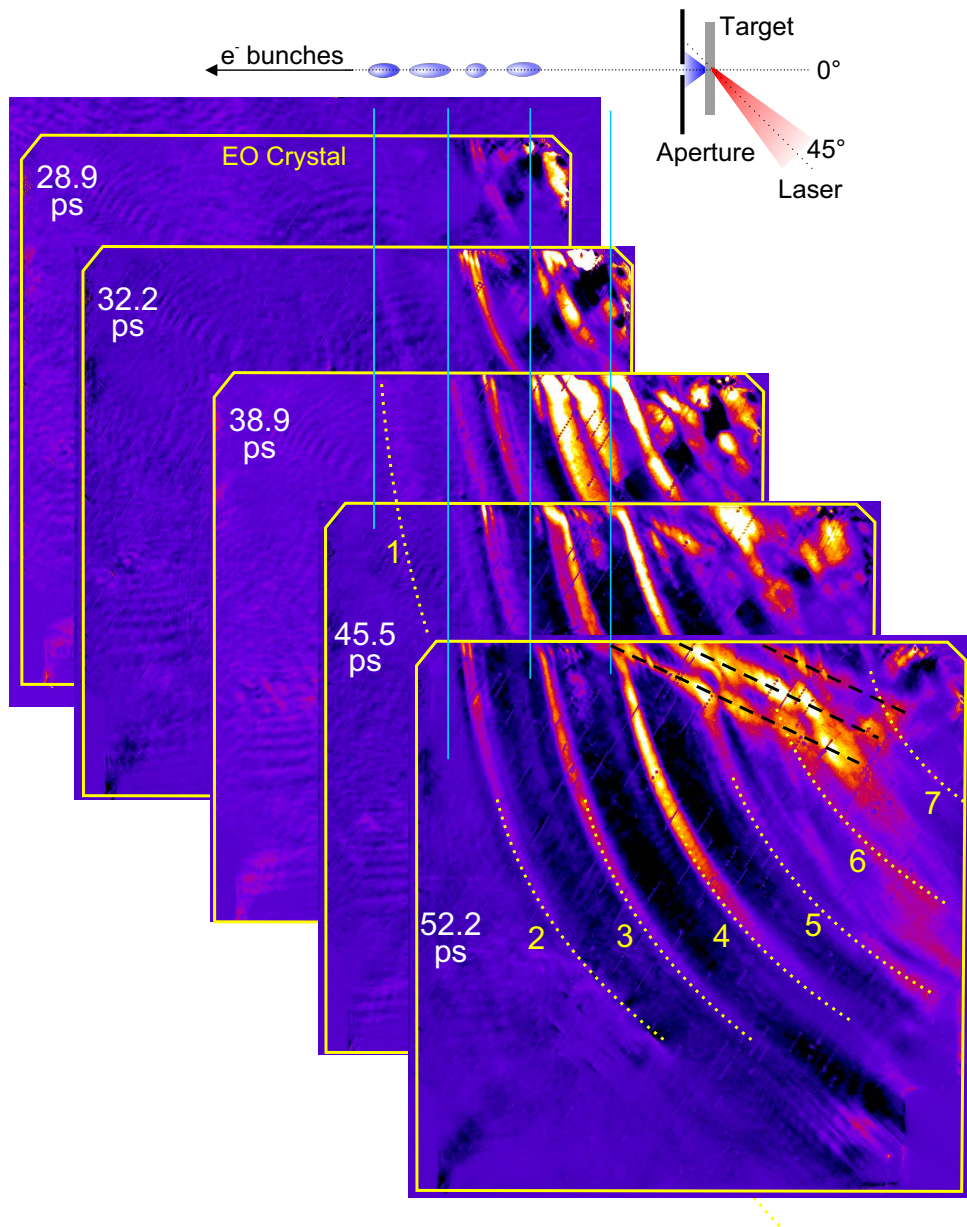


Figure 51: A comparison of the EO signal at successive delays shows a well-defined periodic structure at nearly equal intervals (dotted curves), in addition to three diagonal lines (dashed black). Vertical lines in cyan mark similar EO features on the crystal as the EO signal propagates to the left with time. The yellow box defines the EO crystal.

6.5 Testing signal origin

Since the interaction studied in this experiment emit not only energetic electrons but also THz radiation [8], both of which are detectable in our setup, we need to verify the origin of the detected EO signal. As thoroughly investigated in the previous sections,

6 DIRECT VISUALIZATION OF COULOMB FIELD OF RELATIVISTIC ELECTRON BUNCHES FROM LASER-PLASMA INTERACTION

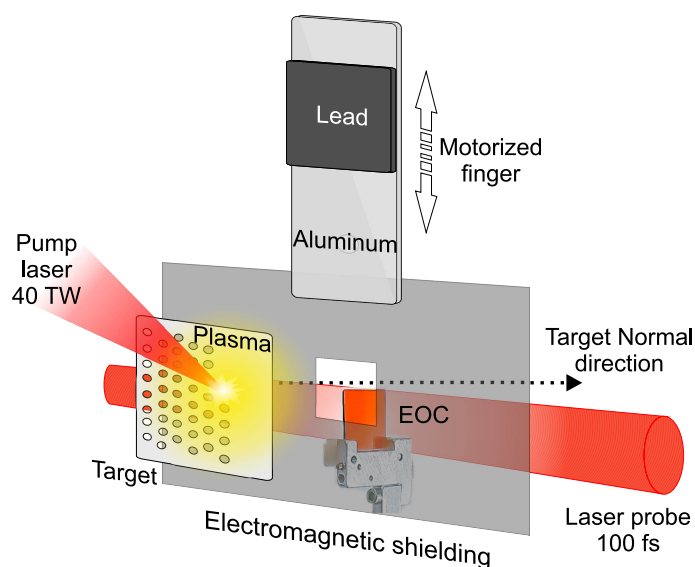


Figure 52: The shielding is arranged as seen in the free-propagation mode and consists of a fixed 1 mm aluminum sheet with a 5 mm window to isolate the EO diagnostics from reflected THz radiation. A motorized shield plate can be lowered with three interchangeable areas: a 1 mm hole, an aluminum plate of 1 mm thickness, and an additional 2 mm thick lead plate on top.

the THz emission has a characteristic temporal structure with a few THz pulses with comparable pulse durations at sub-picosecond times and close temporal delays. The emission occurs mainly in the non-collinear direction around the target normal [80]. Moreover, we also need to estimate the kinetic energy of the electrons separately, since a small uncertainty in the measured velocity near the relativistic limit leads to a large difference in the kinetic energy.

In principle, we completely shield the electro-optic detection setup from the interaction region by employing a 1 mm thick black anodized aluminum sheet to block the noncollinear THz radiation. The sheet has a 5 mm square window cut as seen in Figure 52. The window provides an acceptance angle of about $\pm 41^\circ$. This has been demonstrated experimentally to protect against reflected electromagnetic radiation that would otherwise be detectable. Figure 53 shows the acquired electro-optic signal taken at a longer delay with and without the added shielding.

In addition, we add a motorized aluminum plate of thickness 1 mm partially covered by an additional 2 mm of lead, as shown in Figure 52. The plate position can be controlled to constrain the pathway between the interaction point and the EO crystal in three distinct modes, as seen in Figure Figure 54. The implications of this approach allow us to block THz radiation and energetic electrons in a systematic way. We present

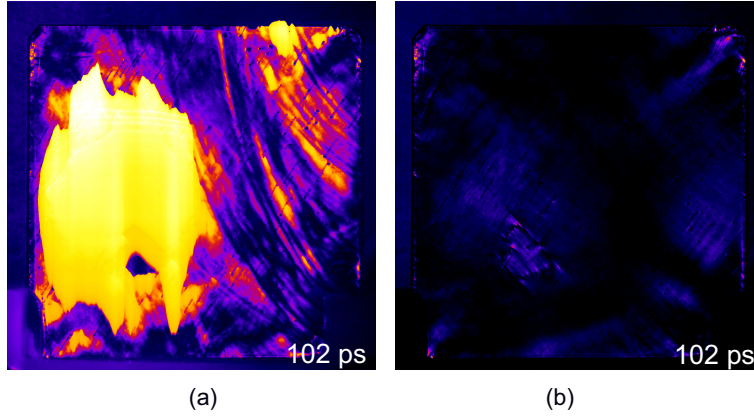


Figure 53: (a) Detected EO signal at a longer delay without complete shielding during the optimization of the experiment. (b) the same acquisition shows zero signal or leakage after adding an aluminum sheet around the EO crystal as illustrated in Figure 52.

the results in Figure 54, where the left column shows the detected EO signal with no restriction between the interaction region and the EO crystal. We note that the EO signal saturates but still shows a similar periodic structure propagating at near-light speed $v \simeq c$.

Next, we introduce a 1 mm thick aluminum plate in the pathway to the EO crystal to fully shield it from THz radiation from the interaction. However, the energy of the electron bunches passing through the metallic plate decreases due to the collisional energy transfer to bound atomic electrons in the material following the “Bethe” theory [102]. The stopping power of 1 mm of aluminum can be estimated using the continuous-slowing-down approximation range (CSDA), which, according to the NIST database, is about 0.57 MeV [124]. The results are presented in the middle column of Figure 54, where the EO signal becomes weaker compared to the free propagation case. Direct THz pulses could not reach the crystal due to the blockage. On the other hand, the recorded energetic electrons near the high energy cutoff in Figure 23 can still penetrate the blocking material, which could explain the detected EO signal.

Evident features in the EO signal rise when blocking the propagation path with a combination of 1 mm aluminum and 2 mm lead plates. The equivalent stopping power is $2.7 \text{ MeV (Pb)} + 0.57 \text{ MeV (Al)} = 3.27 \pm 0.32 \text{ MeV}$. The results are shown in the right column of Figure 54. We note a particularly broad signal extending in time, which may originate from the dispersion of the kinetic energy of the electrons due to their propagation through the blocking material. Since the energy loss depends on the kinetic energy of the electrons [125], the energy dispersion increases, that is,

6 DIRECT VISUALIZATION OF COULOMB FIELD OF RELATIVISTIC ELECTRON BUNCHES FROM LASER-PLASMA INTERACTION

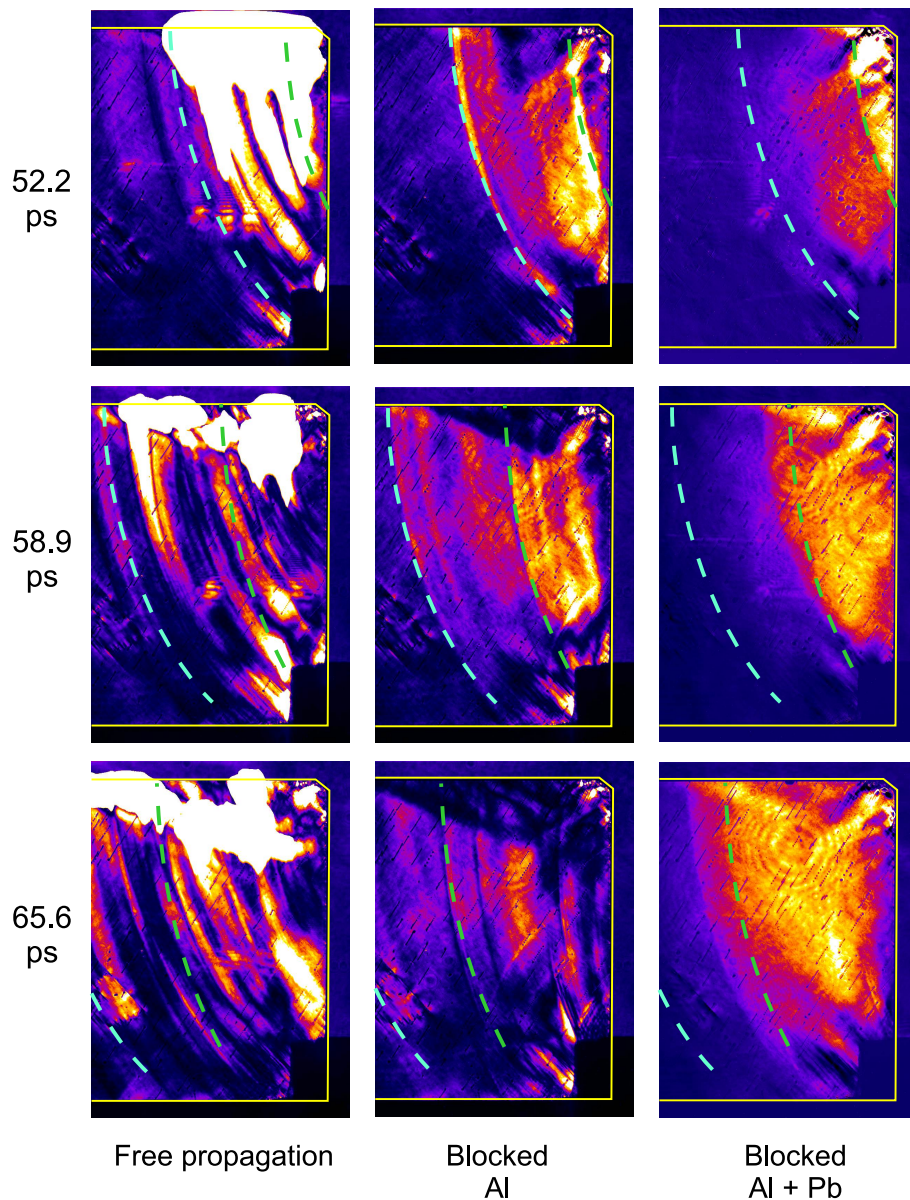


Figure 54: Detected EO signals under distinct propagation conditions between the interaction region and the EO crystal; (left column) free propagation, (middle column) complete blockage by an aluminum plate with a thickness of 1 mm. (Right column) complete blockage by 1 mm of aluminum and 2 mm of lead. Dashed lines mark the position of selected signals to help guide the eye across each delay. The white region in the left column is due to signal saturation.

the difference between the fastest and slowest electrons. This results in an elongated electron cloud emerging behind the blocking material. In this way, the accompanying Coulomb field is elongated longitudinally.

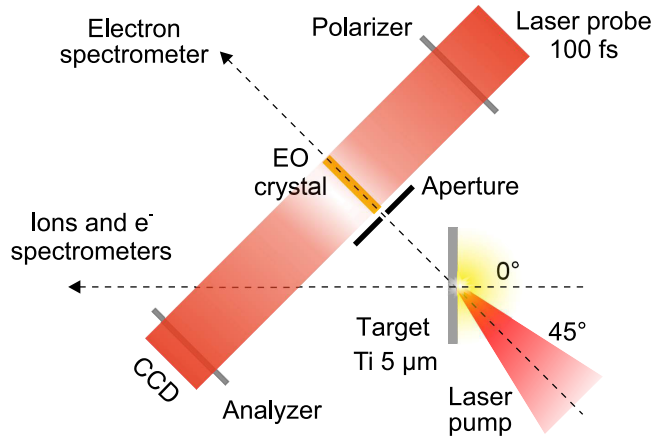


Figure 55: A simplified schematic of the setup for detecting transient emission in the direction of laser propagation. A $200\ \mu\text{m}$ ZnTe crystal is placed at a distance of $13.5\ \text{mm}$ at 45° with respect to the target normal. The EO crystal is protected by a $1\ \text{mm}$ aluminum aperture. The detection scheme is similar to the one presented previously in Figure 45.

6.6 Observations in the direction of laser propagation

In this experiment, we aim to investigate the spatiotemporal structure of the relativistic electron emission along the direction of laser propagation and compare it to observations along the target normal. The EO crystal is placed $13.5\ \text{mm}$ away from the interaction point and along the laser propagation direction at 45° , see Figure 55. The crystal has a thickness of $200\ \mu\text{m}$, compared to $500\ \mu\text{m}$ in the case of the observations along the target normal direction (0°). Here we used a titanium target with a thickness of $5\ \mu\text{m}$. We present the detected EO signal in Figure 56. We report on the detection of spherical wavefronts of Coulomb fields accompanying electron bunches emitted along the laser propagation direction. When varying the probe delay, all detected wavefronts propagate at nearly the speed of light in the vacuum $v \approx c$ with radii equal to the exact distance to the target. Moreover, the detected EO signal extends for $\sim 20\ \text{ps}$ due to velocity dispersion after a propagation distance starting from $13.5\ \text{mm}$ to $23.5\ \text{mm}$. Due to the larger propagation distance, the radius of curvature of the wavefronts presented here is considerably larger than that previously detected at $5.65\ \text{mm}$ in Figure 50. Although the two observations differ in showing distinct propagation directions, 0° and 45° , the spatiotemporal evolution of the spherical wavefronts of the Coulomb fields is nevertheless evident. To the best of our knowledge, this is the first experimentally obtained visualization of the wavefronts of Coulomb fields emitted from relativistic electron bunches during an intense laser-solid interaction.

6 DIRECT VISUALIZATION OF COULOMB FIELD OF RELATIVISTIC ELECTRON BUNCHES FROM LASER-PLASMA INTERACTION

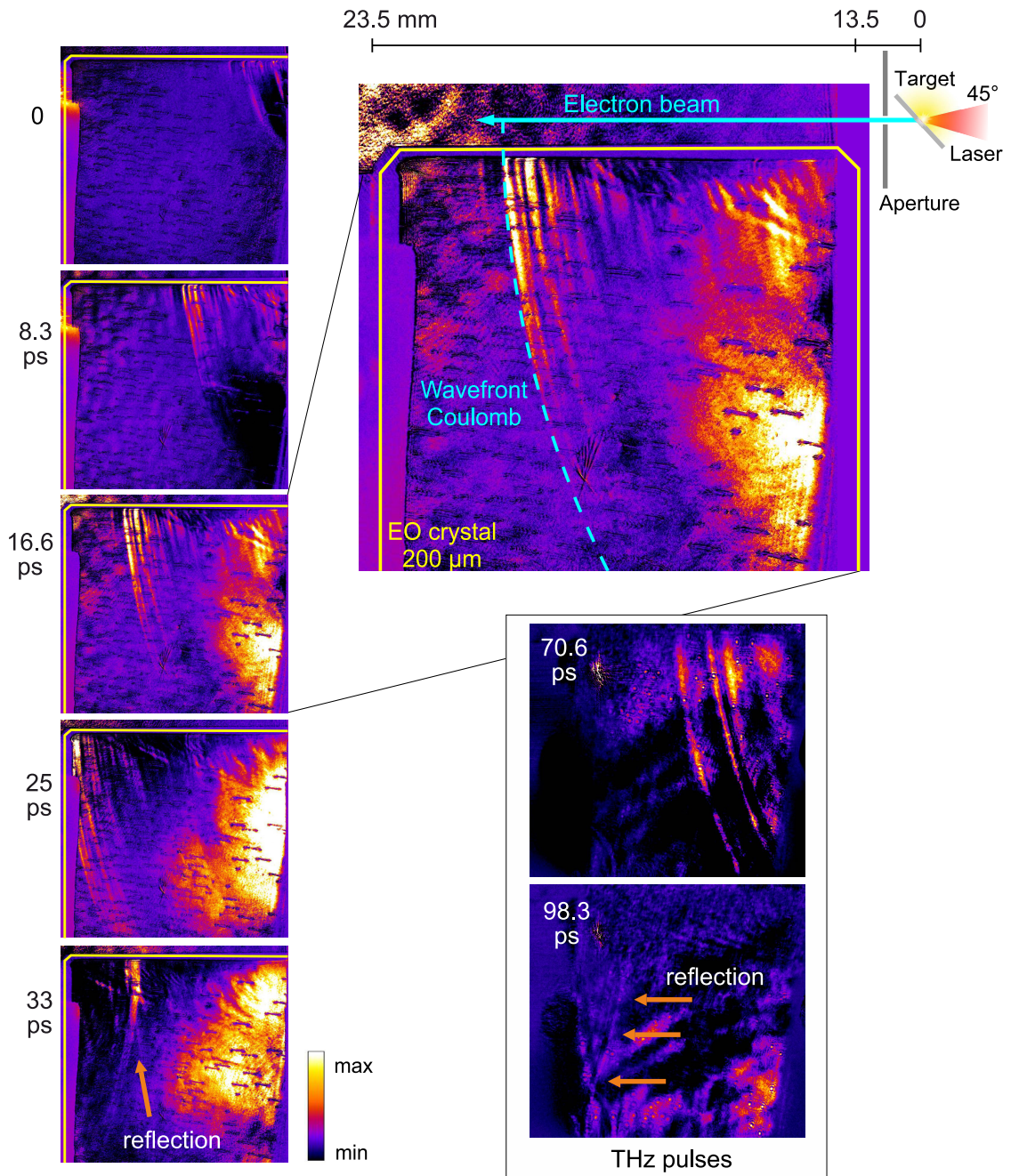


Figure 56: Observations of spherical wavefronts of Coulomb fields accompanying relativistic electron bunches emitted along the laser propagation direction during the laser-plasma interaction. The EO detection takes place 13 mm away from the target. All observed spherical wavefronts have radii equal to the distance to the interaction point. The dashed cyan indicates a circle with its center at the interaction point. Inset shows the detected THz pulses and their reflection at the crystal edge at longer delays.

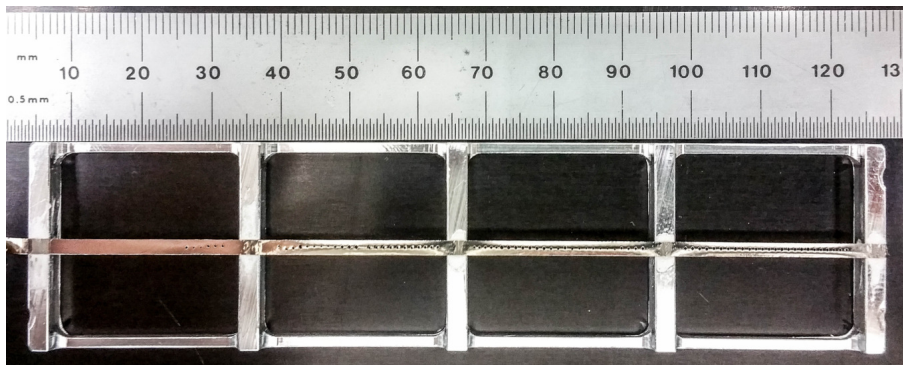


Figure 57: A long strip of Titanium with a thickness of $5\ \mu\text{m}$ was used as a target in the plasma shadowgraphy experiments.

We also report on the detection of THz pulses at longer delay values, see inset of Figure 56. 3 THz pulses were detected with a time delay of around $70\ \text{ps}$ from the first observation at $0\ \text{ps}$. The difference in the EO signal induced by the THz pulses and the electron bunches is an indication of the origin of the signal for both cases. As for the THz pulses, the signal appears as 3 long curves with homogeneous intensities across the entire length of the crystal. The number of pulses reported here matches the 3 identified THz pulses from the EO measurements in Chapter 3 in Figure 14. On the other hand, the EO signal of electron bunches decreases exponentially away from the electron propagation axis, as was shown previously in Figure 49. This comparison further suggests that the presented signal is indeed caused by relativistic electron bunches.

6.7 Time evolution via plasmashadowgraphy

The intensity-temporal profile of the laser has a typical nanosecond-long ASE pedestal with pre-pulses 10s of picoseconds before the main peak, see Figure 11. Given the moderate contrast of the laser, heating and, consequently, ionization of the target is expected to form a pre-plasma before the arrival of the main laser peak. The acceleration of electrons on the irradiated side of the target is governed by the interaction parameters including the conditions of the pre-plasma. However, charge-particle dynamics on the rear side of the target may also give rise to modulated electron emission. One possible mechanism is related to the reflection, deceleration, and acceleration of laser-driven hot electrons by the target-rear sheath electric field [126], which implies a long sheath evolution at the target rear surface. An additional contribution can be the recirculation of hot electrons on the target back surface [127]. Both possibilities

6 DIRECT VISUALIZATION OF COULOMB FIELD OF RELATIVISTIC ELECTRON BUNCHES FROM LASER-PLASMA INTERACTION

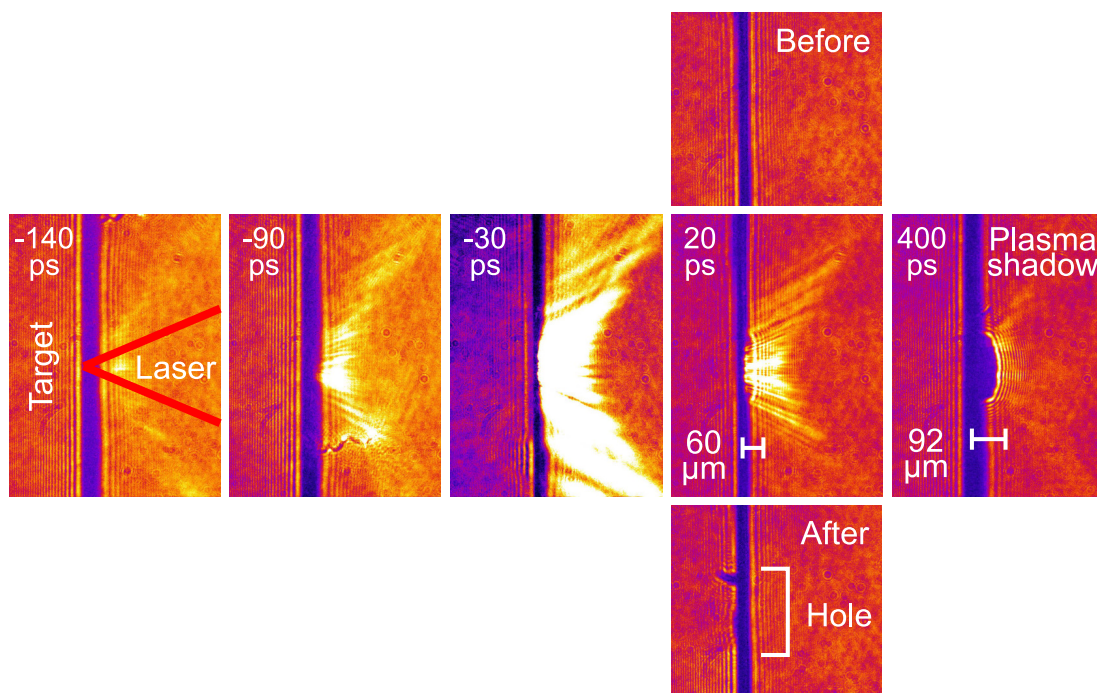


Figure 58: Plasma shadowgraphs show the expansion of the plasma on the irradiated side of the target at various time delays. Laser incident from the right. Images in the top and bottom rows show the target before and after the interaction.

require that the target back surface remains intact over the timescale of the emission, so as not to be perturbed by the expanding plasma on the front side.

We attempt to obtain the time evolution of the plasma expansion using a dedicated time-synchronized probe beam via plasma shadowgraphy, while simultaneously detecting the long-lasting emission, all acquired in a single shot. We set the arrival time of the main laser pulse at the interaction point as time zero by observing the plasma shadowgraph in air at reduced energy. The setup is schematically depicted in Figure 44. The image of the interaction plane is relayed outside the chamber to a CCD camera with a magnification of around 10x to achieve a resolution of about $1.2 \mu\text{m}/\text{pixel}$. The target is a hand-cut strip of titanium with a width of $\sim 2 \text{ mm}$ and a thickness of $\sim 5 \mu\text{m}$, see Figure 57. This layout was chosen as a compromise between mechanical stability and obtaining the thinnest target shadow on the camera.

During the experiment, we varied the time delay of the probe beam with respect to the main beam between -200 ps and $+500 \text{ ps}$. In addition, we imaged the target prior to each shot while blocking the main beam and used it for reference. A selection of images obtained from the shadowgraph scan is shown in Figure 58. The laser beam comes from the right. We can see a plasma shadow expanding hydrodynamically into

the vacuum on the irradiated side of the target, while the rear side remains intact through the whole scan i.e. well beyond the time span of the observed THz and electron emission. A pre-plasma is expected to develop before the main pulse due to the amplified spontaneous emission (ASE) and pre-pulses in the laser temporal profile, however, the expected size of such a pre-plasma is smaller than $40 \mu\text{m}$ [128] and thus can be obscured by the shadow from the curvature of the target and the limited resolution of the imaging system. The plasma expansion velocity after the main pulse can be calculated as $(60 - 92) \mu\text{m}/380 \text{ps} = 8.4 \times 10^4 \text{m/s}$ in good agreement with [129, 130].

6.8 Discussion

The electric field of an electron bunch can be roughly estimated as a convolution $E_{\text{THz}} = (E * Q)(r, t)$ [57, 120], where

$$E(t) = \frac{N e}{4\pi\epsilon_0} \frac{\gamma r}{(r^2 + \gamma^2 v^2 t^2)^{3/2}} \quad , \quad Q(t) = \frac{1}{\sqrt{2\pi\sigma^2}} \exp\left(\frac{-t^2}{2\sigma^2}\right) \quad (89)$$

here $E(t)$ is the radial electric field of N electrons at distance r , v is the electron velocity, and $Q(t)$ is the temporal distribution of the electron bunch assuming a Gaussian profile. We can estimate the number of electrons in a bunch by providing the energy and electric field. We have a good estimate of the average kinetic energy of the electrons from the stopping power of the material used to block them from 6.5. Using a stopping power of 3.27MeV leads to a strong broadening of the EO signal but not a complete stopping, see Figure 54. Furthermore, we measured the electric field of the leading bunch in Figure 49 to be around 8.8kV/cm . We thus estimate the number of electrons in the bunch to be on the order of 7.3×10^8 electrons which is equivalent to a charge of $\sim 100 \text{pC}$. This is in good agreement with the values found in the integrated energy spectra shown in Figure 23, obtained with a calibrated energy spectrometer.

An evident feature arises when comparing the periodicity of the bunches at 45° , shown in Figure 56, and at 0° , shown in Figure 47. We note that the number of lines in the emission at 45° appears to be higher than at 0° . This could originate from the oscillatory component that accelerates the electrons for a given heating mechanism. For example, energetic electrons are accelerated along the laser propagation direction mainly via $j \times B$ acceleration following the frequency of the oscillating ponderomotive force, $2\omega_0$ [91, 131]. This means that twice every laser cycle, a group of electrons will be

accelerated into the plasma by the ponderomotive force. On the other hand, resonance and vacuum heatings accelerate the electrons at a full cycle along the target normal direction. Although the timescale of the laser cycle is of the order of a few femtoseconds and the laser main peak is around 32 fs, we need to take into account the broadening in the electron emission due to energy dispersion while propagating through the target. Additionally, the temporally extended EO signal presented here can be explained by the velocity dispersion of the ejected electrons. For example, using $\Delta t = \frac{\text{distance}}{c}(1/\beta_1 - 1/\beta_2)$, where β_1 and β_2 represent the reduced velocity of the slowest and fastest electrons in a bunch, respectively, the temporal broadening of electrons with energies between 0.511 MeV and 4 MeV, starting at the interaction point at $t = 0$, would be approximately 5.5 ps and 12 ps. This broadening occurs after propagating distances of 16 mm at 0° and 23 mm at 45° . More broadening is expected when considering the temporal intensity profile of the laser [128]. The detected EO signal indeed extends longer in time at 45° compared to the 0° case due to the longer propagation distance at which the crystal is placed. In addition, the separation between electron bunches can be affected by wave breaking dynamics inside the plasma, which reduces the correlation with the laser period [132]. Many groups have presented simulations of laser-thin target/plasma interactions showing accelerated electrons as "trains" of high-energy electrons [133–135], however, to the best of our knowledge, this is the first experimentally obtained temporal profile of electron bunches emitted during laser-thin solid interaction. Moreover, our measurements show a difference in the periodicity of the temporal profile of the electron emission between 0° and 45° due to various acceleration mechanisms.

Our EO measurements show the evolution of the spherical wavefronts observed in a single-shot at a distance of D after the electron beam has passed through the aluminum target. Due to the orthogonal probing of the laser onto the EO crystal, the spatiotemporal profiles can be regarded as snapshots in space, which serves as a proof-of-concept. Despite the limited temporal resolution, the observations confirm that the spherical curvature of the electric field wavefront becomes smaller with increasing propagation distance, as seen from $D = 6$ mm to 16 mm at 0° in Figure 47, and from $D = 13.5$ mm to 23.5 mm at 45° in Figure 56. This validates the approximation of considering the wavefront as a flat plane near the beam axis at a long propagation distance, as can be seen in Figure 56, where the wavefront reaches 23.5 mm on the left side of the EO crystal.

7 Summery

The work contained within this thesis explores two major themes: the intense THz emission and the temporal structure of relativistic electron bunches both emitted from the rear surface of thin metallic foils during the interaction with intense ultrashort laser pulses. The comprehensive characterizations provided in Chapter 3 demonstrate the emission of radially polarized intense terahertz pulses with record-breaking field strength reaching $\sim 3 \text{ MV/cm}$ at the focus [11]. The temporal structure of the THz emission exhibits short, multiple pulses of a few hundred femtosecond duration lasting for several picoseconds in both noncollinear and forward emission geometries. Moreover, the constructed 3D angular distribution reveals the dominance of THz emission at large angles relative to the target's normal direction for oblique laser incidence. A prominent application of intense sub-picosecond THz pulses is the post-acceleration [136] and steering [137] of electron bunches.

To define the correlation between the detected subpicosecond emission and the charged particle dynamics during the interaction, we conducted an in-depth characterization of the particle emission in Chapter 4. Our analysis included the angular distribution of hot electrons exiting the target, revealing the presence of two distinct electron heating mechanisms with various temperatures: resonant absorption at 0° and ponderomotive heating at 45° . Additionally, we provided precise energy-resolved measurements and explored the influence of various laser parameters on the properties of laser-accelerated electrons and protons. This parametric study offers valuable insights into the relativistic laser-matter interaction within thin targets.

In Chapter 5, we present a detailed numerical investigation supported by experimentally measured THz and charged particle emission. We defined two dominant physical processes that could be responsible for the emission of THz radiation. 1- coherent transition radiation (CTR) by the energetic electrons exiting the target. We observed that the CTR emission from accelerated electron bunches in the direction of the laser propagation (45°) is an order of magnitude higher than that from electrons emitted in the target normal (0°). This discrepancy is due to the energy dependence of CTR. In addition, the emission is inhomogeneous and inclined at wider angles, with a spectral range between 0.1 and 1.5 THz. 2- plasma sheath radiation (SR) due to the transient dynamics of the expanding plasma sheath formed at the back surface of the target in the TNSA mechanism. The SR radiation is predominantly emitted non-collinearly away from the target normal, with a spectrum mostly below 2 THz. Comparing the nu-

merical models of CTR and SR radiation with the experimental data revealed excellent agreement in both angular and energy profiles. This validation further supports our understanding of the mechanisms driving the THz radiation emission from thin metallic foils during intense laser interactions. Ultimately, we applied the treatment established in our numerical model to estimate the expected longitudinal duration of fast electron bunches from the measured CTR spectrum. Our analysis revealed that the spatial length of the electron bunches exiting the target is approximately $41 - 61 \mu\text{m}$, which corresponds to a temporal length of $133 - 200 \text{ fs}$ for relativistic electrons. Comparing these values with those obtained from the hot electron spectra, we found a reasonable agreement, supporting the reliability and utility of non-invasive THz-based diagnostics in characterizing the electron bunch dynamics during laser-matter interaction. These insights contribute significantly to the field, paving the way for optimized applications and advancements in the generation and utilization of THz radiation.

Finally, driven by the demand for accurate time-resolved characterization of charged dynamics during intense laser-matter interactions, our work achieved a significant milestone: the first direct observation of Coulomb fields' wavefronts accompanying relativistic electron bunches emitted during the interaction of an intense laser pulse with a thin metallic foil on a sub-picosecond timescale. Ultrafast direct visualization of relativistic electron bunches has been made possible by employing a non-destructive single-shot electro-optic detection system. We experimentally demonstrated the contraction of the electric field of relativistic electron bunches under the Lorentz transformation. The visualized spatiotemporal electric field profile confirms the description of Liénard-Wiechert potential for the Coulomb field: the electromagnetic waves emitted from a relativistic electron are integrated over the propagation direction, forming a spherical wavefront with a radius identical to the propagation distance. Furthermore, we validated the spatiotemporal evolution of the spherical wavefronts by monitoring the change in curvature as the electron bunches propagated away from the target. As the electron bunches exit the rear surface of the target, the Coulomb field distribution extends with wavefronts expanding as spherical waves from the plasma-vacuum interface due to the loss of quasi-neutrality inside the plasma/target. The time-resolved measurements revealed a complex temporal structure with multiple electron bunches. Our proof-of-concept experiment opens the possibility of practical applications in measuring fast dynamics of electrons and positrons [138] and in the research on electric fields described by the general Liénard-Wiechert potentials.

8 Appendix

A. Normalized eigenvectors

$$\begin{aligned} \mathbf{U}_1 &= \frac{1}{2} \sqrt{1 + \frac{\sin \alpha}{\sqrt{1 + 3 \cos^2 \alpha}}} \begin{pmatrix} -1 \\ 1 \\ \frac{2\sqrt{2} \cos \alpha}{\sqrt{1+3 \cos^2 \alpha} + \sin \alpha} \end{pmatrix} \\ \mathbf{U}_2 &= \frac{1}{2} \sqrt{1 - \frac{\sin \alpha}{\sqrt{1 + 3 \cos^2 \alpha}}} \begin{pmatrix} 1 \\ -1 \\ \frac{2\sqrt{2} \cos \alpha}{\sqrt{1+3 \cos^2 \alpha} - \sin \alpha} \end{pmatrix} \\ \mathbf{U}_3 &= \frac{1}{\sqrt{2}} \begin{pmatrix} -1 \\ -1 \\ 0 \end{pmatrix} \end{aligned} \quad (90)$$

B. The high power laser system Jeti 40

The Jeti-40 laser is a table-top multi Terawatt Titanium:Sapphire system operating based on the chirped pulse amplification scheme (CPA) [1]. The system is able to deliver pulses with a maximum pulse energy of 1.2 J at a repetition rate of 10 Hz at a central wavelength of 800 nm with a minimum duration of 32 fs. This leads to intensities exceeding 10^{19} W/cm^2 .

The laser system presented in Figure 59 uses titanium-doped sapphire crystals (Ti:Sa) as an active medium for all amplification stages. The pulses start by a femtosecond oscillator at a central wavelength of 800 nm with energy of about several nanojoules and duration of 45 fs. The pulses are then amplified in the Booster up to microjoules and a pockels cell based pulse picker reduces the repetition rate to 10 Hz. Afterwards the pulses pass the stretcher where they get positively chirped which extends the pulse duration to about 150 ps. This is crucial to prevent non-linear effects such as pulse filamentation and to protect all the following optics from high intensities along various amplification stages. Next, the stretched pulses are guided into three Ti:Sapphire amplifiers pumped by frequency doubled Nd:YAG (Neodymium:Yttrium-Aluminum-Garnet) lasers. These are in sequence: a regenerative amplifier with an outcome of millijoules followed by two free running multipass amplifiers which brings the pulse energy up to few 100s of mJ and later to about 1 Joule level. An additional (1:5) magnification telescope is used to further reducing the intensity. Finally, the fully

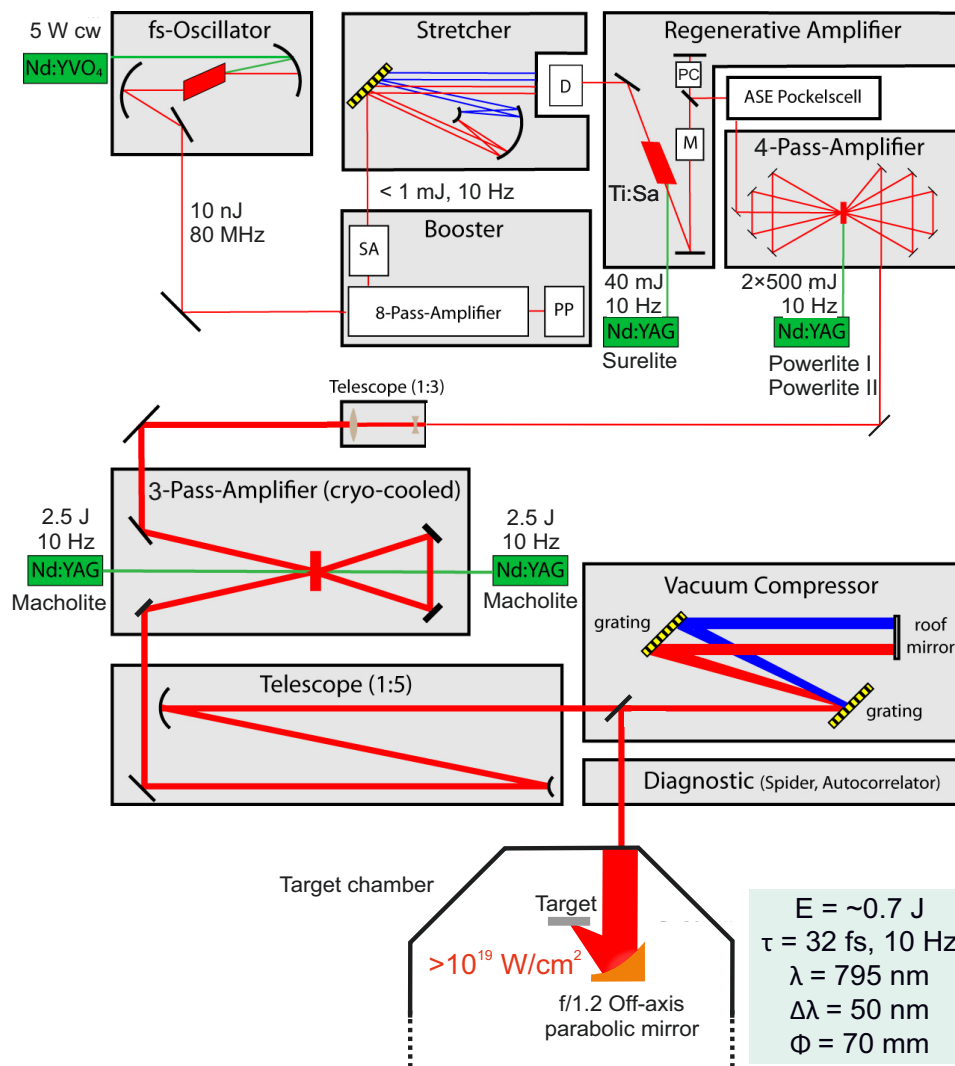


Figure 59: schematic layout of the Jeti laser: a table-top high-intensity laser that uses chirped pulse amplification (CPA). It consists of a short pulse oscillator, a stretcher, three amplification stages, and a vacuum compressor to deliver pulses of 0.7 J of energy on target within 32 fs at a central wavelength of 800 nm. The laser is guided under vacuum to the target chamber and by employing an f/1.2 focusing off-axis parabolic mirror intensities higher than $> 10^{19} \text{ W/cm}^2$ on a target can be achieved. SA: saturable absorber, PP: pulse picker, D: Dazzler, M: Mazzler, PC: Pockels cell.

amplified pulses are re-compressed under vacuum using a double-grating with a double pass compressor down to a FWHM pulse duration of 32 fs. The outcome efficiency of the compressor is about 65% due to multi-reflection on the two gold gratings. After the regenerative amplifier a fast Pockels cell with a rise time on the order of a nanosecond is employed to suppress amplified spontaneous emission (ASE) as well as pre-pulses.

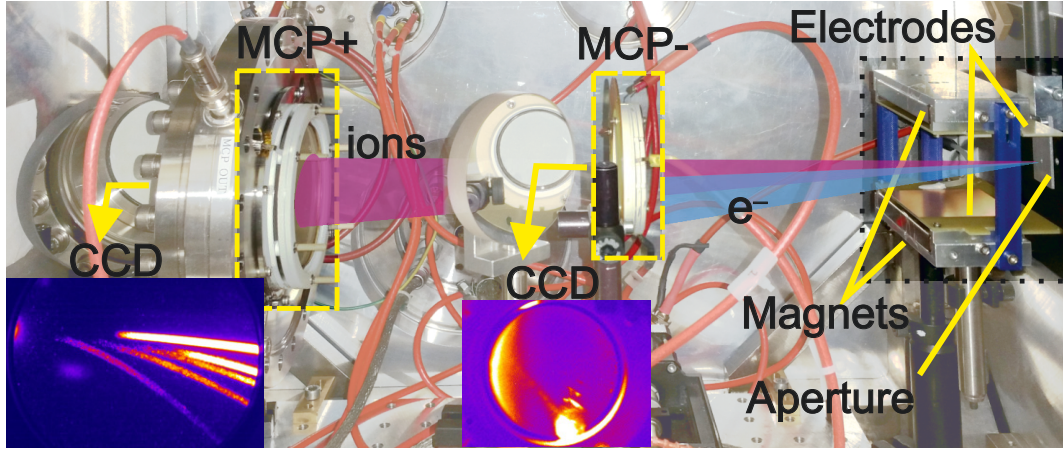


Figure 60: Thomson parabola spectrometer for the detection of protons and ions during high intensity laser-plasma interactions. It consists of two parallel electric and magnetic fields which deflect the accelerated charged particles according to their q/m . After exiting the deflection fields, protons and ions drift for 31 cm to hit a multi-channel plate (MCP+) detector with a phosphor screen, such that the impact position and intensity can be imaged using a CCD. (MCP-) was used to detect electrons and negative ions (not presented in this work).

C. Ions Diagnostics

During the laser-target interaction, the ions are accelerated via TNSA at the rear surface and along the normal direction of the target and can be detected with an ion spectrometer. We built a special spectrometer based on a Thomson Parabola (TP) as a dispersive element and a large (70 mm) multichannel plate (MCP) with an imaging system and nuclear track plastic detectors (CR39) for MCP calibration. The spectrometer was built in a separate chamber for quick adjustment and to prevent light leakage. The TP element consists of two parallel electric and magnetic fields, both of which can be modified by varying the potential and varying the distance between the magnets, respectively. We measured a flux density of $B = 110$ mT using a Hall probe, while the electric field was fixed at 42.5 kV/m. After exiting the deflection field, the protons and ions drift for 31 cm to hit the MCP detector with a phosphor screen, such that the impact position and intensity can be imaged using a CCD. TP deflects charged particles according to their q/m , so that the energy (E) of each particle can be estimated from its deflection value as

$$x = \frac{qB}{\sqrt{2mE}} \left(\frac{1}{2}L_B^2 + L_B D_B \right) \quad (91)$$

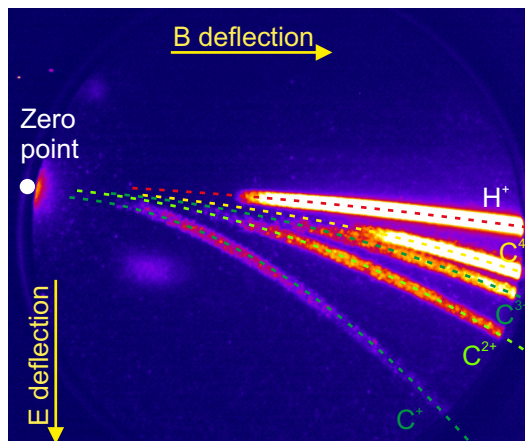


Figure 61: A typical MCP image of ion spectra recorded during the experiment. The dashed lines are simulated traces of carbon ions and protons.

where L_B is the length of the magnet along the trajectory of the particle and D_B is the distance between the end of the magnets and the MCP. The entrance of the TPS is placed 86.3 cm away from the interaction point and has a 1.35 mm hole, giving $2 \mu\text{Sr}$ as the acceptance angle.

The prominent feature of this spectrometer is the high dynamic range, as it can detect protons with energies as low as 30 keV while still detecting high energy cutoffs around 4 MeV in a single shot. The detection of low-energy protons can be a useful tool for marking the evolution of the TNSA mechanism starting from low laser intensities around $5 \times 10^{16} \text{ W/cm}^2$ [88], as will be presented later.

D. Electron Spectrometer

In this work, we attempt to provide a complete picture of electron emission during high-intensity plasma interactions. To support the temporal measurements, we also measured the energy and, sequentially, the temperature of the electrons along the normal direction of the target and the laser propagation direction using an energy spectrometer. We used calibrated electron spectrometers based on a magnetic deflection with image plates as the detection medium [139]. The angles of acceptance are 41 and $25 \mu\text{Sr}$ for the spectrometer at (0°) and (45°), respectively. Both can measure from several keV up to several tens of MeV. To record the electron spectra, several shots were averaged for each set of parameters of the interaction. The time-integrated and averaged spectra are then fitted using a Maxwellian-like distribution to estimate the temperature.

9 References

- [1] D. Strickland and G Mourou. Compression of amplified chirped optical pulses. *Optics Communications*, 56(3):219–221, 1985.
- [2] C. Danson, D. Hillier, N. Hopps, and D. Neely. Petawatt class lasers worldwide. *High power laser science and engineering*, 3:e3, 2015.
- [3] A. Pirozhkov, Y. Fukuda, M. Nishiuchi, H. Kiriyama, A. Sagisaka, et al. Approaching the diffraction-limited, bandwidth-limited petawatt. *Optics express*, 25(17):20486–20501, 2017.
- [4] K. Ledingham, I. Spencer, T. McCanny, R. Singhal, M. Santala, et al. Photonuclear physics when a multiterawatt laser pulse interacts with solid targets. *Physical Review Letters*, 84(5):899, 2000.
- [5] E. Clark, K. Krushelnick, J. Davies, M. Zepf, M. Tatarakis, et al. Measurements of energetic proton transport through magnetized plasma from intense laser interactions with solids. *Physical Review Letters*, 84(4):670, 2000.
- [6] H. Hamster, A. Sullivan, S. Gordon, and R. Falcone. Short-pulse terahertz radiation from high-intensity-laser-produced plasmas. *Physical Review E*, 49(1):671, 1994.
- [7] W. Sun, X. Wang, and Y. Zhang. Terahertz generation from laser-induced plasma. *Opto-Electronic Science*, 1(8):220003–1, 2022.
- [8] S. Herzer, A. Woldegeorgis, J. Polz, A. Reinhard, M. Almassarani, et al. An investigation on THz yield from laser-produced solid density plasmas at relativistic laser intensities. *New Journal of Physics*, 20(6):063019, jun 2018.
- [9] M. Shalaby, C. Vicario, and C. Hauri. Extreme nonlinear terahertz electro-optics in diamond for ultrafast pulse switching. *APL Photonics*, 2(3):036106, 03 2017.
- [10] H. Hamster, A. Sullivan, S. Gordon, W. White, and R. Falcone. Subpicosecond, electromagnetic pulses from intense laser-plasma interaction. *Physical review letters*, 71(17):2725, 1993.
- [11] A. Woldegeorgis, T. Kurihara, M. Almassarani, B. Beleites, R. Grosse, et al. Multi-mv/cm longitudinally polarized terahertz pulses from laser-thin foil interaction. *Optica*, 5(11):1474–1477, Nov 2018.

-
- [12] P. Salén, M. Basini, S. Bonetti, J. Hebling, M. Krasilnikov, A. Nikitin, et al. Matter manipulation with extreme terahertz light: Progress in the enabling thz technology. *Physics reports*, 836:1–74, 2019.
- [13] D. Nicoletti and A. Cavalleri. Nonlinear light–matter interaction at terahertz frequencies. *Advances in Optics and Photonics*, 8(3):401–464, 2016.
- [14] J. Walowski and M. Münzenberg. Perspective: Ultrafast magnetism and thz spintronics. *Journal of Applied Physics*, 120(14), 2016.
- [15] T. Pak, M. Rezaei-Pandari, S. Kim, G. Lee, D. Wi, et al. Multi-millijoule terahertz emission from laser-wakefield-accelerated electrons. *Light: Science & Applications*, 12(1):37, 2023.
- [16] G. Liao, Y. Li, Y. Zhang, H. Liu, X. Ge, et al. Demonstration of coherent terahertz transition radiation from relativistic laser-solid interactions. *Phys. Rev. Lett.*, 116:205003, May 2016.
- [17] Z. Jin, H. B. Zhuo, T. Nakazawa, J. H. Shin, S. Wakamatsu, et al. Highly efficient terahertz radiation from a thin foil irradiated by a high-contrast laser pulse. *Phys. Rev. E*, 94:033206, Sep 2016.
- [18] A. Gopal, T. May, S. Herzer, A. Reinhard, S. Minardi, et al. Observation of energetic terahertz pulses from relativistic solid density plasmas. *New Journal of Physics*, 14(8):083012, aug 2012.
- [19] G. Liao, Y. Li, Y. Zhang, H. Liu, X. Ge, et al. Demonstration of coherent terahertz transition radiation from relativistic laser-solid interactions. *Physical Review Letters*, 116(20):205003, 2016.
- [20] G. Liao, Y. Li, H. Liu, G. Scott, D. Neely, et al. Multimillijoule coherent terahertz bursts from picosecond laser-irradiated metal foils. *Proceedings of the National Academy of Sciences*, 116(10):3994–3999, 2019.
- [21] W. P. Leemans, A. J. Gonsalves, H.-S. Mao, K. Nakamura, C. Benedetti, and et al. Multi-gev electron beams from capillary-discharge-guided subpetawatt laser pulses in the self-trapping regime. *Phys. Rev. Lett.*, 113:245002, Dec 2014.
- [22] E. A. Peralta, K. Soong, R. J. England, E. R. Colby, Z. Wu, et al. Demonstration of electron acceleration in a laser-driven dielectric microstructure. *Nature*, 503(7474):91–94, 2013.

-
- [23] E. A. Nanni, W. R. Huang, K. Hong, K. Ravi, A. Fallahi, et al. Terahertz-driven linear electron acceleration. *Nature communications*, 6(1):8486, 2015.
- [24] L. V. Keldysh et al. Ionization in the field of a strong electromagnetic wave. *Sov. Phys. JETP*, 20(5):1307–1314, 1965.
- [25] V. S. Popov. Tunnel and multiphoton ionization of atoms and ions in a strong laser field (keldysh theory). *Physics-Uspeski*, 47(9):855, sep 2004.
- [26] S. V. Bulanov, I. N. Inovenkov, V. I. Kirsanov, N. M. Naumova, and A. S. Sakharov. Nonlinear depletion of ultrashort and relativistically strong laser pulses in an underdense plasma. *Physics of Fluids B: Plasma Physics*, 4(7):1935–1942, 07 1992.
- [27] S. V. Bulanov, N. M. Naumova, and F. Pegoraro. Interaction of an ultrashort, relativistically strong laser pulse with an overdense plasma. *Physics of Plasmas*, 1(3):745–757, 03 1994.
- [28] F. Pegoraro, T.Zh. Esirkepov, and S.V. Bulanov. Special relativity in action in laser produced plasmas. *Physics Letters A*, 347(1):133–142, 2005. Einstein Special Issue.
- [29] W. L. Kruer. *The physics of laser plasma interaction*, 1988.
- [30] V. L. Ginzburg. *The propagation of electromagnetic waves in plasmas. International Series of Monographs in Electromagnetic Waves*, 1970.
- [31] S.C. Wilks and W.L. Kruer. Absorption of ultrashort, ultra-intense laser light by solids and overdense plasmas. *IEEE Journal of Quantum Electronics*, 33(11):1954–1968, 1997.
- [32] W. Rozmus and V. T. Tikhonchuk. Skin effect and interaction of short laser pulses with dense plasmas. *Physical Review A*, 42(12):7401, 1990.
- [33] G. J. Pert. Inverse bremsstrahlung in strong radiation fields—the born approximation re-examined. *Journal of Physics B: Atomic, Molecular and Optical Physics*, 29(5):1135, 1996.
- [34] M. Chaker, J. C. Kieffer, J. P. Matte, H. Pepin, P. Audebert, et al. Interaction of a 1 psec laser pulse with solid matter. *Physics of Fluids B: Plasma Physics*, 3(1):167–175, 1991.

-
- [35] D. D. Meyerhofer, H. Chen, J. A. Delettrez, B. Soom, S. Uchida, et al. Resonance absorption in high-intensity contrast, picosecond laser–plasma interactions. *Physics of Fluids B: Plasma Physics*, 5(7):2584–2588, 1993.
- [36] V. L. GINZBURG. The propagation of electromagnetic waves in plasmas(book on plasma behavior in electromagnetic field discussing radio and electromagnetic wave propagation in earth atmosphere, interplanetary space and laboratory generated plasmas). 1964.
- [37] K. Estabrook and W. L. Kruer. Properties of resonantly heated electron distributions. *Physical Review Letters*, 40(1):42, 1978.
- [38] F. N. Beg, A. R. Bell, A. E. Dangor, C. N. Danson, A. P. Fews, et al. A study of picosecond laser–solid interactions up to 10^{19} w cm⁻². *Physics of plasmas*, 4(2):447–457, 1997.
- [39] P. Gibbon and E. Förster. Short-pulse laser - plasma interactions. *Plasma Physics and Controlled Fusion*, 38(6):769, jun 1996.
- [40] E. J. Valeo and K. G. Estabrook. Stability of the critical surface in irradiated plasma. *Physical Review Letters*, 34(16):1008, 1975.
- [41] F. Brunel. Not-so-resonant, resonant absorption. *Phys. Rev. Lett.*, 59:52–55, Jul 1987.
- [42] F. Brunel. Anomalous absorption of high intensity subpicosecond laser pulses. *The Physics of fluids*, 31(9):2714–2719, 1988.
- [43] K. G. Estabrook and W. L. Kruer. Resonant absorption in very steep density gradients. *Laser Program Annual Report*, pages 2–87, 1986.
- [44] W. L. Kruer and K. Estabrook. $J \times b$ heating by very intense laser light. *The Physics of Fluids*, 28(1):430–432, 1985.
- [45] G. Malka and J. L. Miquel. Experimental confirmation of ponderomotive-force electrons produced by an ultrarelativistic laser pulse on a solid target. *Phys. Rev. Lett.*, 77:75–78, Jul 1996.
- [46] S. C. Wilks, A. B. Langdon, T. E. Cowan, M. Roth, M. Singh, et al. Energetic proton generation in ultra-intense laser–solid interactions. *Physics of Plasmas*, 8(2):542–549, 2001.

-
- [47] T. Esirkepov, M. Borghesi, S. V. Bulanov, G. Mourou, and T. Tajima. Highly efficient relativistic-ion generation in the laser-piston regime. *Physical review letters*, 92(17):175003, 2004.
- [48] A. Higginson, R. J. Gray, M. King, R. J. Dance, S.D. Williamson, et al. Near-100 mev protons via a laser-driven transparency-enhanced hybrid acceleration scheme. *Nature communications*, 9(1):724, 2018.
- [49] A. Macchi, M. Borghesi, and M. Passoni. Ion acceleration by superintense laser-plasma interaction. *Reviews of Modern Physics*, 85(2):751, 2013.
- [50] H. Daido, M. Nishiuchi, and A. S Pirozhkov. Review of laser-driven ion sources and their applications. *Reports on Progress in Physics*, 75(5):056401, apr 2012.
- [51] P. Mora. Plasma expansion into a vacuum. *Phys. Rev. Lett.*, 90:185002, May 2003.
- [52] P. Mora. Thin-foil expansion into a vacuum. *Phys. Rev. E*, 72:056401, Nov 2005.
- [53] M. Nishiuchi, A. Fukumi, H. Daido, Z. Li, A. Sagisaka, et al. The laser proton acceleration in the strong charge separation regime. *Physics Letters A*, 357(4-5):339–344, 2006.
- [54] J. E. Crow, P. L. Auer, and J. E. Allen. The expansion of a plasma into a vacuum. *Journal of Plasma Physics*, 14(1):65–76, 1975.
- [55] A. V. Gurevich, L. V. Pariiskaya, and L. P. Pitaevskii. Self-similar motion of rarefied plasma. *Sov. Phys. JETP*, 22(2):449–454, 1966.
- [56] A. Pukhov. Three-dimensional simulations of ion acceleration from a foil irradiated by a short-pulse laser. *Physical review letters*, 86(16):3562, 2001.
- [57] B. R. Steffen and DESY. *Electro-Optic Methods for Longitudinal Bunch Diagnostics at FLASH*. Dr., Univ. Hamburg, Hamburg, 2007. Univ. Hamburg, Diss., 2007.
- [58] X. Yan, A. M. MacLeod, W. A. Gillespie, G. M. H. Knippels, D. Oepts, et al. Subpicosecond electro-optic measurement of relativistic electron pulses. *Phys. Rev. Lett.*, 85:3404–3407, Oct 2000.

-
- [59] K. R. Spring, M. J. Parry-Hill, and M. W. Davidson. The fresnel or refractive index ellipsoid. <http://micro.magnet.fsu.edu/primer/java/polarizedlight/ellipsoid/index.html>, 2017.
- [60] S. Casalbuoni, H. Schlarb, B. Schmidt, B. Steffen, P. Schmüser, et al. Numerical studies on the electro-optic sampling of relativistic electron bunches. *DESY. Hamburg, Germany, 2005 – Forschungsbericht TESLA Report*, 2005-01.
- [61] A. S. Barker. Transverse and longitudinal optic mode study in mgf_2 and znf_2 . *Phys. Rev.*, 136:A1290–A1295, Nov 1964.
- [62] G. Gallot, J. Zhang, R. W. McGowan, Tae-In Jeon, et al. Measurements of the THz absorption and dispersion of ZnTe and their relevance to the electro-optic detection of THz radiation. *Applied Physics Letters*, 74(23):3450–3452, 06 1999.
- [63] W. L. Faust and Charles H. Henry. Mixing of visible and near-resonance infrared light in gap. *Phys. Rev. Lett.*, 17:1265–1268, Dec 1966.
- [64] A. Leitenstorfer, S. Hunsche, J. Shah, M. Nuss, and W. Knox. Detectors and sources for ultrabroadband electro-optic sampling: Experiment and theory. *Applied physics letters*, 74(11):1516–1518, 1999.
- [65] S. Casalbuoni, H. Schlarb, B. Schmidt, P. Schmüser, B. Steffen, et al. Numerical studies on the electro-optic detection of femtosecond electron bunches. *Phys. Rev. ST Accel. Beams*, 11:072802, Jul 2008.
- [66] Q. Wu and X.-C Zhang. 7 terahertz broadband gap electro-optic sensor. *Applied Physics Letters*, 70(14):1784–1786, 1997.
- [67] A. Azima. An electro-optical timing diagnostic for pump-probe experiments at the Free-Electron Laser in Hamburg FLASH. Other thesis, 7 2009.
- [68] J. Shan, A. Weling, E. Knoesel, L. Bartels, M. Bonn, et al. Single-shot measurement of terahertz electromagnetic pulses by use of electro-optic sampling. *Opt. Lett.*, 25(6):426–428, Mar 2000.
- [69] A. Yariv and P. Yeh. *Optical Waves in Crystals Propagation and Control of Laser Radiation*. John Wiley & Sons, New York, 1984.

-
- [70] M. Brunken, H. Genz, P. Göttlicher, C. Hessler, M. Hüning, and et al. Electro-optic sampling at the tesla test accelerator: experimental setup and first results. *DESY. Hamburg, Germany, 2005 – Forschungsbericht TESLA Report*, 2003-11.
- [71] P. Gibbon. *Short Pulse Laser Interactions with Matter*. PUBLISHED BY IMPERIAL COLLEGE PRESS AND DISTRIBUTED BY WORLD SCIENTIFIC PUBLISHING CO., 2005.
- [72] A. Poyé, S. Hulin, M. Bailly-Grandvaux, J.-L. Dubois, J. Ribolzi, et al. Physics of giant electromagnetic pulse generation in short-pulse laser experiments. *Phys. Rev. E*, 91:043106, Apr 2015.
- [73] A. Gopal, S. Herzer, A. Schmidt, P. Singh, A. Reinhard, et al. Observation of gigawatt-class thz pulses from a compact laser-driven particle accelerator. *Phys. Rev. Lett.*, 111:074802, Aug 2013.
- [74] A. Gopal, P. Singh, S. Herzer, A. Reinhard, A. Schmidt, et al. Characterization of 700 μ J T rays generated during high-power laser solid interaction. *Opt. Lett.*, 38(22):4705–4707, Nov 2013.
- [75] C. Rödel, M. Heyer, M. Behmke, M. Kübel, O. Jäckel, and et al. High repetition rate plasma mirror for temporal contrast enhancement of terawatt femtosecond laser pulses by three orders of magnitude. *Appl. Phys. B*, 103:295–302, 2011.
- [76] S. Casalbuoni, B. Schmidt, P. Schmüser, V. Arsov, and S. Wesch. Ultrabroadband terahertz source and beamline based on coherent transition radiation. *Phys. Rev. ST Accel. Beams*, 12:030705, Mar 2009.
- [77] S. Quabis, R. Dorn, M. Eberler, O. Glöckl, and G. Leuchs. Focusing light to a tighter spot¹this article is dedicated to marlan o. scully on the occasion of his 60th birthday. we very much appreciate his enormous contribution to science. but above all we like his approach. when told “sir, i have a problem which cannot be solved and above all it’s crazy” his typical answer will be “tell me more about it, i am interested. i give you five minutes”.1. *Optics Communications*, 179(1):1–7, 2000.
- [78] Elijah Y. S. Yew and Colin J. R. Sheppard. Tight focusing of radially polarized gaussian and bessel-gauss beams. *Opt. Lett.*, 32(23):3417–3419, Dec 2007.

-
- [79] S. A. Kennedy, M. J. Szabo, H. Teslow, J. Z. Porterfield, and E. R. I. Abraham. Creation of laguerre-gaussian laser modes using diffractive optics. *Phys. Rev. A*, 66:043801, Oct 2002.
- [80] A. Gopal, A. Woldegeorgis, S. Herzer, and M. Almassarani. Spatiotemporal visualization of the terahertz emission during high-power laser-matter interaction. *Phys. Rev. E*, 100:053203, Nov 2019.
- [81] M. J. Mead, D. Neely, J. Gauoin, R. Heathcote, and P. Patel. Electromagnetic pulse generation within a petawatt laser target chamber. *Review of Scientific Instruments*, 75(10):4225–4227, 2004.
- [82] J. J. Santos, F. Amiranoff, S. D. Baton, L. Gremillet, M. Koenig, et al. Fast electron transport in ultraintense laser pulse interaction with solid targets by rear-side self-radiation diagnostics. *Phys. Rev. Lett.*, 89:025001, Jun 2002.
- [83] J. Schreiber, F. Bell, F. Grüner, U. Schramm, M. Geissler, et al. Analytical model for ion acceleration by high-intensity laser pulses. *Phys. Rev. Lett.*, 97:045005, Jul 2006.
- [84] C. Bellei, J. R. Davies, P. K. Chauhan, and Z. Najmudin. Coherent transition radiation in relativistic laser–solid interactions. *Plasma Physics and Controlled Fusion*, 54(3):035011, feb 2012.
- [85] A. Woldegeorgis, S. Herzer, M. Almassarani, S. Marathapalli, and A. Gopal. Modeling terahertz emission from the target rear side during intense laser-solid interactions. *Phys. Rev. E*, 100:053204, Nov 2019.
- [86] S. Devic. Radiochromic film dosimetry: Past, present, and future. *Physica Medica*, 27(3):122–134, 2011.
- [87] H. Khan, R. Brandt, N. Khan, and K. Jamil. Track-registration-and-development characteristics of cr-39 plastic track detector. *Nuclear Tracks and Radiation Measurements (1982)*, 7(3):129–139, 1983.
- [88] M. Almassarani, S. Meng, B. Beleites, F. Ronneberger, G. Paulus, et al. Parametric study of proton acceleration from laser-thin foil interaction. *Plasma*, 4(4):670–680, 2021.

-
- [89] M. Roth and M. Schollmeier. Ion acceleration—target normal sheath acceleration. *CERN Yellow Reports*, pages Vol 1 (2016): Proceedings of the 2014 CAS–CERN Accelerator School: Plasma Wake Acceleration, 2016.
- [90] M. Schnürer, M. P. Kalashnikov, P. V. Nickles, Th. Schlegel, W. Sandner, et al. Hard x-ray emission from intense short pulse laser plasmas. *Physics of Plasmas*, 2(8):3106–3110, 1995.
- [91] S. C. Wilks, W. L. Kruer, M. Tabak, and A. B. Langdon. Absorption of ultra-intense laser pulses. *Phys. Rev. Lett.*, 69:1383–1386, Aug 1992.
- [92] A. P. Fews, P. A. Norreys, F. N. Beg, A. R. Bell, A. E. Dangor, et al. Plasma ion emission from high intensity picosecond laser pulse interactions with solid targets. *Phys. Rev. Lett.*, 73:1801–1804, Sep 1994.
- [93] J. Fuchs, P. Antici, E. d’Humières, E. Lefebvre, M. Borghesi, E. Brambrink, C. A. Cecchetti, M. Kaluza, V. Malka, M. Manclossi, and et al. Laser-driven proton scaling laws and new paths towards energy increase. *Nature News*, Dec 2005.
- [94] Y. Sentoku, V.Y. Bychenkov, K. Flippo, A. Maksimchuk, K. Mima, G. Mourou, Z.M. Sheng, and D. Umstadter. High-energy ion generation in interaction of short laser pulse with high-density plasma - applied physics b. *SpringerLink*, Feb 2014.
- [95] F. Verluise, V. Laude, J. Huignard, P. Tournois, and A. Migus. Arbitrary dispersion control of ultrashort optical pulses with acoustic waves. *J. Opt. Soc. Am. B*, 17(1):138–145, Jan 2000.
- [96] T. Oksenhendler, S. Coudreau, N. Forget, V. Crozatier, S. Grabielle, et al. Self-referenced spectral interferometry - applied physics b. *SpringerLink*, Feb 2010.
- [97] A. S. Pirozhkov, M. Mori, A. Yogo, H. Kiriya, K. Ogura, et al. Laser-driven proton acceleration and plasma diagnostics with J-KAREN laser. 7354:735414, 2009.
- [98] J. Schreiber, F. Bell, F. Grüner, U. Schramm, M. Geissler, et al. Analytical model for ion acceleration by high-intensity laser pulses. *Phys. Rev. Lett.*, 97:045005, Jul 2006.

-
- [99] S. P. Hatchett, C. G. Brown, T. E. Cowan, E. A. Henry, J. S. Johnson, et al. Electron, photon, and ion beams from the relativistic interaction of petawatt laser pulses with solid targets. *Physics of Plasmas*, 7(5):2076–2082, 2000.
- [100] K. Yasuike, M. H. Key, S. P. Hatchett, R. A. Snavely, and K. B. Wharton. Hot electron diagnostic in a solid laser target by k-shell lines measurement from ultraintense laser–plasma interactions. *Review of Scientific Instruments*, 72(1):1236–1240, 2001.
- [101] S. Augst, D. Strickland, D. D. Meyerhofer, S. L. Chin, and J. H. Eberly. Tunneling ionization of noble gases in a high-intensity laser field. *Phys. Rev. Lett.*, 63:2212–2215, Nov 1989.
- [102] H. Bethe. Zur theorie des durchgangs schneller korpuskularstrahlen durch materie. *Annalen der Physik*, 397(3):325–400, 1930.
- [103] Y. Sentoku, V. Y. Bychenkov, K. Flippo, A. Maksimchuk, K. Mima, et al. High-energy ion generation in interaction. of short laser pulse with high-density plasma. *Applied Physics B*, 74:207–215, 2002.
- [104] V. L. Ginzburg. Radiation by uniformly moving sources (vavilov-cherenkov effect, transition radiation, and other phenomena). *Phys. Usp.*, 39(10):973–982, 1996.
- [105] M. L. Ter-Mikaelian. *High-Energy Electromagnetic Processes in Condensed Media*. Wiley-Interscience, New York, 1972.
- [106] C. B. Schroeder, E. Esarey, J. van Tilborg, and W. P. Leemans. Theory of coherent transition radiation generated at a plasma-vacuum interface. *Phys. Rev. E*, 69:016501, Jan 2004.
- [107] J. Zheng, K. A. Tanaka, T. Miyakoshi, Y. Kitagawa, R. Kodama, et al. Theoretical study of transition radiation from hot electrons generated in the laser–solid interaction. *Physics of Plasmas*, 10(7):2994–3003, 2003.
- [108] P. Antici, J. Fuchs, M. Borghesi, L. Gremillet, T. Grismayer, et al. Hot and cold electron dynamics following high-intensity laser matter interaction. *Phys. Rev. Lett.*, 101:105004, Sep 2008.
- [109] J. D. Jackson. *Classical Electrodynamics*. Wiley, New York, 1999.

-
- [110] A.S. Kuratov, A.V. Brantov, Yu.M. Aliev, and V.Yu. Bychenkov. Terahertz radiation in laser-induced charge separation in the irradiated plasma target. *Quantum Electronics*, 46(11):1023, nov 2016.
- [111] U. Happek, A. J. Sievers, and E. B. Blum. Observation of coherent transition radiation. *Phys. Rev. Lett.*, 67:2962–2965, Nov 1991.
- [112] J. Van Tilborg, C.B. Schroeder, E. Esarey, and W.P. Leemans. Pulse shape and spectrum of coherent diffraction-limited transition radiation from electron beams. *Laser and Particle Beams*, 22(4):415–422, 2004.
- [113] M. Castellano, A. Cianchi, G. Orlandi, and V.A. Verzilov. Effects of diffraction and target finite size on coherent transition radiation spectra in bunch length measurements. *Nuclear Instruments and Methods in Physics Research Section A: Accelerators, Spectrometers, Detectors and Associated Equipment*, 435(3):297–307, 1999.
- [114] C. Bellei, S. R. Nagel, S. Kar, A. Henig, S. Kneip, et al. Micron-scale fast electron filaments and recirculation determined from rear-side optical emission in high-intensity laser–solid interactions. *New Journal of Physics*, 12(7):073016, jul 2010.
- [115] L. Romagnani, J. Fuchs, M. Borghesi, P. Antici, P. Audebert, et al. Dynamics of electric fields driving the laser acceleration of multi-mev protons. *Phys. Rev. Lett.*, 95:195001, Oct 2005.
- [116] S. N. Chen, A. P. L. Robinson, P. Antici, E. Brambrink, E. d’Humières, et al. Passive tailoring of laser-accelerated ion beam cut-off energy by using double foil assembly. *Physics of Plasmas*, 21(2):023119, 2014.
- [117] A. D. Lad, Y. Mishima, P. K. Singh, B. Li, A. Adak, et al. Luminous, relativistic, directional electron bunches from an intense laser driven grating plasma. *Scientific Reports*, 12(1):16818, 2022.
- [118] P. Planken, H. Nienhuys, H. Bakker, and T. Wenzel. Measurement and calculation of the orientation dependence of terahertz pulse detection in znte. *J. Opt. Soc. Am. B*, 18(3):313–317, Mar 2001.
- [119] In J. Diels and W. Rudolph, editors, *Ultrashort Laser Pulse Phenomena (Second Edition)*. Academic Press, second edition edition, 2006.

-
- [120] K. Huang, T. Esirkepov, J. Koga, H. Kotaki, M. Mori, et al. Electro-optic spatial decoding on the spherical-wavefront coulomb fields of plasma electron sources. *Scientific Reports*, 8(1):1–10, 2018.
- [121] M. Galletti, A. Cianchi, A. Curcio, F. Dipace, M. Ferrario, et al. Direct visualization of relativistic coulomb field in the near and far field ranges. *New Journal of Physics*, 25(6):063014, jun 2023.
- [122] V. A. Verzilov. Transition radiation in the pre-wave zone. *Physics Letters A*, 273(1):135–140, 2000.
- [123] H. J. Bakker, G. C. Cho, H. Kurz, Q. Wu, and X.-C. Zhang. Distortion of terahertz pulses in electro-optic sampling. *J. Opt. Soc. Am. B*, 15(6):1795–1801, Jun 1998.
- [124] S. Seltzer and P. Bergstrom. Stopping-power range tables for electrons, protons, and helium ions, 2019-2022.
- [125] H. Pratt, H. Tseng, C. Lee, L. Kissel, C. MacCallum, et al. Bremsstrahlung energy spectra from electrons of kinetic energy 1 keV or $\approx 10^3$ or ≈ 2000 keV incident on neutral atoms Z or $Z=92$. *At. Data Nucl. Data Tables; (United States)*, 20(1), 8 1977.
- [126] Z. Jin, H. B. Zhuo, T. Nakazawa, J. H. Shin, S. Wakamatsu, et al. Highly efficient terahertz radiation from a thin foil irradiated by a high-contrast laser pulse. *Phys. Rev. E*, 94:033206, Sep 2016.
- [127] J. Déchard, X. Davoine, L. Gremillet, and L. Bergé. Terahertz emission from sub-micron solid targets irradiated by ultraintense femtosecond laser pulses. *Physics of Plasmas*, 27(9), 09 2020. 093105.
- [128] F. Wagner, S. Bedacht, A. Ortner, M. Roth, A. Tauschwitz, et al. Pre-plasma formation in experiments using petawatt lasers. *Opt. Express*, 22(24):29505–29514, Dec 2014.
- [129] Oliver J. *Characterisation of ion acceleration with relativistic laser-plasmas*. Phd thesis, Friedrich-Schiller-Universität, Jena, Germany, 2009. ISBN 978-3-89959-902-2.

-
- [130] P. Mora. Collisionless expansion of a Gaussian plasma into a vacuum. *Physics of Plasmas*, 12(11), 11 2005. 112102.
- [131] A. J. Mackinnon, Y. Sentoku, P. K. Patel, D. W. Price, S. Hatchett, et al. Enhancement of proton acceleration by hot-electron recirculation in thin foils irradiated by ultraintense laser pulses. *Phys. Rev. Lett.*, 88:215006, May 2002.
- [132] J. Albritton and P. Koch. Cold plasma wavebreaking: Production of energetic electrons. *The Physics of Fluids*, 18(9):1136–1139, 09 1975.
- [133] D. R. Blackman, Y. Shi, S. R. Klein, M. Cernaianu, D. Doria, et al. Electron acceleration from transparent targets irradiated by ultra-intense helical laser beams. *Communications Physics*, 5(1):116, 2022.
- [134] J. Braenzel, A. A. Andreev, F. Abicht, L. Ehrentraut, K. Platonov, et al. Amplification of relativistic electron bunches by acceleration in laser fields. *Phys. Rev. Lett.*, 118:014801, Jan 2017.
- [135] A. Sharma. High energy electron and proton acceleration by circularly polarized laser pulse from near critical density hydrogen gas target. *Scientific reports*, 8(1):2191, 2018.
- [136] D. Zhang, A. Fallahi, M. Hemmer, X. Wu, M. Fakhari, et al. Segmented terahertz electron accelerator and manipulator (steam). *Nature photonics*, 12(6):336–342, 2018.
- [137] L. Zhao, Z. Wang, H. Tang, R. Wang, and Y. and. others Cheng. Terahertz oscilloscope for recording time information of ultrashort electron beams. *Physical review letters*, 122(14):144801, 2019.
- [138] S. Corde, E. Adli, J. M. Allen, W. An, C. I. Clarke, et al. Multi-gigaelectronvolt acceleration of positrons in a self-loaded plasma wakefield. *Nature*, 524(7566):442–445, 2015.
- [139] O. Rosmej, N. Andreev, S. Zaehter, N. Zahn, P. Christ, and et al. Interaction of relativistically intense laser pulses with long-scale near critical plasmas for optimization of laser based sources of MeV electrons and gamma-rays. *New Journal of Physics*, 21(4):043044, apr 2019.

10 Ehrenwörtliche Erklärung

Ich erkläre hiermit ehrenwörtlich, dass ich die vorliegende Arbeit selbständig, ohne unzulässige Hilfe Dritter und ohne Benutzung anderer als der angegebenen Hilfsmittel und Literatur angefertigt habe. Die aus anderen Quellen direkt oder indirekt übernommenen Daten und Konzepte sind unter Angabe der Quelle gekennzeichnet.

Bei der Auswahl und Auswertung folgenden Materials bzw. der Beisteuerung von Material/Daten haben mir die nachstehend aufgeführten Personen in der jeweils beschriebenen Weise entgeltlich/unentgeltlich geholfen:

- Dr. Gopal und A. Woldegeorgis (meine vorherigen Kollegen) mit Aufnahme, Analyse, Diskussion, und Interpretation der Resultate in Kapitel 3 und 5.

Weitere Personen waren an der inhaltlich-materiellen Erstellung der vorliegenden Arbeit nicht beteiligt. Insbesondere habe ich hierfür nicht die entgeltliche Hilfe von Vermittlungs- bzw. Beratungsdiensten (Promotionsberater oder andere Personen) in Anspruch genommen. Niemand hat von mir unmittelbar oder mittelbar geldwerte Leistungen für Arbeiten erhalten, die im Zusammenhang mit dem Inhalt der vorgelegten Dissertation stehen.

Die Arbeit wurde bisher weder im In- noch im Ausland in gleicher oder ähnlicher Form einer anderen Prüfungsbehörde vorgelegt. Die geltende Promotionsordnung der Physikalisch-Astronomischen Fakultät ist mir bekannt.

Ich versichere ehrenwörtlich, dass ich nach bestem Wissen die reine Wahrheit gesagt und nichts verschwiegen habe.

Jena, den 07.08.2023

Mohammed Almassarani